THE FLORIDA STATE UNIVERSITY

COLLEGE OF ARTS AND SCIENCES

MEASUREMENT OF THE POLARIZATION OBSERVABLES I^S AND I^C FOR $\vec{\gamma}\, p \to p\, \pi^+\, \pi^-$ USING THE CLAS SPECTROMETER

(THESIS TEXT MODIFIED TO BE USED AS CLAS ANALYSIS NOTE)

By

CHARLES HANRETTY

A Dissertation submitted to the
Department of Physics
in partial fulfillment of the
requirements for the degree of
Doctor of Philosophy in Physics

Degree Awarded:
Spring Semester, 2011

The members of the committee approve the dissertation of Charles Hanretty defended on December 7^{th}, 2010.

Dr. Volker Credé
Professor Directing Dissertation

Dr. Greg Riccardi
University Representative

Dr. Paul Eugenio
Committee Member

Dr. Winston Roberts
Committee Member

Dr. Todd Adams
Committee Member

Approved:

Dr. Mark Riley, Chair, Department of Physics

Dr. Joseph Travis, Dean, College of Arts and Sciences

The Graduate School has verified and approved the above-named committee members.

TABLE OF CONTENTS

LIST OF FIGURES

LIST OF TABLES

CHAPTER 1

PREPARATION OF THE $p\ \pi^+\pi^-$ FINAL STATE

Data collection for the g8b experiment was carried out by the CLAS Collaboration between July 20^{th} and September 1^{st} of 2005. The data set boasts 11,475 data files, is $\approx$ 30 TB in size and contains 10.7 billion triggers. These data taken during the running of the g8b is stored on large data tapes in a "silo" at Jefferson Lab. This data was initially in its raw format, consisting of only detector signals and information about the various detector elements. Therefore the data must undergo reconstruction, or be *cooked* (transforming the data into information about scattered particle angles, masses, velocities, momenta, etc), in order for it to be ready for a physics analysis. It is also during this cooking phase that the calibration of the detectors is carried out with each detector being calibrated independently.

Quark model calculations suggest that the excited baryon resonances decay back to their ground state through decays involving intermediate states (with the emission of a meson). Some of these intermediate states, for example, are then expected to decay further into $\Delta\pi$ which then decays into a $p\,\pi^+\pi^-$ final state. Therefore the primary final state/channel investigated in this work is:

$$\vec{\gamma}\ p \rightarrow p\,\pi^+\pi^-,$$

where all final state particles are detected. We call this final state Topology 4. Three additional topologies are investigated as well:

Topology 1: $\vec{\gamma}\ p \rightarrow p\ \pi^+(\pi^-)$ (π^- not detected),

Topology 2: $\vec{\gamma}\ p \rightarrow p\ \pi^-(\pi^+)$ (π^+ not detected),

Topology 3: $\vec{\gamma}\ p \rightarrow \pi^+\pi^-(p)$ (proton not detected).

The investigation of these three additional final state topologies serves to provide a way to extract the polarization observables over topology-dependent acceptance holes resulting in a continuous measurement and to study acceptance effects themselves. Several steps and techniques were used to carry forth this analysis and are described in the following sections.

1.1 Pre-Event Selection

After the detectors have been calibrated and the particle tracks have been reconstructed, the cooking of the data is complete and the data is made available for analysis. Each event

in the data has its information organized into data banks. These data banks hold not only the properties of the particles involved in the reaction but information about detector hits. Specific data banks of interest in this analysis are the GPID, TAGR, TBID, TBER, and MVRT banks. How and where these banks were used will be explained during the course of this chapter.

We have used the following data runs in our analysis:

1. 1.3 GeV Setting (PARA): 48224, 48226, 48227, 48228, 48229, 48230, 48231, 48232, 48235, 48236, 48256, 48257, 48258, 48259, 48260, 48261, 48262, 48278, 48279, 48280, 48281, 48282, 48283, 48284, 48285, 48286, 48309, 48310, 48315, 48316, 48317, 48318, 48319, 48320

2. 1.3 GeV Setting (PERP): 48240, 48241, 48245, 48246, 48247, 48248, 48249, 48250, 48251, 48268, 48270, 48271, 48272, 48273, 48274, 48276, 48292, 48293, 48294, 48295, 48296, 48297, 48298, 48323, 48326, 48327, 48328, 48329, 48330

3. 1.5 GeV Setting (PARA): 48418, 48419, 48420, 48421, 48422, 48423, 48424, 48426, 48445, 48446, 48447, 48448, 48449, 48450, 48452, 48454, 48455, 48462, 48463, 48464, 48465, 48501, 48502, 48503, 48504, 48505, 48507, 48508, 48509

4. 1.5 GeV Setting (PERP): 48431, 48432, 48433, 48434, 48435, 48436, 48437, 48438, 48439, 48440, 48441, 48442, 48443, 48444, 48466, 48467, 48469, 48477, 48478, 48479, 48482, 48483, 48484, 48485, 48486, 48487, 48488

5. 1.7 GeV Setting (PARA): 48544, 48545, 48546, 48547, 48548, 48549, 48550, 48551, 48552, 48554, 48555, 48556, 48557, 48558, 48561, 48562, 48564, 48565, 48566, 48567, 48568, 48569, 48570, 48571

6. 1.7 GeV Setting (PERP): 48580, 48581, 48582, 48583, 48584, 48585, 48586, 48587, 48588, 48589, 48590, 48591, 48592, 48593, 48595, 48596, 48597, 48598, 48599, 48601, 48602, 48603, 48605, 48607, 48608, 48609, 48610, 48620, 48623, 48624, 48626, 48628, 48630

7. 1.9 GeV Setting (AUTO): 48091, 48093, 48095, 48096, 48098, 48099, 48103, 48104, 48105, 48107, 48108, 48110, 48115, 48117, 48120, 48131, 48132, 48134, 48135, 48137, 48146, 48148, 48149, 48150, 48152, 48153, 48154, 48157, 48158, 48159, 48163, 48165, 48171, 48172, 48176, 48178, 48181, 48182, 48185, 48186, 48187, 48189, 48190, 48192, 48195, 48196, 48199, 48200

8. 2.1 GeV Setting (PARA): 48357, 48358, 48359, 48360, 48361, 48362, 48363, 48364, 48365, 48387, 48388, 48392, 48393, 48394, 48395, 48396, 48397, 48399, 48400, 48405, 48406, 48407, 48408

9. 2.1 GeV Setting (PERP): 48335, 48337, 48338, 48339, 48340, 48341, 48342, 48343, 48344, 48348, 48349, 48351, 48366, 48367, 48368, 48370, 48371, 48372, 48373, 48374, 48377

10. Amorphous runs: 48211, 48215-48217, 48237-48239, 48252-48254, 48265-48267, 48287, 48290, 48291, 48299, 48305, 48307, 48308 // 47923, 47927, 47931, 47935, 47939, 47945, 47946, 48413, 48414-48417, 48427-48429, 48456, 48460, 48461, 48489, 48492 // 47951, 47955, 47994, 48023, 48028, 48032, 48037, 48041, 48045, 48073, 48077, 48083, 48528-48531, 48575, 48576, 48578, 48579, 48635, 48636, 48641-48643 // 48092, 48097, 48101, 48106, 48111, 48112, 48114, 48126, 48133, 48138, 48147, 48151, 48155, 48160, 48177, 48183, 48184, 48188, 48193, 48197 // 48352-48355, 48381-48386

Explanation of data banks:

- GPID: This data bank contains much of the information regarding the event. This information includes the particle IDs, vertex positions (for each detected particle), 4-vectors, charge, beta ($\beta = \frac{v}{c}$) of the particle, the vertex time of the particle's track, particle masses (calculated), the incident photon's energy, photon time, and an index to the TAGR bank for the incident photon. Information from several detectors are used to fill this data bank. These detectors are: the Drift Chambers, Time of Flight Scintillators, Tagger and Start Counter.

- TAGR: Information recorded by the Hall B tagging system (the Tagger) is stored here. Information includes: energy of all recorded photons, reconstructed time of photon as calculated by the Tagger, the corrected time of the photon using information from other detectors as well, the *status* of the photon (whether or not it was properly reconstructed), and the E- and T- counter the scattered electron hit.

- TBER: The tracking resolution errors associated with the tracking measurements of the particles in the event are stored in this bank. Information comes mainly from the Drift Chambers and the Time of Flight. This bank is used to build up the covariance matrix used for kinematic fitting.

- MVRT: This bank uses information from the Drift Chambers and the Time of Flight and contains the vertex information for the event as a whole using individual particle tracks.

1.2 Event Selection

Since the g8b experiment was not designed for this analysis alone, the trigger file (for this run period, a single charged, able-to-be-reconstructed track in a single sector of CLAS) used during data-taking allowed for the recording of a large variety of hadronic events. In order to analyze a specific channel, the first step of this analysis is therefore to find events possessing the final states of interest. As stated before, there are 4 different topologies of interest in this analysis. However since the data contains all events which passed the single-sector requirement of the trigger, the data must be *filtered*, keeping only the final states of interest.

This filtering occurs by placing requirements regarding what data to keep based on the particle's identification number, or *PID*, which is determined during the cooking process and is based on the value of the particle's calculated mass. Events that do not meet this requirement are ignored and subsequently omitted from the analysis. The calculation of the detected particle's mass uses two independently measured quantities, its momentum (p) and velocity as a fraction of the speed of light, β. The magnitude of the particle's momentum (p) is determined with an error of $< 1\%$ using the measurements made by the Drift Chambers [43]. The β value of the detected final state particle is determined using a combination of the Start Counter, the Time of Flight, and the particle's detected trajectory through CLAS (with an error of up to 5 %).

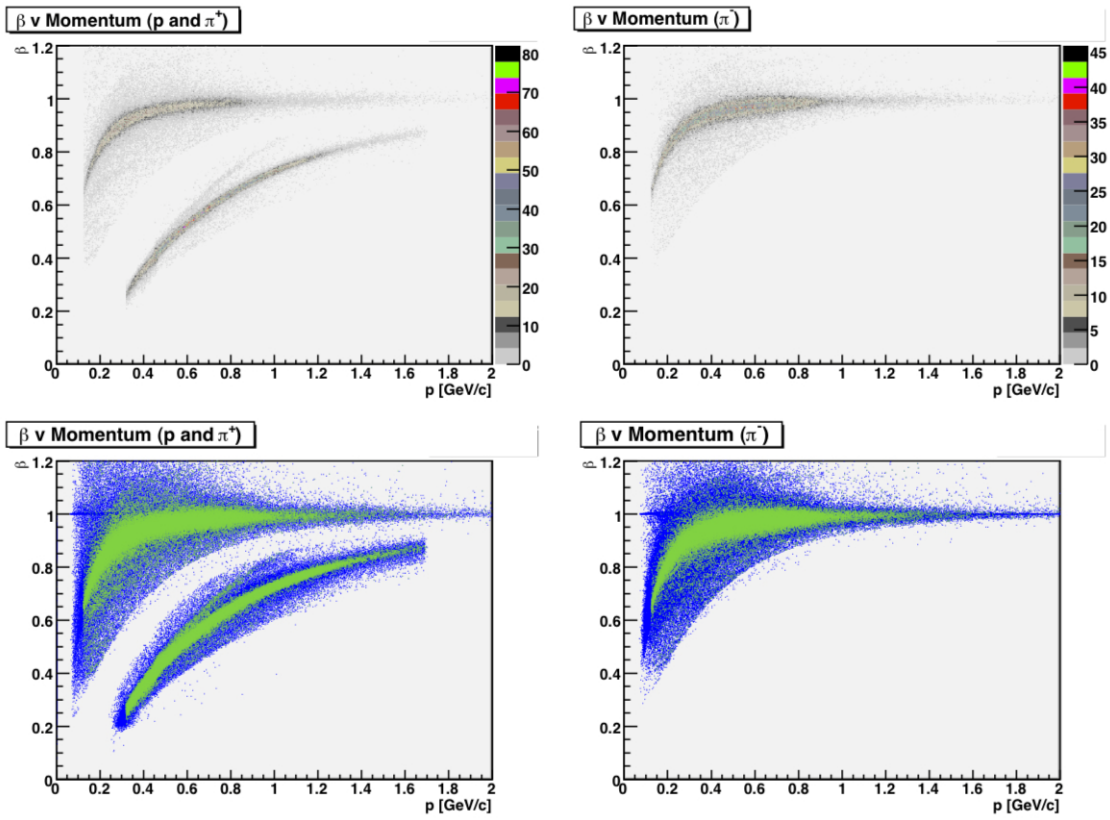

Figure 1.1: β versus momentum distributions from run #048326 for positively-charged particles (proton and π^+) (left) and negatively-charged particles (π^-) (right) before and after all cuts. Clear and fairly narrow bands can be observed for the different final-state particles. See text for more details.

The top row of Figure 1.1 shows "momentum vs. β" distributions from run #48326 for positively-charged particles (p and π^+) (left) and negatively-charged particles (π^-) (right) after all cuts. Topology 4 has been used for selecting $\gamma p \to p\pi^+\pi^-$ events, i.e. all three final-state particles are detected. The bottom row of the figure represents before / after plots: the blue bands are the distributions before all cuts, whereas the green bands are the *cleaned-up* distributions after all cuts (and thus correspond to the plots shown in the top row). The green bands in the bottom row appear broader than in the top row because no color code was used for the number of entries (ROOT COLZ option for histograms). Clear and fairly narrow bands can be observed for the different final-state particles. The figure shows typical CLAS distributions, which have been presented in other analyses, and demonstrates the quality of the particle identification system. The distributions for the proton (lower bands on the left side of Figure 1.1) exhibit a small tail for $p \in [0.6, 1.0]$ MeV/c. The events contributing to this tail are not accidentals. Our studies show that the final state is assigned to the correct tagger photon. We conclude that these tracks are incorrectly identified particles. We have cut these events from the analysis.

A detected particle's mass can then be calculated according to equation (1.1):

$$m^2_{\text{particle X}} = \frac{p^2(1-\beta^2)}{\beta^2}\,. \tag{1.1}$$

After the particle's mass has been calculated, it is compared to the masses of known particles (hadrons and leptons). If this calculated mass matches that of a known particle (within resolution errors), the PID associated with that mass is assigned to the final state particle. This value can then be used to select certain final state particles for analysis.

Therefore to select events that match one of the four topologies, the first requirement is based on this PID value (GPID[track number].pid = 8, 9, 14) and requires that the necessary final state particles are detected, no more, no less. Information regarding the properties of these final state particles (their 4-vectors, vertex information for individual particles, etc.) was then extracted from the GPID data bank and used for kinematic fitting, determination and application of cuts and systematic corrections, and the extraction of the polarization observables.

1.3 Photon Selection

The g8b run period used photoproduction on the proton via a beam of tagged photons. As the electrons used to produce this beam of polarized photons arrive in Hall B from the accelerator in 2 ns bunches with each bunch containing many electrons, the photons too arrive at the target in bunches with each bunch containing many photons. Therefore an accurate determination of the correct photon is very important in order to have a full understanding of the initial state of the event. This determination uses data collected by the Drift Chambers (for tracking the particle's path), Time of Flight (for velocity and timing information), and the Tagger (for photon timing information). The timing information collected by the Time of Flight and the Tagger (both independently calibrated) are used to make a time-based determination of the correct photon.

Each event in the g8b data set has an average of 16 *candidate* photons associated with it (Figure 1.2(a)). For a photon to be considered a candidate, it must occur within the timing window set by the trigger and satisfy several consistency checks involving the Tagger. These consistency checks involve the photon having a corresponding hit in the E- and T-counters, depositing a certain amount of energy in the E-counter, and producing a PMT signal at both ends of the scintillator bars that make up the E- and T-plane of the Tagger.

In spite of these requirements, many candidate photons are present in the data stream for one physics event as a result of the 2 ns bunching of the electron beam. To determine the exact photon corresponding to a physics event, vertex information of the physics event along with the timing information regarding the photon(s) are used. The time of the event's vertex is determined by using information from the Time of Flight along with an extrapolation of a particle's track (a particle in the event) through CLAS. The process for determining the correct photon uses the following steps.

First, the vertex time of the event (t_v) is calculated:

$$t_v = t_{TOF} - \frac{d_{TOF}}{c\beta_c}\,, \tag{1.2}$$

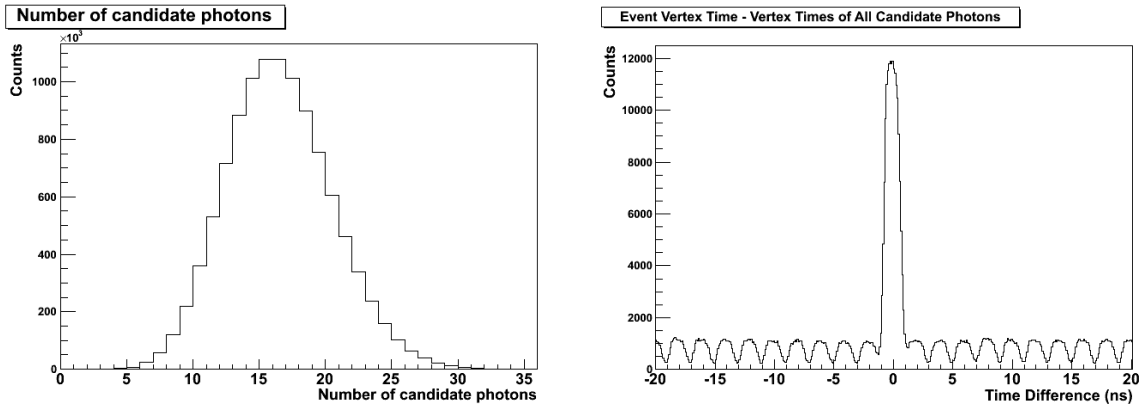

(a) (b)

Figure 1.2: (a) Shows the number of candidate photons per event in the data. There is an average of 16 candidate photons associated with every physics event. (b) Shows a distribution of the time difference (Δt) between the event vertex time (t_v) and the vertex time of all candidate photons. The 2 ns-wide distributions to the right and left of the central peak represent the 2 ns bucket structure in which the electrons (and therefore photons) in the beam arrive. Both histograms were produced using run #048326.

where t_{TOF} is the time at which the hadron was detected by the TOF, d_{TOF} is the calculated distance from the event vertex to the hit in the TOF scintillator paddle, c is the speed of light, and β_c is the hadron's velocity as a fraction of c. Next, the time of each candidate photon associated with the current event at the event vertex position (t_γ) is calculated:

$$t_\gamma = t_{center} + (\frac{z}{c}), \tag{1.3}$$

where t_{center} is the time at which the photon arrives at the center of the target (calculated by mathematically propagating the electron as it leaves the accelerator to the radiator and then propagating the photon from the radiator to the center of the target cell), z is the distance between the center of the target cell and the event vertex (with both positions being measured along the beam axis), and c is again the speed of light. The small offsets in the x- and y-positions of the event vertex do not appear in the calculations as they are comparable to the resolution of vertex measurements.

The correct incident photon is then found by comparing these two times calculated in equations (1.2) and (1.3) (t_v and t_γ) as in equation (1.4):

$$\Delta t = \mid t_v - t_\gamma \mid. \tag{1.4}$$

A distribution of the time differences between the event vertex time and the times of all candidate photons for the event can be seen in Figure 1.2(b). The 2 ns-wide structures to the right and left of the central peak show the 2 ns beam buckets in which the beam is delivered to the target.

The photon in the list of candidate photons with the smallest time difference between the event vertex time and the time of the photon at the event vertex (smallest value of Δt) is then labeled as the correct incident photon. The distribution seen in Figure 1.3 shows

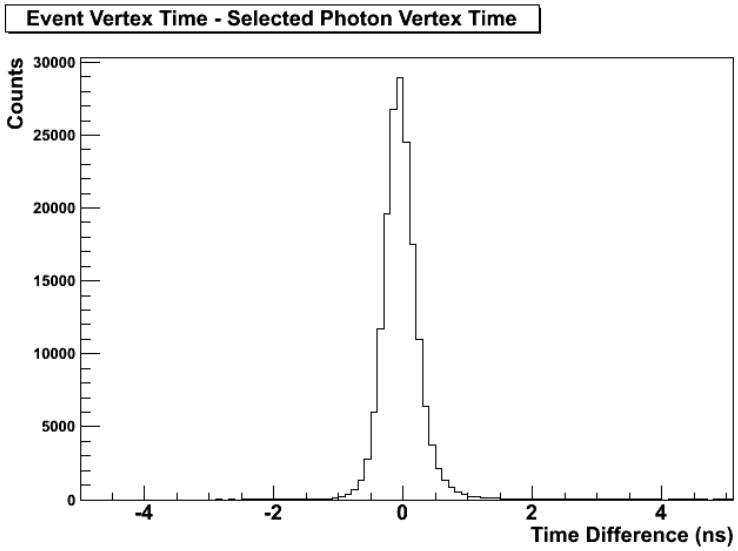

Figure 1.3: The time difference between the event vertex time and the time of the correct photon after photon determination. This distribution shows a large peak around zero, signifying the quality of photon selection. Produced using run #048326.

the time difference (in ns) between the event vertex time and photon which was determined to be the correct photon.

Using the above method results in the determination of a single photon in the beam bucket which is responsible for the event. However, in the instance that more than one photon is found with a time $\Delta t < 1$ ns, the statement as to which photon was actually responsible for the event cannot be made. In this case, the ambiguity of the photon determination is reflected in the GPID bank and these events are subsequently not analyzed. In this analysis, we required that GPID[ ].ngrf = 1 for all selected tracks and also that GPID[ ].tagrid be the same for all tracks.

Once a single photon is found to be the incident photon, the information regarding the incident photon is then stored in the GPID bank for each final state particle. The fact that the incident photon is found per particle track means that a quick cross check of the reconstruction code can be carried out by comparing the photon times for each final state particle. When analyzing an event, the photon's energy and time (as well as other information regarding the photon) are obtained from the GPID and TAGR banks. This information is then used in the reconstruction of the event, the binning of the data, systematic corrections for the photon energy and to perform cuts.

1.4 ELoss

As a charged particle travels from the target cell to the Drift Chambers of CLAS, it loses energy through atomic excitations and ionization when interacting with the target material (liquid hydrogen), target walls, support structures, beam pipe, start counter, and the air gap between the start counter and the Region 1 drift chambers. Therefore the

reconstructed momentum seen in the Drift Chambers is actually less than the momentum of the particle(s) at the production vertex. To account and correct for this, the 4-vectors of the final state particles (as taken from the data) were corrected event-by-event according to the ELoss package developed for charged particles moving through CLAS (using the g8b parameters such as target geometry and target material) [53]. This ELoss package calculates the momentum of the particle in the target cell. To perform this calculation, the particle's 4-momentum as measured by the Region 1 Drift Chambers is used to track the particle back to the reaction vertex in the target cell. As the particle is tracked back to the reaction vertex, the materials and distances it traverses are considered and the energy loss of the detected particle calculated and the 4-vector of the particle appropriately corrected. The energy-loss-corrected 4-vectors are then used in the analysis with the corrections being on the order of a few MeV.

1.5 KinFit

Unique to this g8b analysis is the implementation of the COBRA kinematic fitter developed at Carnegie Melon University for CLAS experiments [54]. The use of this kinematic fitter further refines the data through the enforcement of energy-momentum conservation and missing mass cuts (should the fit hypothesis contain a missing particle). The kinematic fitter is also very useful for the precise determination of systematic errors such as momentum corrections (needed to account for variations of the magnetic field of CLAS as well as any inconsistencies in the Drift Chambers) and photon energy corrections (needed to account for mismeasurements of the photon's energy) to be applied to the data. The following briefly describes the fitter and its implementation.

When an event is kinematically fitted, it is forced to obey energy-momentum conservation. The 4-vectors of the final state particles as determined by the reconstruction code are fed to the fitter as well as the incident photon energy. The components of these 4-vectors and the photon energy are then altered until the event satisfies energy-momentum conservation. These alterations occur within the limits (measurement errors) contained in the *full covariance matrix* which uses the *tracking covariance matrix*, built event-by-event from the data, and the scaling parameters associated with the tracking covariance matrix. After the tracking covariance matrix has been constructed for an event, the scaling parameters are then applied to it to form the full covariance matrix. These scaling parameters are unique to and must be determined for every run period and run condition. The resolution errors contained in the full covariance matrix represent the actual resolution of the detectors while the tracking covariance matrix is the resolution reported (calculated) by the reconstruction code. Once an event has been kinematically fitted, the quality of that fit can be quantified via a confidence level value of the fit as well as a pull value for every measurement parameter.

1.5.1 Confidence Level and Pulls

When using a kinematic fitter, the *goodness of fit* (the agreement between the data and the fit hypothesis) can be determined by examining the confidence level and pull distributions (Fig. 1.4).

The confidence level is defined as:

$$CL = \int_{\chi^2}^{\infty} f(z;n)dz, \tag{1.5}$$

where *f(z;n)* is the χ^2 probability density function possessing n degrees of freedom. It is a determination of the probability that a χ^2 from the theoretical distribution is greater than the χ^2 obtained from the fit.

An ideal data set containing only events which satisfy the fit hypothesis and with normally distributed errors would result in a confidence level distribution that is flat from (0,1]. However, a real-life data set run through the fitter (assuming the resolution errors have been properly determined) would produce a confidence level distribution that has a peak at zero. This distribution should then possess a negative slope as you move to higher confidence level values with this slope becoming level (flat) from [0.5,1] (representing confidence levels of 50 % - 100 %). The large number of events with a low confidence level represent the events which did not match the particular fit hypothesis used. These events include, but are not relegated to only being from: background events, poorly reconstructed events, or events with misidentified particles. This makes the confidence level a good parameter to cut on as doing so will remove a large number background and "bad" events while only losing a small portion good events.

Pull distributions are generated for every fit parameter for every (detected) final state particle involved in the fit. A pull is a measure of how much (and in what direction) the kinematic fitter had to alter, or pull, the value of that parameter in order to enforce energy-momentum conservation normalized to the error of that measurement. A pull value for the i^{th} fit parameter (z_i) is given by:

$$z_i = -\frac{\epsilon_i}{\sigma(\epsilon_i)}, \tag{1.6}$$

where $\epsilon_i = \eta_i - y_i$ is the difference between the value of the i^{th} parameter from the final iteration of the fitting routine, y_i and the measured value of the i^{th} parameter, η_i. The quantity σ represents the standard deviation, or error, of the parameter. Therefore, the i^{th} pull can be written as:

$$z_i = -\frac{\eta_i - y_i}{\sqrt{\sigma^2(\eta_i) - \sigma^2(y_i)}}. \tag{1.7}$$

Assuming that the errors of the parameters used for kinematic fitting are properly determined and all systematic errors have been corrected, the distribution of pull values (z_i values) will be Gaussian in shape with a width of one ($\sigma = 1$) and a mean value of zero ($\mu = 0$). Any systematic error in the quantity η_i will be seen as an overall shift away from zero. An overestimation or underestimation of the error of the quantity η_i will cause the pull distribution to be too narrow or broad, respectively [54].

The above describes ideal confidence level and pull distributions. When one begins using the kinematic fitter with their data, this is not the case. The scaling parameters applied to the covariance matrix (the covariance matrix will be discussed in the following subsection) are related to the tracking measurements made for each track, target and magnetic field and are therefore unique to every run period and must be determined as such.

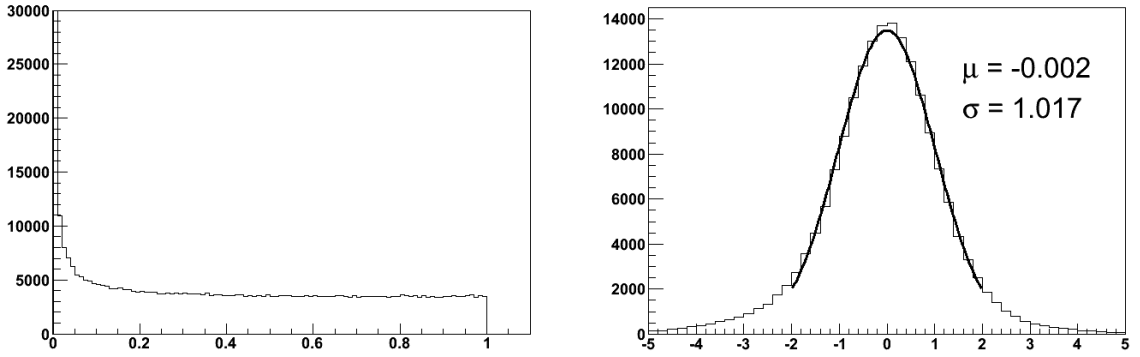

(a) Confidence Level Distribution

(b) Pull Distribution

Figure 1.4: Example of fit results coming from a fit to a fully reconstructed $p\pi^+\pi^-$ final state. (a) Shows an example of a confidence level distribution. A confidence level distribution (working with real data) peaks toward zero but flattens out toward one. (b) Shows an example of a pull distribution (the photon energy pull). Ideally, a pull distribution is Gaussian in shape around the origin with a mean (μ) of zero and a sigma (σ) of one.

This determination of the proper covariance matrix errors is an iterative process. As a starting point, one may use the scaling parameters from another run period (this analysis started with the g11a scaling parameters). These parameters can then be adjusted/modified, keeping track of all changes to the confidence levels and the pull widths. As these scaling parameters exist as arrays read in by the kinematic fitter, a simple script may be used in order to alter these parameters to be specific to one's data set.

When iterating through this process, one needs to keep track of the pull sigmas and the slope of the confidence level plots, specifically the *normalized slope*. This normalized slope is the slope of a linear fit to the confidence level distribution from [0.5,1] (50 % - 100 %) which has been normalized to the number of entries at the point 0.5 (the number of events possessing a confidence level of 50 %). The choice of the fit range used to calculate the normalized slope was determined with the expectation that the negative slope arising from the large number of events which resulted in poor fits flattens out at 50 %. This normalized slope is then defined as seen in Eq. (1.8) where a is the slope of a linear fit from [0.5,1] and b is the y-intercept.

$$\bar{a} = \frac{a}{(a/2) + b} \tag{1.8}$$

Checking the widths (σ's) of the pull distributions is as simple as fitting them to a Gaussian with a 2σ ($[-2, 2]$) fit range.

The quality of the covariance matrix errors for a particular data set can be determined thusly: Errors which are too large will result in a confidence level distribution having a positive slope between 0.5 and 1 and pull distributions with widths less than 1 ($\sigma < 1$). The positive slope of the confidence level distribution signifies that one is artificially increasing the number of events that fit, or pass, the fit hypothesis. In other words, the fitter is being

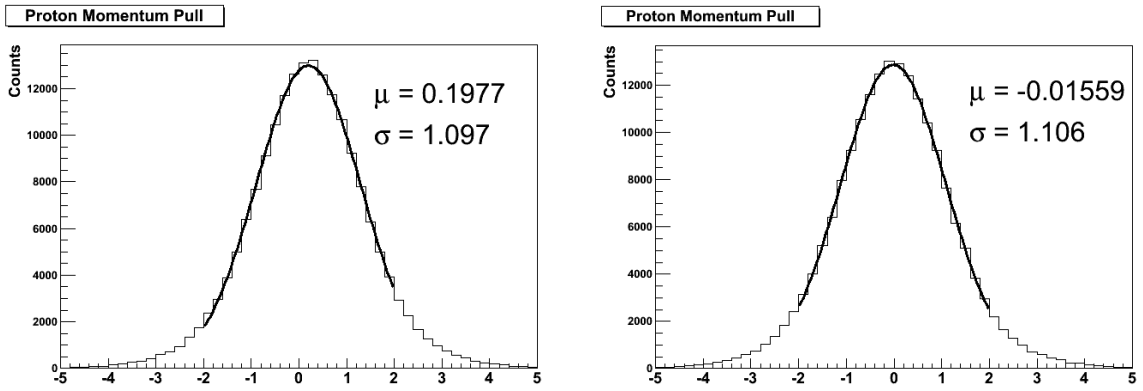

Figure 1.5: Pull distributions for the proton momentum for a $\gamma\ p \rightarrow p\pi^+\pi^-$ final state showing the sensitivity of the kinematic fitter to systematic effects. The distribution on the left, (a), was generated using one run (#048326) without alterations of the proton momentum. The distribution to the right was generated using the same run but after an alteration to the proton's 3-vector. This alteration was small (a 0.4 % increase) and is equivalent to a 2 MeV increase in the proton's momentum. The high degree of sensitivity of the kinematic fitter to systematic effects is clearly seen as this very small correction shifted the mean (μ) value from 0.1977 to -0.01559.

given too much freedom to alter the measured values of the particle's 4-vectors. If the determined and applied errors are too small, the confidence level plot will have a negative slope between 0.5 and 1 signifying that one is excluding possible good events (by not allowing the fitter enough "wiggle room"). The resulting pull distributions will then possess widths greater than 1 ($\sigma < 1$). If the determined and applied errors are appropriate (not too small, not too large), then the confidence level plot will be flat from 0.5 to 1 (resulting in a normalized slope of zero) and the pull distributions will have a sigma of 1 ($\sigma = 1$).

Systematic errors in the data can be seen and corrected by examining the mean values of the pull distributions. For example, the effects of the ELoss package as well as momentum corrections (described in Section 3.6) can be easily seen by monitoring the momentum pull distributions. An examination of the momentum pulls generated by the kinematic fitter shows off the fitter's sensitivity to small changes in the fit parameters. Pull distributions showing this sensitivity can be seen in Figure 1.5. These proton momentum pulls were generated using no momentum alterations for the proton (Fig. 1.5(a)) and a small alteration in momentum equivalent to a 2 MeV shift (Fig. 1.5(b)). This correction corresponds to a change that is smaller than the resolution of CLAS yet still results in a noticeable shift in the pull distribution. Therefore the sensitivity of the kinematic fitter surpasses the resolution of the detector systems. This was one of the reasons the kinematic fitter was used to generate momentum corrections. This process was also an iterative one involving a binning of the pull distributions (in $p_{\rm p}$, $\theta_{\rm lab}$, and $\phi_{\rm lab}$) that matched the binning of the corrections and a script to alter the momentum correction factors. Corrections were refined by generating correction factors, running over the data using these factors, fitting all of the binned pulls, extracting the mean values, generating new corrections based on the results of the previous iteration and repeating.

1.5.2 Use

Kinematically fitting an event requires a process involving several steps. The 4-vectors of the final state particles as well as the incident photon energy must first be extracted from the data. The resolution errors of the tracking measurements used for determining these 4-vectors are then used to build the tracking covariance matrix. Scaling parameters which serve to refine these resolution errors are then applied to the tracking covariance matrix to create a second matrix, the full covariance matrix. The event is then ready to be kinematically fitted.

Covariance Matrix. The covariance matrix used for kinematic fitting is built for every event using information from the TBER and GPID data banks and has the form seen below [54]. The TBER bank is used as it contains the errors pertaining to the measured values of the detected particle's momentum and the drift-chamber-specific angles lambda (λ) and phi (ϕ) which are sector dependent and describe the particle's track as it moves through the Drift Chambers. To obtain the magnitude of the 3-momentum of the final state particle, the GPID bank is used. The dimensions of the covariance matrix depend on the number of detected final state particles being used for the fit hypothesis. It is a square matrix of dimensions $(3n+1) \times (3n+1)$ where n is the number of detected final state particles. The extra row and column (the '+1') is reserved for containing the error in the measurement of the photon energy. The tracking resolutions regarding the detected final state particles are used to build 3×3 matrices along the diagonal of the covariance matrix, one for each detected final state particle. In these mini-matrices, the diagonal terms hold the "pure" (non correlated terms) measurements of momentum, lambda, or phi while the off-diagonal terms represent the correlation (mixing) of these measurements. The C's present in the generalized covariance matrix seen below represent the elements of the covariance matrix and are polynomials with values extracted or calculated from the data.

$$C = \begin{pmatrix} \sigma^2_{E_\gamma} & 0 & 0 & 0 & \cdots & 0 & 0 & 0 \\ 0 & C_1^{pp} & C_1^{p\lambda} & C_1^{p\phi} & \cdots & 0 & 0 & 0 \\ 0 & C_1^{p\lambda} & C_1^{\lambda\lambda} & C_1^{\lambda\phi} & \cdots & 0 & 0 & 0 \\ 0 & C_1^{p\phi} & C_1^{\lambda\phi} & C_1^{\phi\phi} & \cdots & 0 & 0 & 0 \\ \vdots & \vdots & \vdots & \vdots & \ddots & \vdots & \vdots & \vdots \\ 0 & 0 & 0 & 0 & \cdots & C_k^{pp} & C_k^{p\lambda} & C_k^{p\phi} \\ 0 & 0 & 0 & 0 & \cdots & C_k^{p\lambda} & C_k^{\lambda\lambda} & C_k^{\lambda\phi} \\ 0 & 0 & 0 & 0 & \cdots & C_k^{p\phi} & C_k^{\lambda\phi} & C_k^{\phi\phi} \end{pmatrix}$$

Photon Error. The energy of the photons are determined by using the 384 E-counter scintillator paddles contained in the E-plane of the Tagger. These scintillator paddles are arranged in an overlapping fashion such that each counter optically overlaps its adjacent neighbors by one-third of their respective widths, leading to a total of 767 bins in photon energy (767 E-bins). This configuration leads to an energy resolution of $r = 0.001 E_{\text{beam}}$ [46].

Due to the fact that the information regarding the incident photon's energy comes from a measurement made by a detector, there is an error that must be associated with the photon energy. If one assumes that this error is the same for all paddles then the error can be given by equation (1.9):

$$\sigma^2_{E_\gamma} = \frac{1}{2r}\int_{-r}^{r} E^2 dE = \frac{r^2}{3}, \tag{1.9}$$

where again, $r = 0.001 E_{\text{beam}}$. Therefore for the g8b run period, which used an electron beam with energy $\text{E}_{\text{beam}} = 4.559$ GeV, the associated error in photon energy is $\sigma^2_{E_\gamma} = 6.928$ MeV.

Momentum and Tracking Angle Error. The measurements made regarding the momentum and tracking angles (λ and ϕ) describe the path of the detected final state particles as they moved through the Drift Chambers of CLAS. These measurements, like all other measurements, carry with them an error. This error comes from several sources. Tracking errors which lead to inaccurate momentum (and angle) measurements, multiple scattering leading to differences between the measured angles and the angles at the interaction vertex, and the performance of the reconstruction code (the fitting of the tracks) being the main culprits. When an event is reconstructed, the reconstruction code includes the calculated errors but this calculation assumes a complete knowledge of the resolution of detector components which vary in a small amount from one run period to the other. Therefore it is necessary that the resolution of the detector components for the run period under analysis be completely determined. This true resolution comes in the form of scaling parameters. These scaling parameters are binned in sector number and θ_{lab} and are applied to the momentum, and tracking angle components of the tracking covariance matrix.

Once a fit is performed, the user has access to several fit results. These are: the fitted 4-vectors of the final state particles (except the missing particle if the fit hypothesis involved a missing particle), the fitted photon energy, the confidence level of the fit, and the pull value for each pure element of the covariance matrix (elements along the diagonal of the covariance matrix). The information returned by the fitter can then be used to check the quality of the performed fit as well as provide quantities on which cuts may be imposed during the course of the analysis.

1.6 Momentum Corrections

Since the CLAS detector is not a perfect detector, corrections for momentum must be determined for every run period. This mainly is a result of unknown variations in the magnetic field provided by the Torus Magnet as well as inefficiencies and misalignments of the Drift Chambers. As mentioned before, the momentum corrections were determined using the kinematic fitter, specifically looking at the momentum pull distributions for the topology $\vec{\gamma}\, p \to p\, \pi^+ \pi^-$ and have been incorporated into the various analyses which use the g8b data set.

To properly determine the momentum corrections for the g8b data set, these pulls (and corresponding correction factors) must be binned in momentum (p) and the lab angles θ and ϕ of the particle to be corrected (in this case, the proton). The binning used to determine these correction factors was determined based upon the observed distribution

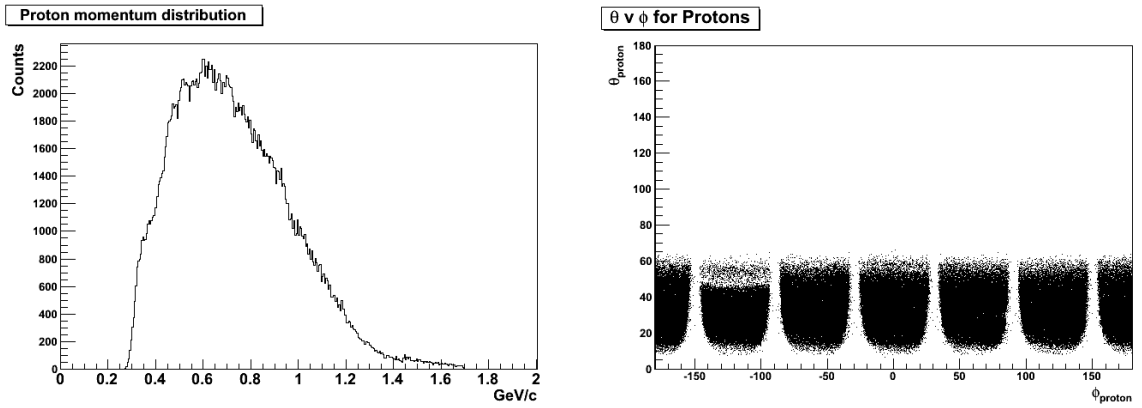

(a) (b)

Figure 1.6: The observed distributions of momentum (a), $\theta_{\rm lab}$ and $\phi_{\rm lab}$ (b) for the proton used to determine the binning for momentum corrections. Distributions were produced for $p\pi^+\pi^-$ events contained in run #048326 (a) and #048229 (b) which pass a confidence level cut of 1 %. The region seen in (b) showing low statistics for $-150^\circ < \phi_{\rm proton} < -110^\circ$ is seen in several runs and can be attributed to dead wires in the Drift Chambers.

of momentum, $\theta_{\rm lab}$ and $\phi_{\rm lab}$ for the proton seen in Figure 1.6. The momentum binning utilized 6 momentum bins covering a range of 0.2 GeV to 1.7 GeV:

- 0.00 GeV/$c < p_{\rm proton} \leq$ 0.45 GeV/c
- 0.45 GeV/$c < p_{\rm proton} \leq$ 0.70 GeV/c
- 0.70 GeV/$c < p_{\rm proton} \leq$ 0.95 GeV/c
- 0.95 GeV/$c < p_{\rm proton} \leq$ 1.20 GeV/c
- 1.20 GeV/$c < p_{\rm proton} \leq$ 1.45 GeV/c
- 1.45 GeV/$c < p_{\rm proton}$,

with the angle binning utilizing 7 bins in θ_{lab} (10° - 70°) and 18 bins in ϕ_{lab} (covering the full range of ϕ_{lab}). First, the proton momentum pulls and correction factors were binned in the above manner with the correction factors existing in an array (each possessing a default value of 1). The pull distributions were then individually fitted to a Gaussian and the resulting mean value (μ) and width (σ) recorded into another array. Then through the examination of the mean values resulting from the (Gaussian) fits of the pulls and determining the direction and magnitude in which these mean values should be moved, the correction factors were altered to either a value above or below 1 with these new correction factors being read into a new array. These new correction factors were then applied to the data, the pulls regenerated and then fit again to determine whether further corrections were needed. For example: if the proton momentum pull has a mean value that is above zero, then for the majority of the fits, the kinematic fitter is increasing the proton's momentum in order to satisfy

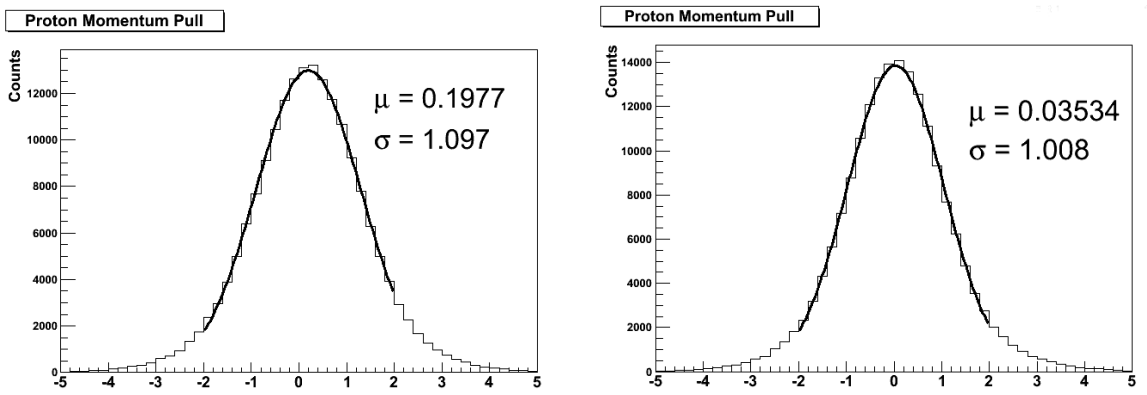

(a) Without momentum corrections

(b) With momentum corrections

Figure 1.7: Proton momentum pulls without momentum corrections (a) and with momentum corrections (b) as extracted from the fitter for a fit to a $\vec{\gamma}p \rightarrow p\pi^+\pi^-$ final state. After application of the final momentum corrections, the pull becomes symmetric and has a mean value close to zero. Produced using a full run (#048326).

energy-momentum conservation. In this case, the correction factor should be greater than one such that the fitter *pulls* the momentum of the proton equally in both directions. The same course of logic may be applied to a pull distribution with a (fitted) mean value that is negative. This mean value indicates that the fitter is decreasing the proton momentum the majority of the time. Therefore the appropriate correction factor would decrease the proton's momentum before it is kinematically fitted. Once these correction factors have been determined, they are applied to the 3-momentum of the final state particles thereby correcting its momentum. The effect of the momentum corrections on the momentum pull of the proton can be seen in Figure 1.7.

1.7 Tagger Sag

The Hall B tagging system is an invaluable tool for determining the energy of the photons that are incident on the target. This detection system, however, is not beyond the need for corrections. It has been seen in the g8b data set (as well as in past experiments) that there is a physical sagging of the support structures used to support the E-counter scintillator bars in the Tagger hodoscope which has been attributed to gravitational forces [55]. The consequence of this sagging is a misalignment of the scintillator bars which leads to a mis-measurement of the scattered electron's energy. This mis-measurement must then be compensated for via an energy-dependent photon energy correction.

The energy correction used in this analysis assumes that the angles measured by the CLAS detector are correct. This assumption of correctness in angle measurement allows the determination of momentum and energy correction factors from a set of four equations with four unknowns within the constraints of momentum and energy conservation using the reaction $\gamma p \rightarrow p\pi^+\pi^-$.

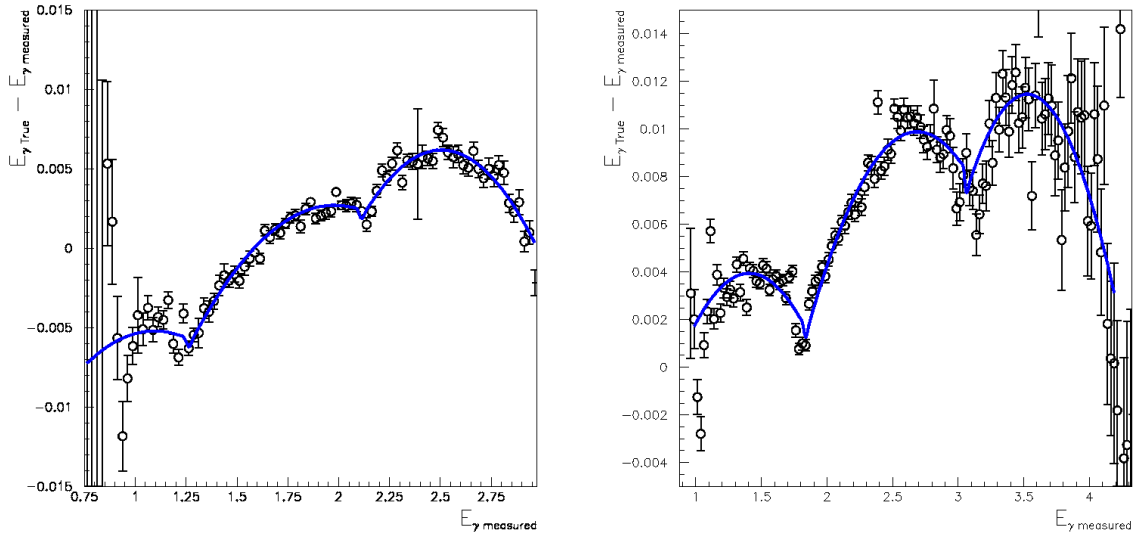

(a) g1c (b) g8b

Figure 1.8: A plot of the difference between the calculated photon energy and the measured photon energy as a function of incident photon energy using the g1c data set (a) and the g8b data set (b). The effects of the sagging of the E-counter scintillator support structures can be seen in the "humps".

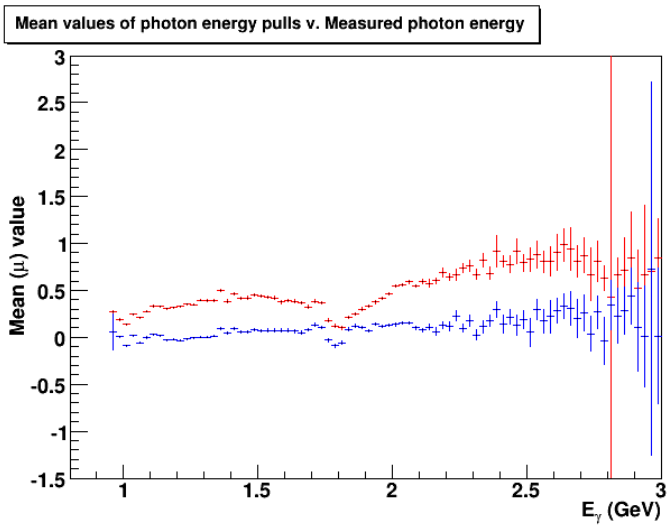

Figure 1.9: Superimposed on one another are the mean values of the photon energy pulls as extracted from the kinematic fitter versus the measured photon energy. The red points represent the mean values of the photon energy pulls before the correction and the blue points represent the mean values after the application of the photon energy corrections. These pull distributions were generated using one run for each coherent edge energy for a $p\pi^+\pi^-$ final state. The "humps" after this correction is applied are suppressed and the mean values shift toward zero. The sharp dip seen near $E_\gamma = 1.8$ GeV represents an effect which could not be overcome using these corrections.

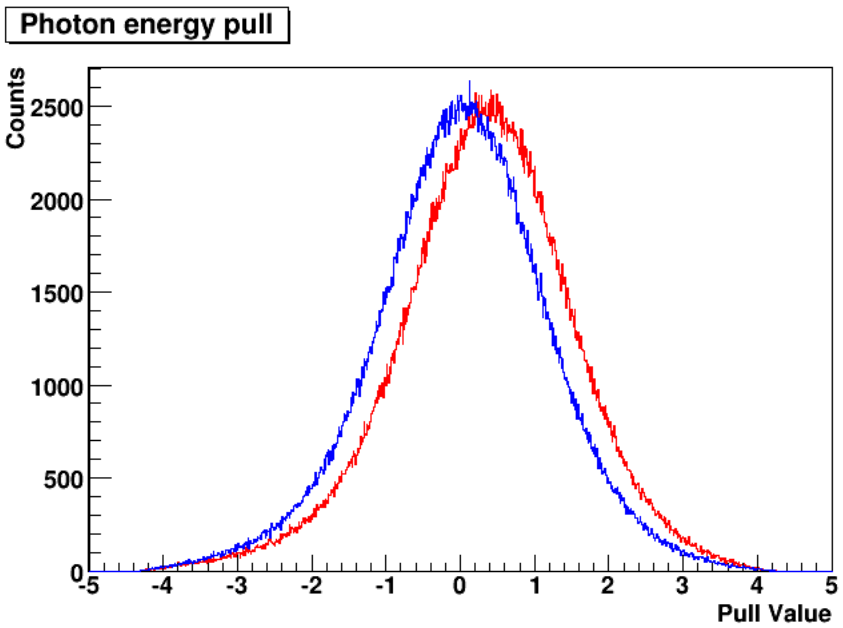

Figure 1.10: Superimposed on one another are the y-axis projections of the photon energy pulls used make Figure 1.9. These photon energy pulls were extracted from the kinematic fitter with (blue) and without (red) the energy-dependent photon corrections for $p\pi^+\pi^-$ final states. After the application of the photon energy corrections, the σ of the Gaussian fit changed from 1.087 to 1.069 and the μ improved from 0.374 to 0.042.

The sagging of the hodoscope's support structures can be seen by comparing the calculated photon energy, E_{true} (which for this study was the photon energy returned by the kinematic fitter) and the measured photon energy, E_{measured}, as a function of photon energy (E_{measured}) as seen in Figure 1.8. This sagging is demonstrated by the "humps" of the ($E_{\text{true}} - E_{\text{measured}}$) values with the vertical support structures (which support the sagging beams on which the E-counter scintillators rest) of the detector plane evidenced by the sharp dips.

The algorithm for a simple iterative routine to determine the corrections to the incident photon energies using g1c and g8b data is described in full details in the CLAS analysis note *"Correction to the incident photon energy for g8b data"*, CLAS-Note 2009-030 [56]. Some details on the procedure are also discussed in the analysis note *"Data analysis technique for obtaining $\gamma p \to n\pi^+$ and $\gamma p \to p\pi^0$ beam asymmetries from the g8b running period."* Corrections applied to the photon energies typically are on the order of a few MeV and greatly improve the quality of the data. The before and after effects of these corrections can be seen in Figure 1.9 with the effects on the photon energy pull distributions being shown in Figure 1.10. These two histograms were generated using the kinematic fitter and therefore are very sensitive to systematics. The plot seen in Figure 1.9 is a distribution of the mean values of the photon energy pulls generated from fitting to a $p\pi^+\pi^-$ final state versus the measured photon energy. The effects of the sagging can be seen in this plot as deviations from zero. Seen in Figure 1.10 is the y-projection of the photon pull distributions used in Figure 1.9.

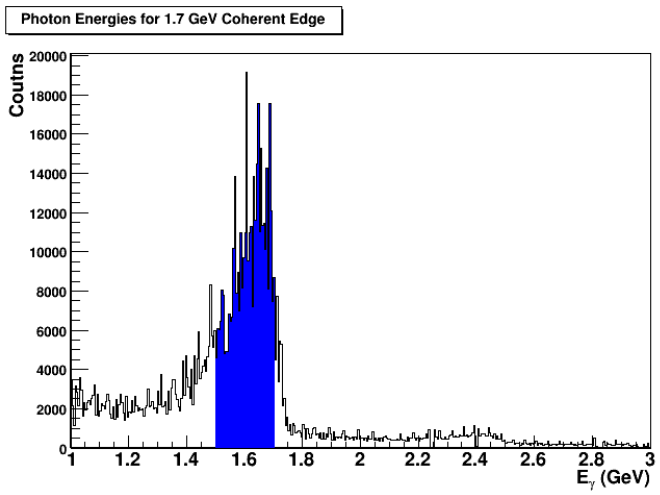

Figure 1.11: Photon energies taken from data (run #048544) produced with a coherent edge energy of 1.7 GeV using events passing a 5 % confidence level cut for all final state topologies. The highly polarized photons in this coherent edge energy reside in the region between 1.5 and 1.7 GeV and therefore cuts are applied to use only these photons.

1.8 Cuts

Once the events that match one of the four topologies have been obtained and kinematically fitted, it is necessary to impose a series of cuts before extracting polarization observables. These cuts will serve to further refine the data sample and help remove accidental events and other things that corrupt the data set. In the histograms contained in this section, the blue region represents the data which passes the imposed cuts.

1.8.1 Photon Energy Cut

The first cut that is applied is a cut on the photon energy. While photons are produced with a wide range of energies, the highly polarized photons occur in a 200 MeV wide window (the upper limit of which is the coherent edge energy) with this window occupying five different positions (the five different coherent edge energies). A cut on the upper and lower limits of this window ensures that the events passing this cut came from a highly polarized photon in the coherent peak (Fig. 1.11 shows an example of such a cut). This leads to a total of 5 photon energy cuts (one for each dataset with a fixed value of the (nominal) coherent edge energy):

- 1.1 GeV $< E_\gamma <$ 1.3 GeV
- 1.3 GeV $< E_\gamma <$ 1.5 GeV
- 1.5 GeV $< E_\gamma <$ 1.7 GeV
- 1.7 GeV $< E_\gamma <$ 1.9 GeV
- 1.9 GeV $< E_\gamma <$ 2.1 GeV

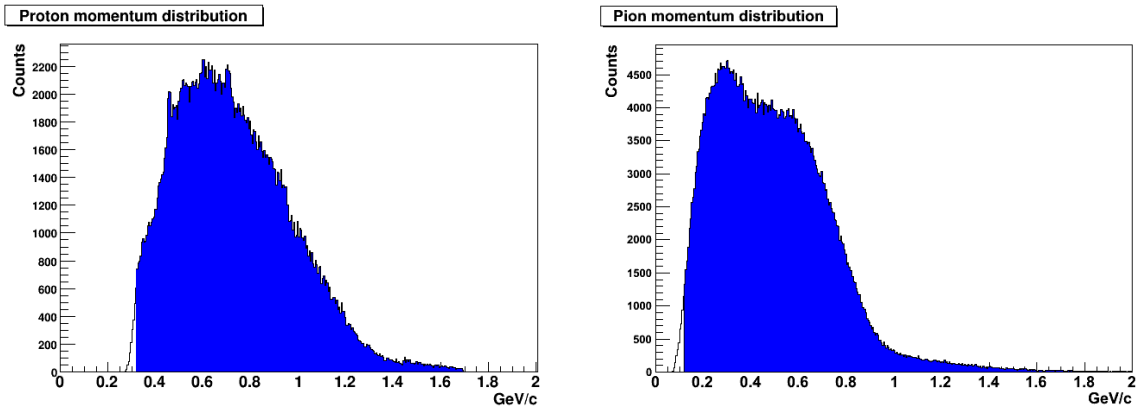

(a) All protons (b) All pions

Figure 1.12: Momentum distributions showing the range of momentums for all (a) protons and (b) pions. Generated for $p\,\pi^+\pi^-$ events passing a confidence level cut of 1 % using one full run: #048326.

Since the coherent edge varies with time, an additional event-based cut was applied:

$$\text{event edge} - 200\ \text{MeV} \ < \ E_\gamma \ < \ \text{event edge}\,. \tag{1.10}$$

This cut is derived from overlap studies between datasets with different nominal coherent edges and discussed in more details in the analysis note *"Consistency corrections to the linear photon polarization for g8b data"* [63]. It has been verified using the reaction $\gamma p \to p\pi^+\pi^-$ from this analysis.

1.8.2 Final State Momentum Cut

A low momentum particle moving through CLAS presents a problem to the reconstruction of the event. These particles' possession of low momentum can affect the accuracy of the ELoss corrections applied to them. More importantly however is the fact that particles with this characteristic have a low-acceptance for detection. Using these acceptance limitations, cuts in the proton momentum and the momentum of the pions were determined and applied. This cut requires all protons have a minimum momentum of 320 MeV/c ($\mathrm{p}_{\,\mathrm{proton}} > 320$ MeV/c) and all pions have a momentum of at least 125 MeV/c ($\mathrm{p}_{\pi^\pm} > 125$ MeV/c). These cuts may be seen in Figure 1.12.

1.8.3 Vertex Cut

The next set of cuts imposed in this analysis involves the vertex information for each final state particle and event. This set of cuts then ensures that the physics event originated in the target cell and all particles are from the same event.

Position. The dimensions of the target cell are well defined quantities. Therefore cuts on the vertex positions of all the final state particles which mimic these dimensions ensure that the event originated in the target cell. The first of these cuts is on

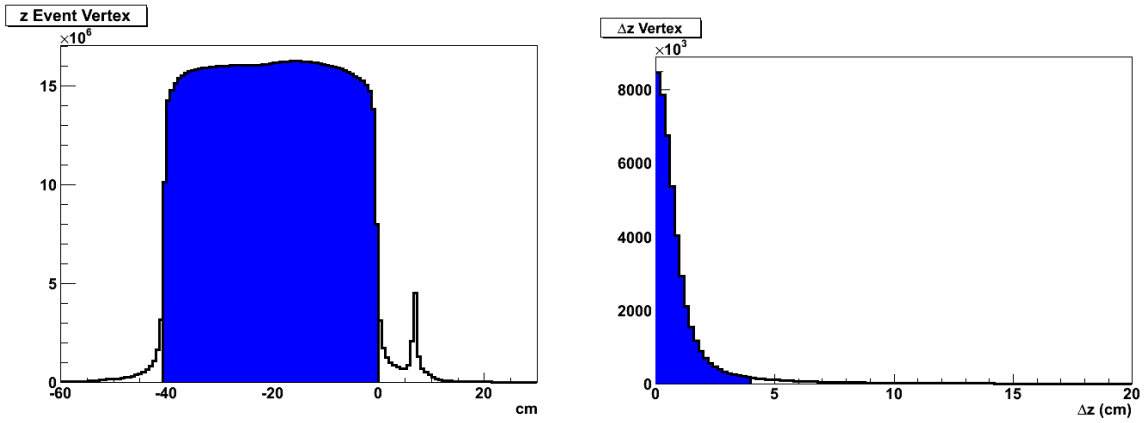

(a) (b)

Figure 1.13: (a) The vertex z-position (axis along the beam line) of all reconstructed particles showing the length and position of the target cell. The peak at ≈ 7 cm shows the exit window of the scattering chamber (the vacuum tight chamber in which the target cell resides). Events must have a z-vertex occurring between 0 and -40 cm. (b) A distribution showing the differences between the vertex z-position of the π^+ and π^- for a $\pi^+\pi^-(p)$ final state. The cut applied to this difference requires that it be no more than 4 cm.

the z-component of the vertex position for all final state particles. The g8b target was a 40 cm long target with its center located at z $= -20$ cm (Figure 1.13(a)). This vertex cut therefore requires that $-40 <$ z$_{\text{all particles}} < 0$. The next cut that is applied involves comparing the vertex z-positions of all final state particles. This cut requires that the z-component of the vertex positions of all final state particles be within 4 cm of each other ($|$ z$_{\text{particle X}} -$ z$_{\text{particle Y}} | < 4$ cm) (Figure 1.13(b)). The third cut on the vertex position(s) involves the x- and y-components of the event itself. This cut makes sure that the event originated no more than 2 cm from the axis of the beamline (the z-axis) ($x^2 + y^2 < 4$ cm). A distribution of event vertices in x, y, and x-y can be seen in Figure 1.14.

Timing. Timing information regarding the vertex time for all final state particles is used by making a cut on the time stamp of the particles' vertex. This cut is the same for all final state particles and further aids in removal of accidentals by requiring that the vertex time (for all final state particles) be between -10 ns and 20 ns (Figure 1.15).

1.8.4 Angular Cuts

The CLAS detector, while having a large acceptance, does not possess a *completely* 4π solid angle coverage. The existence of the forward-angle hole in CLAS means that it lacks acceptance from $0^\circ < \theta < 8^\circ$ and in the backward region lacks acceptance at angles greater than $\theta = 142^\circ$. These limitations combined with the observed distributions of the θ values for all final state particles (Figures 1.16 and 1.17) determine the angular cuts used. The applied cut requires that the lower limit (in θ) for all final state particles be $\theta > 10^\circ$ and the upper limit for pions be $\theta < 120^\circ$.

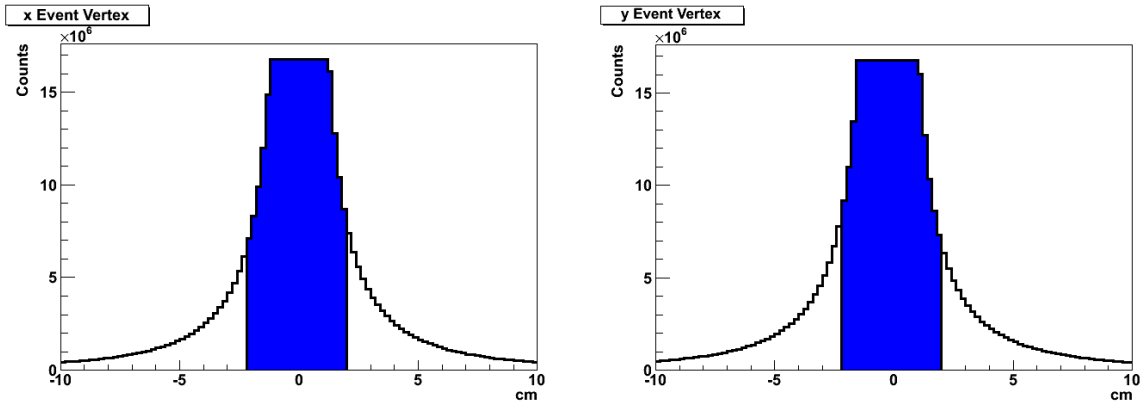

(a) x-Vertex

(b) y-Vertex

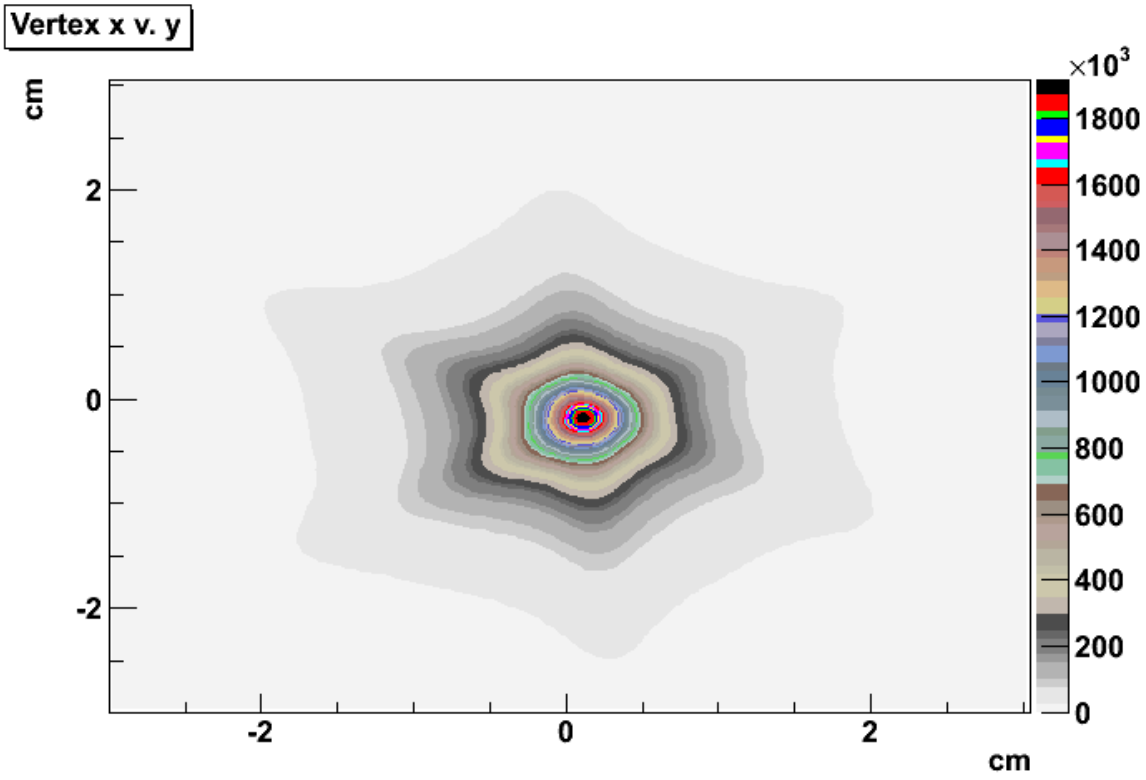

(c) x versus y Vertex

Figure 1.14: Plots showing the x- and y- vertices of all final state particles. (a) Shows the x-vertices, (b) shows the y-vertices. Histogram (c) is a plot of the x versus y vertices of the reconstructed final state particles. The vertex cut applied requires that the x- and y-components of the event are within a circle of radius 2 cm around (0,0).

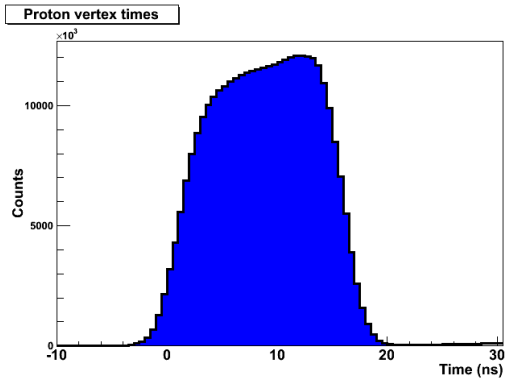

(a) Proton Vertex Time

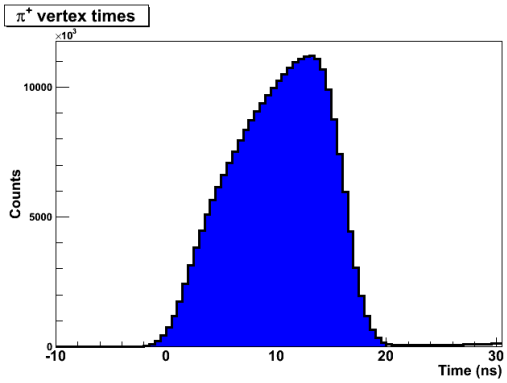

(b) π^+ Vertex Time

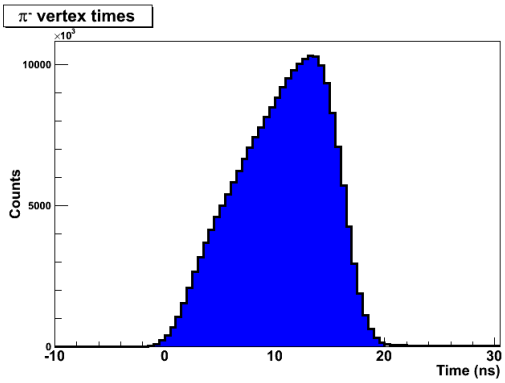

(c) π^- Vertex Time

Figure 1.15: Vertex times of final state particles. A loose cut of (−10,20) ns is enforced to help remove accidentals from the data set.

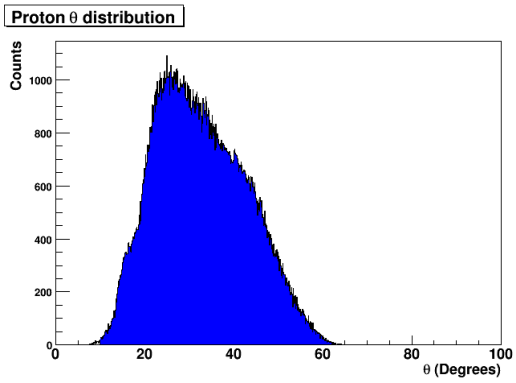

(a) Proton θ range.

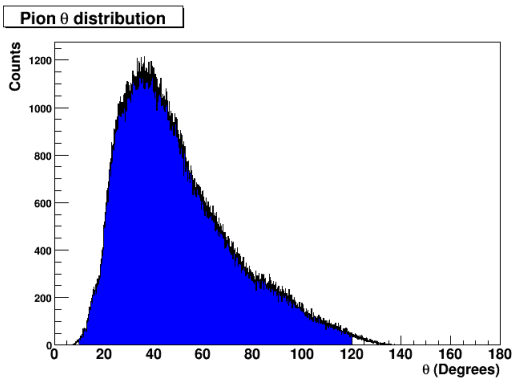

(b) Pion θ range.

Figure 1.16: Distributions showing the values of θ for all (a) protons and (b) pions. Generated for $p\,\pi^+\pi^-$ events passing a confidence level cut of 1 % using one full run #048326.

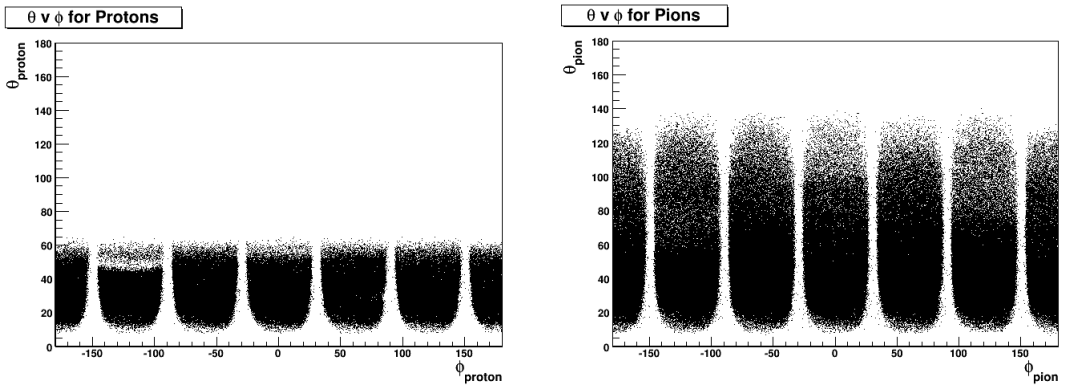

(a) θ v ϕ for Protons (b) θ v ϕ for Pions

Figure 1.17: Distributions showing θ v ϕ for protons ((a)) and pions ((b)). The six structures apparent in the histograms represent the six sectors of CLAS. Generated for $p\,\pi^+\pi^-$ events passing a confidence level cut of 5 % using one full run: #048326. The region seen in (b) showing low statistics for $-150^\circ < \phi_{\,\mathrm{proton}} < -110^\circ$ is seen in several runs and can be attributed to dead wires in the Drift Chambers.

1.8.5 Other Cuts

'ngrf' and 'tagrid' Cuts. Another cut imposed on the g8b data set during this analysis is one that uses specific bank variables. These variables can be found in the GPID bank with the names 'ngrf' and 'tagrid' with both being in reference to the incident photon. The 'ngrf' variable indicates how many of the candidate photons the reconstruction code found which passed the reconstruction timing cut for finding the incident photon (using the process outlined in Section 3.3). The 'tagrid' provides an index to the location of that photon in the TAGR bank (therefore pointing to the correct photon). The cut on the 'ngrf' value imposed on all final state particles requires that they all have a value of one (ngrf=1). This means that for every final state particle, there was only one photon that was found to pass the timing requirements (occasionally the reconstruction code will find two photons that are close enough in time for a time-based selection to be inconclusive). For the 'tagrid' variable, the requirement that the value of this variable be the same for all final state particles guarantees that the reconstruction code found the same photon for all final state particles (as the photon determination occurs for every detected final state particle). These cuts ensure that the events being analyzed include a successful determination of the incident photon and that this photon is the same for all final state particles thus leading to a well-defined initial state.

The remaining background from accidentals can be estimated from time-difference plots. Figure 1.18 (left side) shows the coincidence-time distribution of tagged photons for the raw data without any cuts (blue distribution) and after applying all cuts (green distribution). The fraction of accidental coincidences can be estimated by comparing the yields from the central peak with the yields from neighboring beam buckets. The fraction is about 4 % for the raw data and at most 1.7 % after all cuts without the one-photon requirement (NGRF = 1). The additional one-photon cut removes all side buckets and reduces the fraction of accidental coincidences to a negligible level (green distribution).

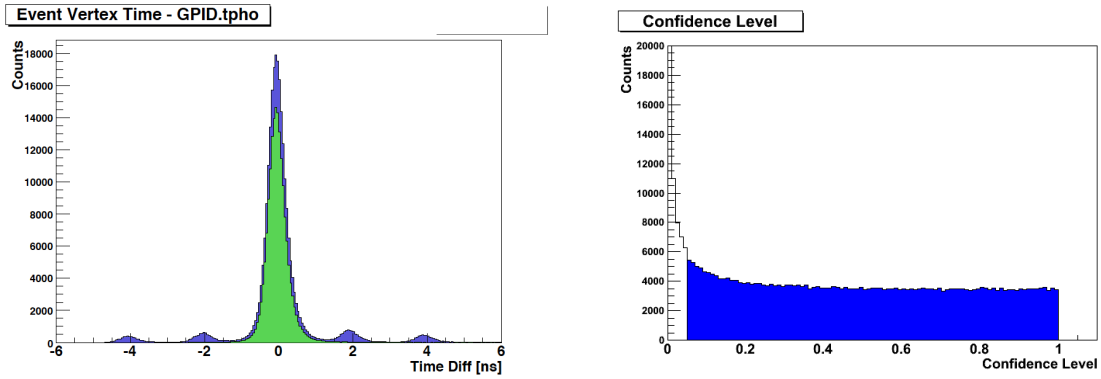

Figure 1.18: Left: A time-difference plot of tagged photons before and after all cuts. The fraction of accidental coincidences can be estimated by comparing the yields from the central peak with the yields from neighboring beam buckets. Right: A confidence level distribution generated from run #048326 for a $p\,\pi^+(\pi^-)$ final state showing the imposed confidence level cut of 5 %.

Confidence Level Cut. By performing a cut on the confidence level, one can easily remove many of the background events, poorly reconstructed events as well as events with misidentified particles. A confidence level cut of 5 % was imposed in this analysis (shown on the right side of Fig 1.18). This cut removes much of the background events while ideally only cutting out 5 % of the good events.

1.9 Results of Corrections and Cuts

The process of developing and applying energy and momentum corrections during the course of an analysis serves the purpose of correcting for the effects of the experimental setup, therefore resulting in a data set that is as nature intended it. Additionally, determining and enforcing cuts in an analysis serves not only to remove the remaining effects of the experimental setup but also to remove the contribution to the data set from physics events not of interest to the analysis (the background).

1.9.1 Study of Background in the Mass Distributions

The background may be comprised for example of accidental events (where a detected final-state particle was attributed to an event to which it does not belong), events with an incorrect initial state (misidentification of a photon) and/or events originating from interactions with matter other than the target material. A typical method of observing the background is to choose a final state topology and construct the missing mass of that topology. A single cut on the confidence level greatly reduces this background but does not entirely remove it. In particular, a CL cut does not remove much background under the missing-mass peak since these background events behave kinematicly very similarly to the "good" events. In general, through the application of vertex position, vertex timing, photon identification variables, angular and momentum cuts as well as a CL cut, the background can be greatly reduced or, as in the case of this analysis, almost entirely removed (the

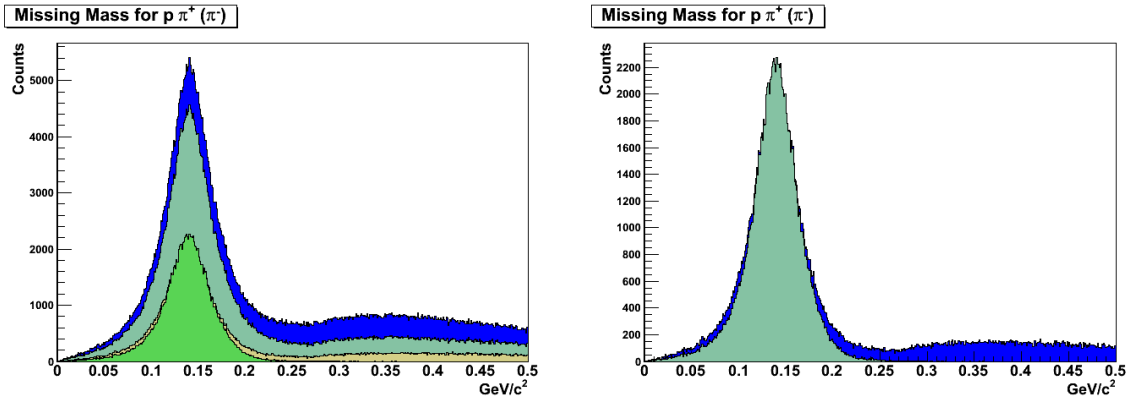

(a) Before Cuts

(b) After Cuts

Figure 1.19: A missing mass plot for the final state topology $p\,\pi^+(\pi^-)$ generated from run #048326. Left side: (blue) no cuts; (greenish-blue) cuts on the initial state (*ngrf* and *tagrid*); (tan) additional cuts on angle, momentum, and vertex of the final-state particles; (green) all previous cuts and a CL cut of 5 %. Right side: (blue) all cuts without a CL cut of 5 %, corresponding to the tan distribution on the left; (greenish-blue) all cuts including the CL cut. The background events are reduced to a negligible contribution via the application of these cuts imposed on the final state measurements.

background is negligible after all cuts are imposed). Previous CLAS-two-pion analyses also considered their missing-mass spectra background-free [57].

The missing mass distribution seen in Figure 1.19 was generated for all $p\,\pi^+(\pi^-)$ events in run #048326 with a π^- escaping undetected (Topology 1). The left side illustrates the effect of all the cuts. The blue distribution is the "raw" distribution without any cuts imposed. The greenish-blue distribution shows the effect of the cuts imposed on the initial state, i.e. cuts on the variables *ngrf* and *tagrid*. The signal height is reduced by only about 15 %, whereas the background is reduced by about 40-50 %. This indicates that most of the background consists of so-called accidentals. In the next step, angle, momentum, and vertex were imposed in addition to the previous cuts; the distribution in tan shows the corresponding effect. Although these additional cuts reduce the signal substantially, they reduce the background even more. It hardly extends to the actual signal peak anymore. Finally, the fourth distribution (plotted in green) includes all cuts imposed on the events, in particular the CL cut of 5 %. The latter cut somewhat improves the resolution of the peak and, more importantly, renders the background underneath the signal negligible.

The right side of Figure 1.19 zooms in. The blue distribution corresponds to the tan distribution in the left plot and the greenish-blue distribution corresponds to the green distribution of Figure 1.19 (left). It can be seen that the final CL cut slightly improves the resolution and that the signal region can be considered background-free.

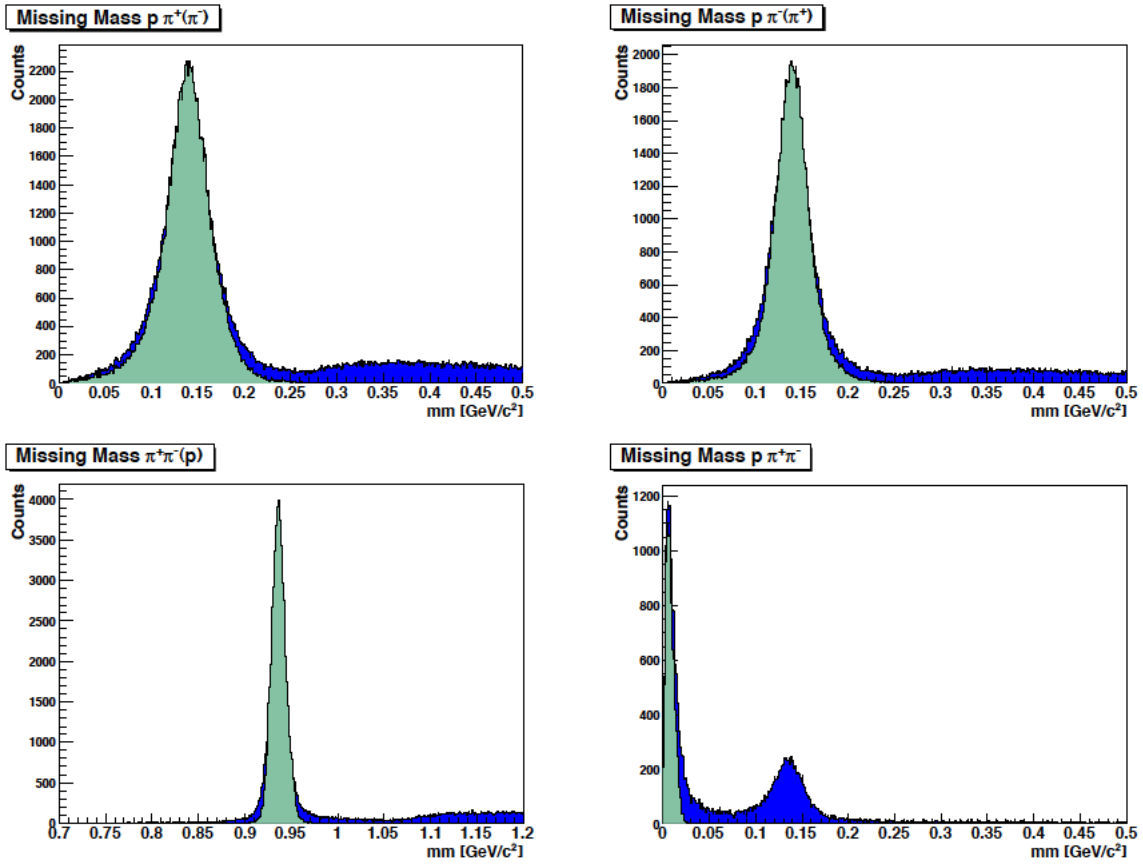

Figure 1.20: Missing mass distributions for all final-state topologies generated from run #048326: (blue) all cuts without a CL cut and (greenish-blue) all cuts including a CL cut of 5 %. The background events are reduced to a negligible contribution via the application of cuts imposed on the final state measurements.

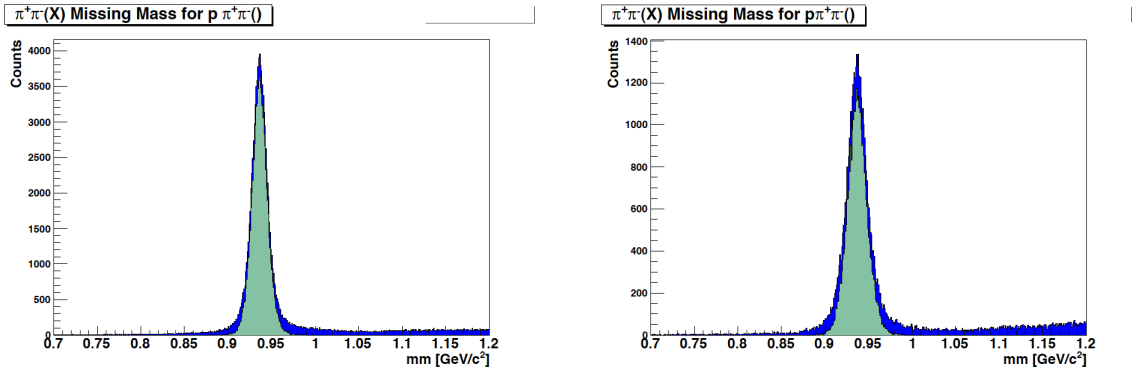

Figure 1.21: Missing-proton peaks for Topology 4 where all final-state particles have been detected. Generated from run #048326 (1.3 GeV dataset, left) and from run #048407 (2.1 GeV dataset, right). Symmetric peaks at the proton mass can be seen.

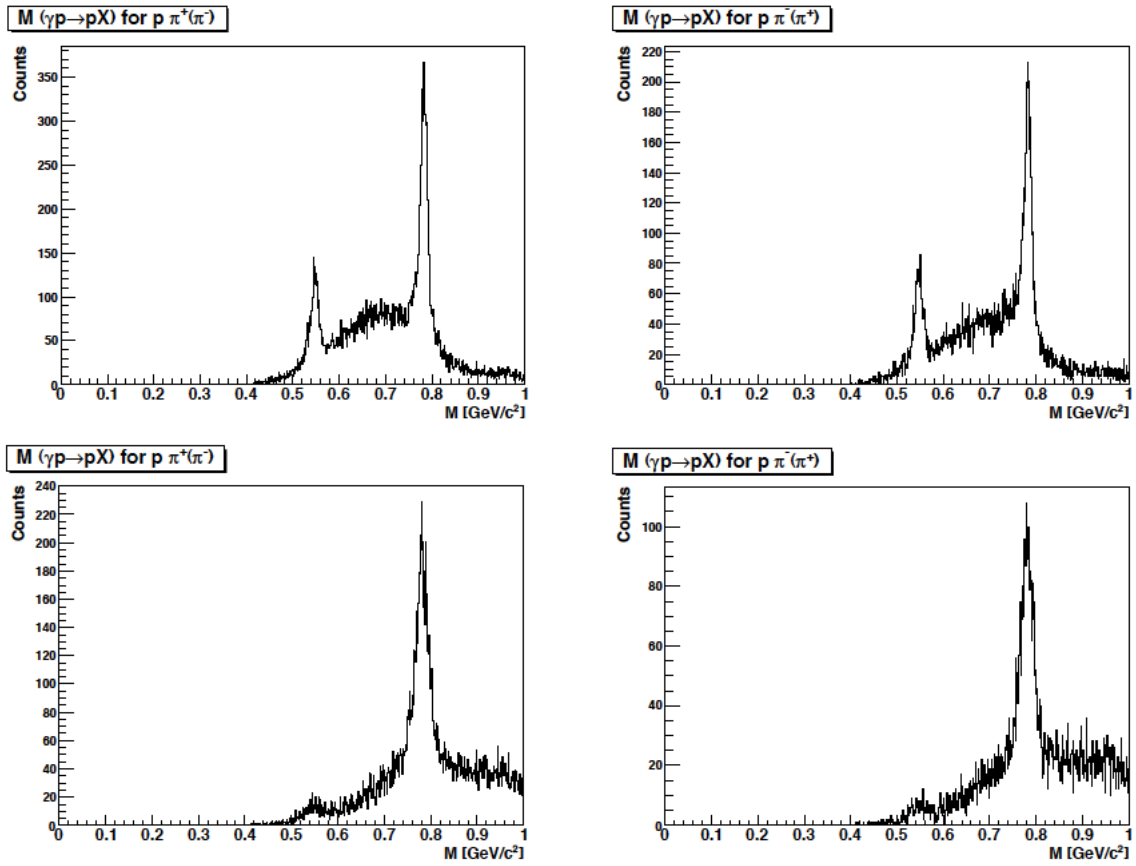

Figure 1.22: Missing mass distributions in the reaction $\gamma p \rightarrow p\,X$ where the missing mass has been restricted in the reaction $\gamma p \rightarrow p\pi\,X$ to $0.25 < X < 0.5$ GeV/c^2 consistent with the mass range of the top row in Figure 1.20. For the top row, run #48326 (1.3 GeV dataset) has been chosen and for the bottom row, run #48407 (2.1 GeV dataset). The left plots represent Topology 1 (missing π^-) and the right plots Topology 2 (missing π^+). The peaks for the η and ω are clearly visible and are dominating the spectra.

Figure 1.20 shows missing-mass distributions for all four topologies using run #48326 of the 1.3 GeV dataset. The blue distributions represent the missing mass for *all cuts applied without CL cuts* and the green distributions the missing mass for *all cuts applied including the final CL cuts of 5 %*:

Top left for $\gamma p \rightarrow p\pi^+\pi^-_{\rm miss}$: A clear peak for the π^- can be seen.

Top right for $\gamma p \rightarrow p\pi^+_{\rm miss}\pi^-$: A clear peak for the π^+ can be seen.

Bottom left for $\gamma p \rightarrow p_{\rm miss}\pi^-\pi^+$: A clear peak for the proton can be seen.

Bottom right for $\gamma p \rightarrow p\pi^+\pi^-$: A peak for the π^0 is seen which disappears after the CL cut due to energy-momentum conservation.

Accidentals represent a negligible contribution to the background. The size of the remaining (already very small) background close to the missing-mass peaks varies somewhat

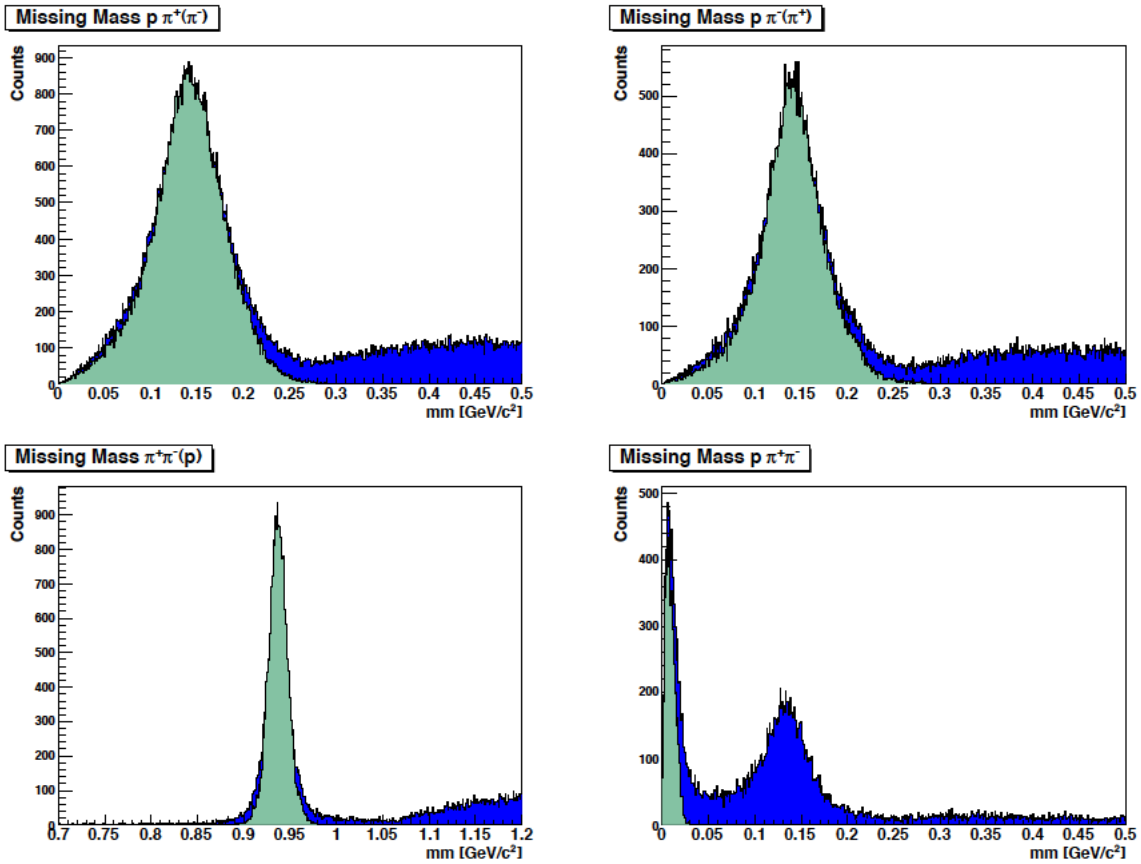

Figure 1.23: Missing mass distributions for all final-state topologies generated from run #048407 at higher energies (2.1 GeV dataset): (blue) all cuts without a CL cut and (greenish-blue) all cuts including a CL cut of 5 %. The background events are reduced to a negligible contribution via the application of these cuts imposed on the final state measurements.

and is essentially zero for Topology 3 (Fig. 1.20, bottom left). We also observe that the kinematic fitter improves the resolution of the missing-mass peaks as expected: The peaks become more narrow.

Figure 1.21 shows missing-proton peaks for Topology 4. All particles have been detected, but the proton has been artificially left out. The left side shows the distribution for run #48326 from the 1.3 GeV dataset and the right side shows the distribution for run #48407 from the 2.1 GeV dataset. Symmetric peaks at the proton mass can be observed.

The background in the top row of Figure 1.20 (before CL cuts) consists almost entirely of events where one or more particles in addition to the π^- (left) or the π^+ (right) have escaped detection. Good examples are the reactions $\gamma p \to p\eta \to p(\pi^+\pi^-\pi^0)_\eta$ and $\gamma p \to p\omega \to p(\pi^+\pi^-\pi^0)_\omega$ with the π^0 missing in addition to either the π^- or the π^+. Such background reactions cannot contribute to the central region of the missing-mass peak and are completely cut out by the CL cuts because they are kinematically different. To illustrate the contributions from these background reactions, Figure 1.22 shows missing masses in the

reaction $\gamma p \to p\,X$ where the missing mass has been restricted in the reaction $\gamma p \to p\pi\,X$ to $0.25 < X < 0.5$ GeV/c^2 consistent with the mass range of the top row in Figure 1.20. For the top row of Figure 1.22, run #48326 (1.3 GeV dataset) has been chosen and for the bottom row, run #48407 (2.1 GeV dataset). Moreover, the left plots represent Topology 1 (missing π^-) and the right plots Topology 2 (missing π^+). The peaks for the η and ω are clearly visible and are dominating the spectra.

Other hadronic reactions also strongly contribute, e.g. $\gamma p \to \Delta^+\eta \to (p\pi^0)_\Delta\,(\pi^+\pi^-\pi^0)_\eta$, where two π^0 mesons are lost. The cross section of this reaction is comparable (a few μb) with single-η and ω production. Figure 1.23 shows the missing-mass distributions for all topologies (similar to Fig. 1.20) for higher energies (using run #48407 of the 2.1 GeV dataset). Since more hadronic reactions contribute with increasing energy, e.g. $\gamma p \to \Delta^+\rho^0 \to (p\pi^0)_\Delta(\pi^+\pi^-)_\rho$ and $\gamma p \to \Delta^+\omega \to (p\pi^0)_\Delta(\pi^+\pi^-\pi^0)_\omega$ above $E_\gamma \approx 1.7$ GeV, the blue background to the right of the plot is slightly increased relative to the missing-mass peak. However, the background under the peak is still negligible because competing hadronic reactions are completely cut out by the CL cuts. The background in the distribution for Topology 3 (before CL cuts) may consist of a missing baryon, e.g. the $\Delta(1232)^+$ in $\Delta^+\rho^0$ production. The $\Delta\eta$ final state could also contribute to this topology. There is visibly no overlap between the missing-mass peak for the proton and the background rising at a mass of about 1.06 GeV.

1.9.2 Kinematic Fitting

The confidence level and pull distributions reveal the quality of systematic corrections as well as how well the covariance matrix errors were determined. Therefore to determine the quality of the fits, these two quantities are examined. The confidence level distributions produced in this analysis can be found in Figure 1.24. These confidence level distributions show the typical peak at zero (corresponding to poor fits, these are cut from the analysis via the confidence level cut) and a flat behavior from $[0.5, 1.0]$. Distributions seen in Fig. 1.25 show the normalized slopes (given by Eq. (1.8)) of the confidence level distributions for each final state topology. Each plot shows a distribution centered around zero. This is a strong indication that the covariance matrix errors are correct.

To provide a second check to verify if the covariance matrix errors have been properly determined, the pull distributions are examined. Figure 1.26 shows all pull distributions resulting from a fit to a $p\,\pi^+\pi^-$ final state for events in run #048326. These pulls have been fitted with a Gaussian distribution from $[-2, 2]$. The resulting fits show a σ close to one, indicative of the covariance matrix errors being properly determined. Also seen in Figure 1.26 are the mean values of the Gaussian fits of the pull distributions. The proximity of these mean values to zero affirms that the systematic corrections (energy loss corrections, momentum corrections and photon energy corrections) were properly determined and applied. A table containing the mean and sigma values of all of the fits seen in Figure 1.26 can be found in Table 1.1. Finally, Table 1.2 shows the number of events for each polarization setting and for each topology surviving our analysis cuts. For each energy setting, Topology 1 (with a missing π^-) provides the largest statistics.

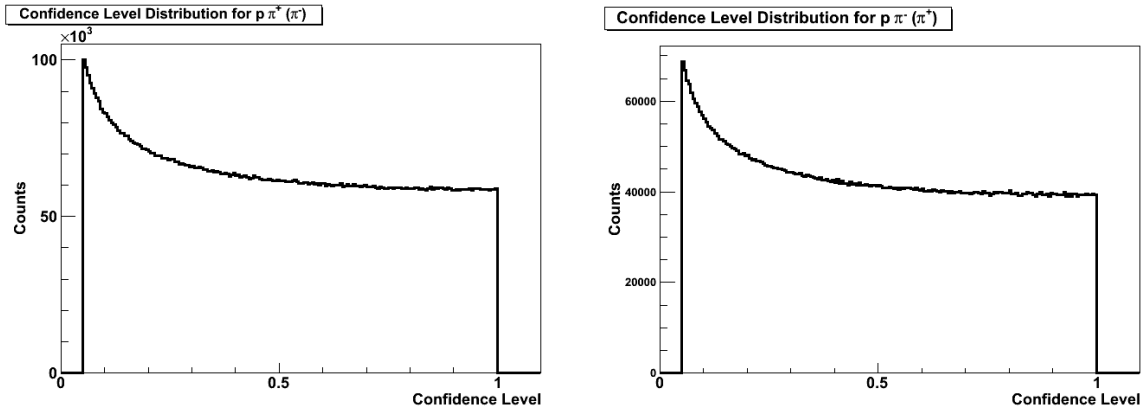

(a) $p\ \pi^+(\pi^-)$

(b) $p\ \pi^-(\pi^+)$

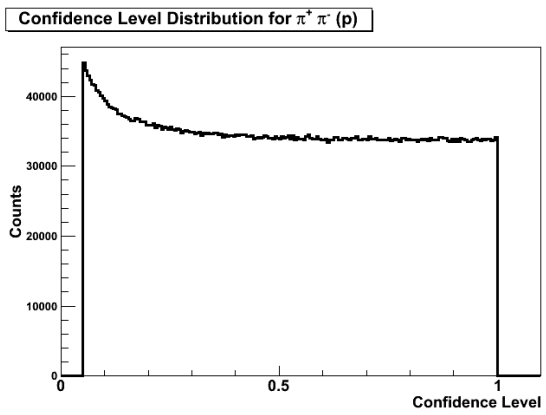

(c) $\pi^+\pi^-(p)$

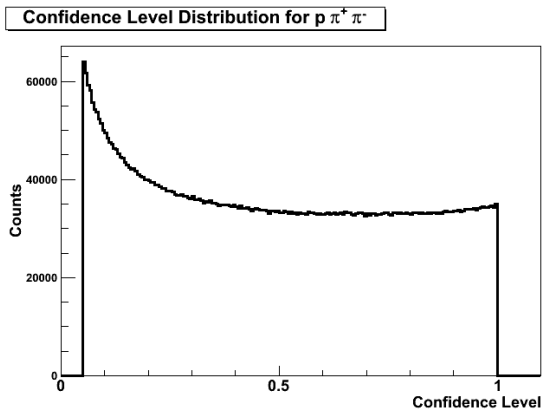

(d) $p\,\pi^+\pi^-$

Figure 1.24: A set of confidence level distributions for all final state topologies after the application of all corrections and cuts. Only Topology 4 shows a small increase toward large CL values. Generated using one run (#048326).

Table 1.1: The Gaussian mean (μ) and sigma (σ) values (left) for all fits to the pull distributions seen in Figure 1.26 for run #048326. The right columns give the same values for the full statistics.

Parameter	Mean (μ)	Sigma (σ)		Mean (μ)	Sigma (σ)
p_p	0.035	1.008		0.009	0.997
λ_p	−0.041	1.022		−0.041	0.974
ϕ_p	0.015	0.997		0.012	1.031
$\mathrm{p}_{\pi+}$	−0.045	0.982		−0.101	1.019
$\lambda_{\pi+}$	−0.049	1.021		−0.054	0.995
$\phi_{\pi+}$	−0.080	0.994		−0.110	1.019
$\mathrm{p}_{\pi-}$	−0.033	0.988		0.076	1.019
$\lambda_{\pi-}$	−0.019	1.024		−0.024	0.988
$\phi_{\pi-}$	−0.058	0.996		−0.070	1.037
E_γ	−0.003	1.017		0.023	1.062

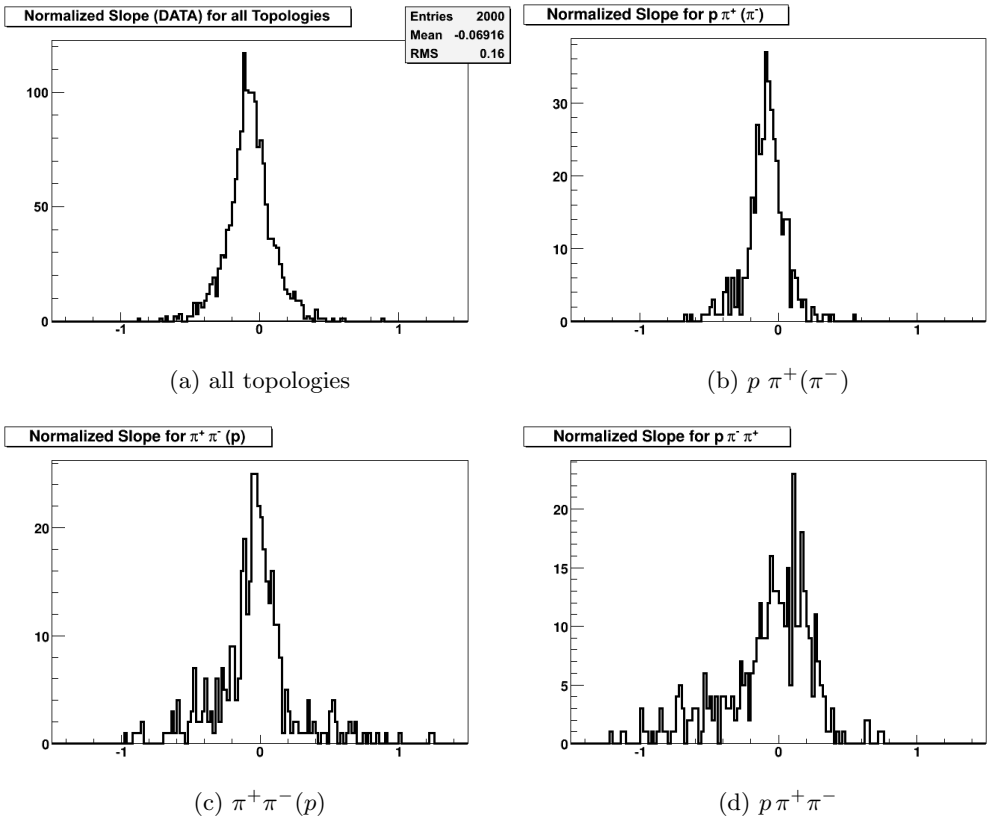

(a) all topologies

(b) $p\ \pi^+(\pi^-)$

(c) $\pi^+\pi^-(p)$

(d) $p\,\pi^+\pi^-$

Figure 1.25: The normalized slope distributions for individual final state topologies. Each confidence level distribution was fitted to a linear equation from $[0.55, 1.00]$ and the normalized slope determined using Equation (1.8). The behavior of the distributions (centered around zero) indicated the flatness of the confidence level histograms. Entries that stray away from zero can be attributed to kinematical regions containing low statistics.

Table 1.2: The total number of events for each polarization setting and for each reconstructed topology surviving all cuts. The initial total number of events for each polarization setting is also given. A particle in parenthesis indicates a missing particle.

Setting	Total #Events	$p\pi^+(\pi^-)$	$p(\pi^+)\pi^-$	$(p)\pi^+\pi^-$	$p\pi^+\pi^-$
1.3 GeV, PARA	153,957,674	1,714,914	1,299,563	1,255,387	1,084,469
1.3 GeV, PERP	125,592,563	1,685,168	1,220,384	1,117,943	1,020,754
1.5 GeV, PARA	136,715,419	1,601,785	1,103,198	860,476	939,695
1.5 GeV, PERP	113,987,764	1,272,650	844,791	628,846	724,132
1.7 GeV, PARA	96,448,403	848,857	519,309	352,144	434,214
1.7 GeV, PERP	145,330,810	1,195,841	705,107	458,224	594,687
1.9 GeV, PARA	38,902,106	447,928	237,636	138,244	186,113
1.9 GeV, PERP	50,730,044	674,156	348,865	199,226	284,220
2.1 GeV, PARA	83,546,322	575,615	283,030	143,550	200,952
2.1 GeV, PERP	85,409,333	617,480	296,336	147,616	221,544
AMORPHOUS	248,573,710	2,912,591	1,850,473	1,386,307	1,507,422

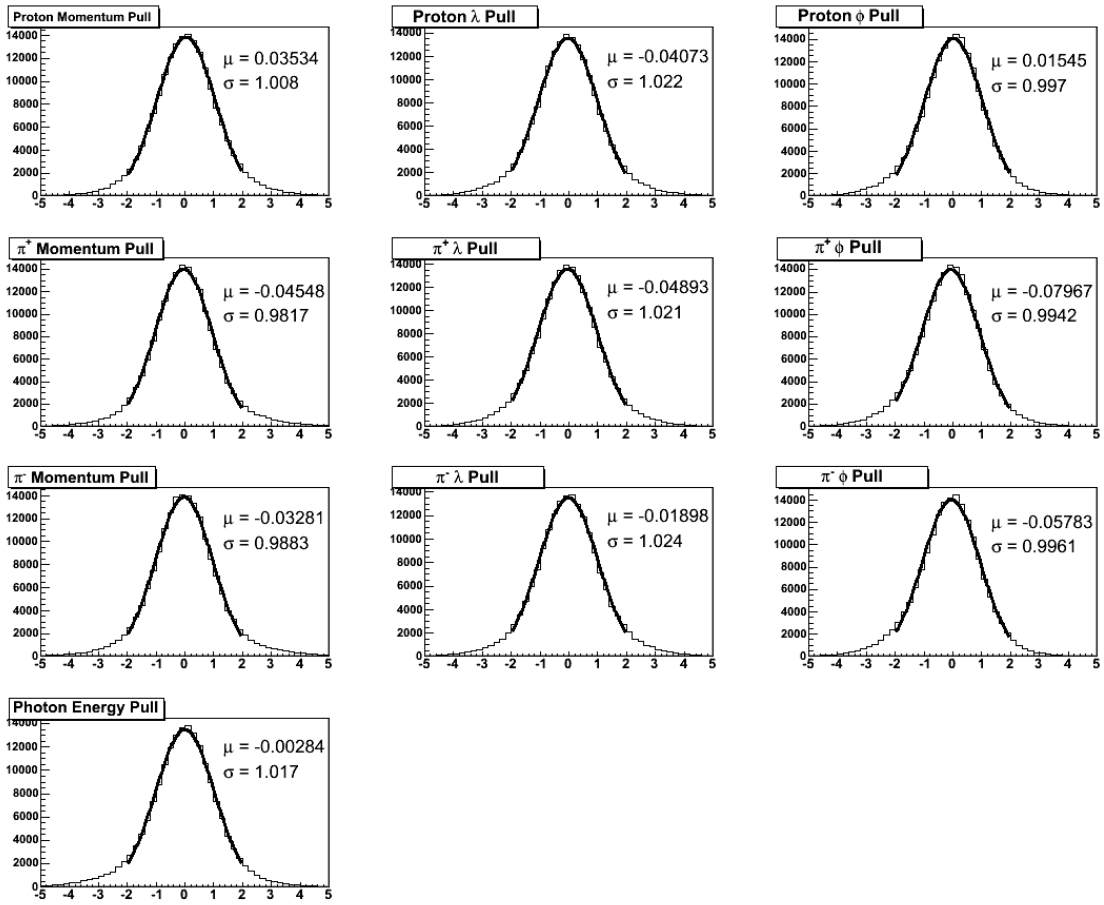

Figure 1.26: Pull distributions generated from a kinematic fit to a $p\pi^+\pi^-$ final state for events in run #048326. Distributions are fitted with a Gaussian from $[-2, 2]$.

CHAPTER 2

DATA ANALYSIS

Once the final state topologies of interest have been selected from the data, the corrections and cuts applied and kinematic fitting performed, the process of extracting the polarization observables I^s and I^c can begin. This chapter will focus on the methods used to extract these two polarization observables.

2.1 Binning and Angles

In order for any analysis to be carried out, the kinematics involved in the reaction of interest must be understood. The description of the kinematics involved in the reaction $\vec{\gamma}p \rightarrow p\,\pi^+\pi^-$ requires a choice of five independent kinematic variables. The kinematic variables chosen for this analysis are $\cos\theta^p_{c.m.}$, a mass ($m_{p\pi^+}$, $m_{p\pi^-}$, or $m_{\pi^+\pi^-}$), the incident photon energy, k, $\theta^*_{\pi^+}$, and $\phi^*_{\pi^+}$. A diagram showing the kinematics involved in the analysis of this $p\,\pi^+\pi^-$ final state can be seen in Figure 2.1. This diagram illustrates the kinematics in not only the center-of-mass frame (the blue plane in the figure) but also the decay frame in which the two final state pions occur back-to-back (the gold plane). The vectors describing the final state particles in the center-of-mass frame are shown by the vectors drawn with a solid line while the vectors with a dashed line represent the final state particles in the decay frame.

The angle ϕ^* is a kinematical variable unique to a final state containing two mesons. It describes the orientation of the decay plane containing the two pions (defined by the z'-axis and the $(\pi^+)'$ 4-vector) with respect to the production plane (defined by the incident photon and recoiling proton) and is measured with respect to one final state pion. Our choice is the π^+ meson. This angle, $\phi^*_{\pi^+}$, is calculated via two boosts, the first being a boost along the beamline (the z-axis) into the center-of-mass frame. The second boost occurs along the axis that is antiparallel to the recoiling proton and results in a boosting into the decay frame where the two final state pions occur back-to-back. Describing the angle between one of the final state pions and the axis defined as being anti-parallel to the recoiling proton in the center-of-mass frame (the z'-axis) is the angle θ^*_π. This angle is also calculated via boosting into the pion frame. For this analysis, the pion from which both angles are measured was chosen to be the π^+ meson. It is certainly also possible to look at the $p\pi^-$ or $p\pi^+$ system recoiling against the π^-. The coordinate system formed to calculate these angles is put together thus (see also Figure 2.1):

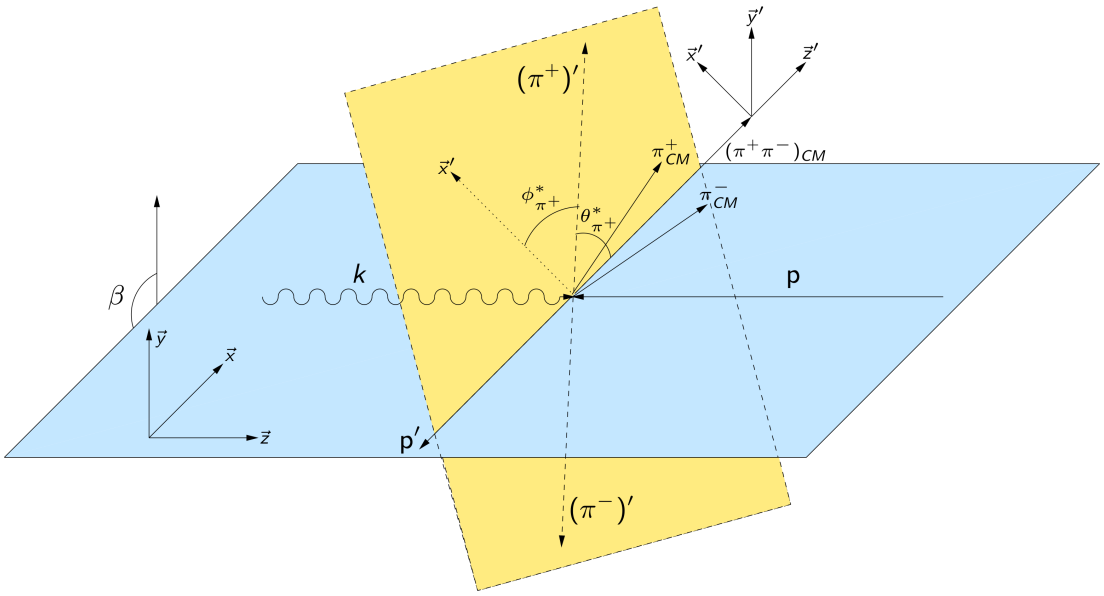

Figure 2.1: A diagram describing (one possible configuration of) the kinematics of the $\vec{\gamma}p \to p\,\pi^+\pi^-$ reaction. The blue plane represents the center-of-mass (c.m.) production plane while the gold plane represents the decay plane (where the two pions are produced back-to-back). Vector drawn with a solid line represent final state particles in the c.m. frame while the vectors drawn with a dashed line represent the final state particles in the decay frame. The pion 4-vectors in the c.m. frame ($\vec{\pi}^+_{c.m.} + \vec{\pi}^-_{c.m.}$) are used to form the $\vec{z}'$-axis. The $\vec{y}'$-axis is formed by determining the cross product of the target and recoil proton's 4-vector ($\vec{p} \times \vec{p}'$). The $\vec{x}'$-axis is then determined by forming the cross product of the $\vec{y}'$ and $\vec{z}'$-axes ($\vec{y}' \times \vec{z}'$). The angle $\phi^*_{\pi^+}$ is shown here and is the angle between the $(\pi^+)'$ (the 4-vector of π^+ after a boost into the decay frame) and the $\vec{x}'$-axis (which lies in the production plane). The angle $\theta^*_{\pi^+}$, also shown here, is the angle between the $(\pi^+)'$ and the $\vec{z}'$-axis.

1. The z'-axis is formed by adding the 4-vectors of the two final state mesons:

$$\vec{z}' = (\vec{\pi}^+_{c.m.} + \vec{\pi}^-_{c.m.}). \tag{2.1}$$

2. The y'-axis (pointing "up" perpendicular to the production plane) is formed by taking the cross product of the target proton and the recoiling proton in the center-of-mass frame:

$$\vec{y}' = (\vec{p} \times \vec{p}'). \tag{2.2}$$

3. Finally, the x'-axis is formed by taking the cross product of the y'- and the z'-axes:

$$\vec{x}' = (\vec{y}' \times \vec{z}'). \tag{2.3}$$

In this analysis, the data is then binned in three out of the five independent kinematical variables. For example, these binning variables can be: incident photon energy, k, $\theta^*_{\pi^+}$ and $\phi^*_{\pi^+}$. The decision to bin in the incident photon energy, E_γ, was a matter of convention while the decision to bin in the angles θ^* and ϕ^* came from the fact that they are unique to a three-body final state. We also analyzed the data using the incident photon energy,

k, $m_{p\pi^+}$, and $\phi^*_{\pi^+}$. A diagram of the reaction of interest and the angles used for binning can be seen in Figure 2.1. In terms of photon energy, k, each 200 MeV-wide window of highly polarized photons is divided into four bins each being 50 MeV wide. With there being 5 different coherent edge energies, this leads to a total of 20 bins in incident photon energy, covering a range from 1.1 GeV to 2.1 GeV. For the other binning variables ($\theta^*_{\pi^+}$, $\phi^*_{\pi^+}$, and $m_{p\pi^+}$), 20 bins are used: (1) $\cos\theta^*_{\pi^+}$ (covering a range from $-1 \leq \cos\theta^*_{\pi^+} \leq 1$) , (2) $\phi^*_{\pi^+}$ (covering a range from $-\pi \leq \phi^*_{\pi^+} \leq \pi$), and (3) $m_{p\pi^+}$ (covering a range from 1 to 2 GeV/c^2). This choice of binning (and using three variables) therefore results in a total of 8000 bin combinations per final state topology.

For $\gamma p \to p\,\pi\pi$ without measuring the polarization of the recoiling nucleon, the reaction rate I can be written as [4]:

$$\begin{aligned} I \;=\; I_0 \{\, (1 \,+\, \vec{\Lambda}_i \cdot \vec{\mathbf{P}} \,) \\ &+\, \delta_\odot \,(\mathbf{I}^\odot \,+\, \vec{\Lambda}_i \cdot \vec{\mathbf{P}}^{\,\odot}\,) \\ &+\, \delta_l \,[\sin 2\beta \,(\,\mathbf{I}^{\mathbf{s}} \,+\, \vec{\Lambda}_i \cdot \vec{\mathbf{P}}^{\,\mathbf{s}}\,) \\ &\qquad \cos 2\beta \,(\,\mathbf{I}^{\mathbf{c}} \,+\, \vec{\Lambda}_i \cdot \vec{\mathbf{P}}^{\,\mathbf{c}}\,)\,]\,\} \;, \end{aligned} \tag{2.4}$$

where I_0 is the unpolarized reaction rate and $\vec{\mathbf{I}}^{\odot}$ is the only two-pion observable, which has been published previously [39]. It describes the asymmetry for an unpolarized target and a circularly-polarized photon beam. The observables $\vec{\mathbf{P}}$ represents the polarization asymmetry that arises if only the target nucleon is polarized, and $\vec{\mathbf{P}}^{\,\odot}$ as well as $\vec{\mathbf{P}}^{\,\mathrm{s,c}}$ represent the polarization observables if, in addition to the target nucleon, also the incoming photon is polarized, either circularly or linearly, respectivley. Here, $\vec{\Lambda}_i$ denotes the polarization of the initial nucleon, $\delta_\odot$ is the degree of circular polarization in the photon beam, while δ_l is the degree of linear polarization. In the experiment, the orientation of the linear photon polarization is given in the laboratory frame by an angle α and, thus, $\beta = \alpha - \phi_{\mathrm{lab}}$. For our measurements, the diamond crystal was oriented such that the direction of the beam polarization was either perpendicular to the floor of the experimental area with $\alpha = \pi/2$ (PERP data) or parallel to the floor with $\alpha = 0$ (PARA data). For the g8b data, this equation reduces to:

$$I \;=\; I_0 \,(\, 1 + \delta_l \,[\sin 2\beta \;\mathbf{I}^{\mathbf{s}} \,+\, \cos 2\beta \;\mathbf{I}^{\mathbf{c}}\,]\,)\,, \tag{2.5}$$

and results in the two beam asymmetries, $\vec{\mathbf{I}}^{\mathrm{s}}$ and $\vec{\mathbf{I}}^{\mathrm{c}}$, which have been determined in this analysis for the first time.

The definition of β is not unique. In [4], it is defined as the angle between the direction of the photon polarization and the x-axis. The x-axis is related to the three-momentum direction of the pair of pions. In other words, the angle, β, is simply the angle between the polarization plane and the reaction plane. The latter is defined according to [4] as the plane spanned by the beam axis and the recoiling two-pion pair (or equivalently the recoiling proton). In single-meson production, the reaction plane is usually defined as the plane spanned by the beam axis and the recoiling proton. In double-meson production, there are more possibilities to define the reaction plane. In our analysis, we have chosen the beam axis and the recoiling π^+ meson. For this reason, $\beta = \phi_{\mathrm{lab}}$ of the π^+ meson in all following equations. The choice of the particle depends somewhat on the focus of the analysis. Equation 2.4 is of course still valid, the observables just depend on the chosen

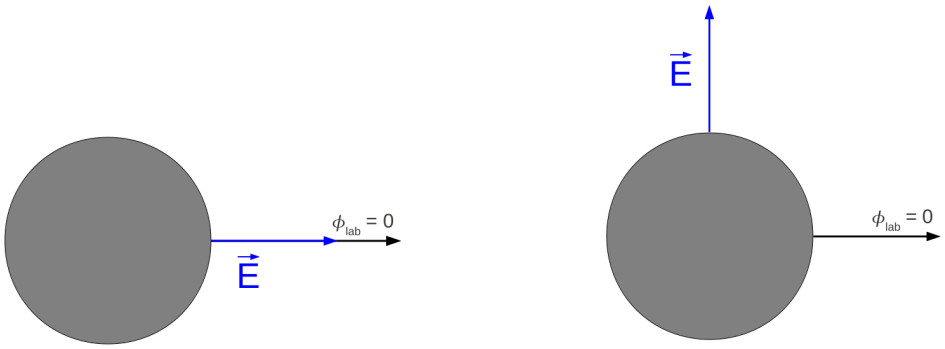

(a) PARA (b) PERP

Figure 2.2: A cartoon describing the two linear polarization settings of the photon. For the PARA setting (a), the $\vec{E}$ field oscillates in a plane parallel to the floor ($\phi_{\text{lab}} = 0$) of the experimental hall while for the PERP setting (b), the oscillation of the $\vec{E}$ field is perpendicular to the floor of the experimental hall.

variables. This is also true for the choice of the five independent kinematic variables needed to describe the five-dimensional phasespace.

2.2 Study of ϕ_{lab} Distributions

When using unpolarized photons, the production of the final state particles is independent of the azimuthal lab angle, ϕ_{lab}. This analysis, however, involves the use of linearly polarized photons which breaks this symmetry. Therefore a plot of the distribution of events over the full range of the lab angle ϕ_{lab} (with respect to a particular final state particle) can be made, revealing this asymmetry.

The two orthogonal linear polarization settings used during g8b, termed PARA and PERP, denote the relationship between the $\vec{E}$ field of the polarized photon and the axis where $\phi_{\text{lab}} = 0$. Therefore a PARA setting indicates that the photon was polarized such that its $\vec{E}$ field (electric field) oscillates in a plane parallel to $\phi_{\text{lab}} = 0$ (the floor of the experimental hall) and the PERP setting indicates that the oscillation of the photon's $\vec{E}$ field is perpendicular to $\phi_{\text{lab}} = 0$. The cartoon seen in Figure 2.2 demonstrates these two settings. To produce unpolarized photons, an amorphous radiator was used in place of the diamond radiator. This setting is termed the amorphous (AMO) setting.

During the course of this analysis there were two methods developed to extract the polarization observables. The common trait between these two methods is that they both begin with the production of histograms containing the ϕ_{lab} distributions (hereby referred to as *ϕ-distributions*)[1] containing the ϕ_{lab} value of a final state particle (in this case, the π^+ meson) for all events which pass the imposed cuts. Exploiting the fact that the use of polarized photons breaks the ϕ_{lab} symmetry, events are plotted as a function of the lab angle ϕ_{π^+} for each polarization setting (Figure 2.3).

[1]Note that ϕ_{lab} is different from the angle ϕ^* describing the azimuthal angle of the π^+ in the rest frame of the two pions.

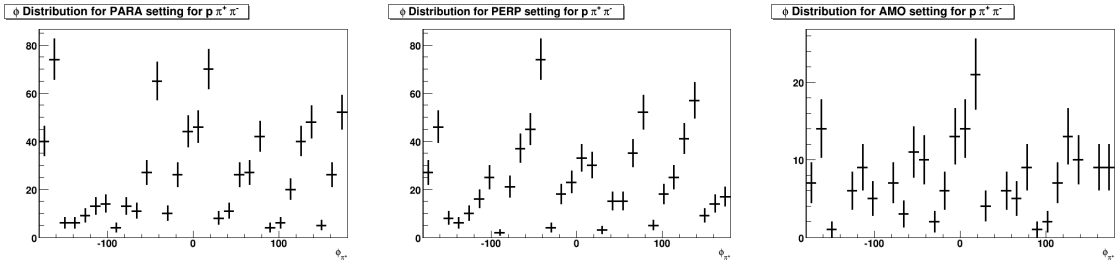

(a) PARA ϕ-distribution (b) PERP ϕ-distribution (c) AMO ϕ-distribution

Figure 2.3: Examples of ϕ_{lab}-distributions for each polarization setting for a $p\,\pi^+\pi^-$ final state using data from the 1.3 GeV coherent edge setting. All three histograms belong to the same bin combination ($1.25\text{ GeV} < E_\gamma < 1.3\text{ GeV}$, $-1 < \cos\theta^*_{\pi^+} < -0.9$, $180^\circ < \phi^*_{\pi^+} < 198^\circ$). Acceptance effects (such as the support structures of the Drift Chambers) can be seen in all figures and demonstrate the need for a method which removes these acceptance effects. Furthermore, as the error bars for the measurements are an indication of available statistics, the low-statistics problem for the AMO setting is clearly evident. This low amount of statistics for the AMO setting leads to observable measurements which also possess large error bars.

Systematic effects which drown out the ϕ asymmetry can easily be seen in these distributions. An example of such an effect are the support structures of the drift chambers which, as one might expect, affect the distributions as no particle will be detected where the support structure is. The effects of these support structures can be seen at $\phi_{\pi^+} = -150^\circ$, -90°, -30°, 30°, 90° and 150° in all three histograms. For this reason, two methods are carried out which remove these systematic effects, leading to a measurement of the polarization observables.

2.2.1 Method 1: Using unpolarized (AMO) data

The first method for extracting the polarization observables involves using the unpolarized (AMO) data. Even though corrections and cuts have been imposed on the events that are plotted in the ϕ-distributions, systematics such as the support structure of the the Drift Chambers are still present in the distributions. In order to remove these effects, the ϕ-distributions for each of the linear polarization settings is divided by the AMO ϕ-distribution (for matching kinematical bin combinations) (Figure 2.4). The resulting distributions are then fitted to the double-meson final state equation with the g8b run conditions applied [4]:

$$I = I_0 \,\{\, 1 \;+\; \delta_l \,[\mathbf{I^s}\,\sin(2\beta) \;+\; \mathbf{I^c}\,\cos(2\beta)\,]\,\}\,, \tag{2.6}$$

which when written as a fit equation, becomes:

$$f(\beta) = A \;+\; B\sin(2\beta) \;+\; \mathrm{C}\cos(2\beta)\,, \tag{2.7}$$

where $A = F_{\parallel,\perp}/F_{\text{amo}}$ is the flux ratio of polarized to unpolarized data and $B = A\,\delta_{\parallel,\perp}\,I^s$ and $C = A\,\delta_{\parallel,\perp}\,I^c$. Moreover, $\delta_{\parallel,\perp}$ is the degree of linear beam polarization.

The polarization observables I^s and I^c can then be readily extracted from the fitted ϕ-distributions. The downside of producing observable measurements in this way is that

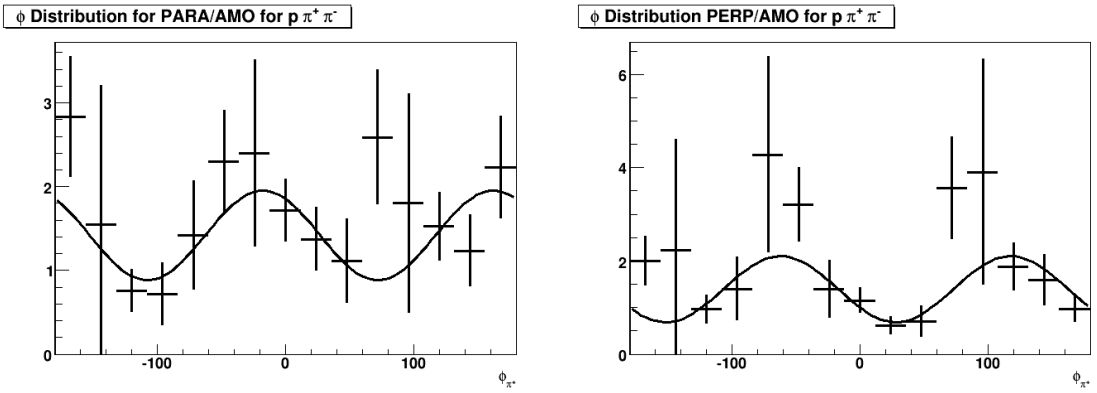

(a) PARA/AMO (b) PERP/AMO

Figure 2.4: ϕ-distributions generated by dividing the PARA and PERP ϕ-distributions by the AMO ϕ-distribution (using the histograms seen in Figure 2.3). The solid line on both (a) and (b) represents the fitting of the distributions with Equation (2.7). Once this fit is performed, the observables I^s and I^c can be extracted. The large error bars and low number of data points seen in both histograms demonstrate the limitation of extracting the polarization observables in this manner. This limitation arises from the low amount of statistics contained in the amorphous (AMO) data.

the statistics of the ϕ-distribution to be fit is limited by the number of events in the AMO distribution. This AMO setting possesses the lowest amount of statistics in the g8b data set. This reduction of events in the PARA/AMO or PERP/AMO distributions directly affects the fits and the fit qualities therefore affecting the final polarization observable measurements. This difference in statistics can be seen in Figure 2.3. Both the PARA and PERP ϕ distributions contain roughly five times the statistics of the AMO ϕ-distribution for the same bin combination. In order to produce observable measurements with minimal statistical errors, another method is needed which does not depend on the statistics of the AMO polarization setting.

2.2.2 Method 2: Asymmetry using the two linear polarization settings, PARA and PERP, directly

The second method for extracting polarization observables from the data is independent of the (statistics-poor) AMO data and therefore leads to observable measurements with much smaller statistical errors. This method possesses the characteristic that it uses the asymmetry between the PARA and PERP polarization settings. Just like the previously discussed method, the starting point is the generation of ϕ-distributions for both the PARA and PERP settings. The asymmetry between these ϕ-distributions is then formed. Finally, this asymmetry is fit to the asymmetry equation involving PARA and PERP (substituting in the final state equation for two mesons for each setting):

$$A(E_\gamma, \theta^*_{\pi^+}, \phi^*_{\pi^+}, \theta^p_{c.m.}, m_{p\pi^+}) \;=\; \frac{I^{PARA} \;-\; I^{PERP}}{I^{PARA} \;+\; I^{PERP}}\,, \tag{2.8}$$

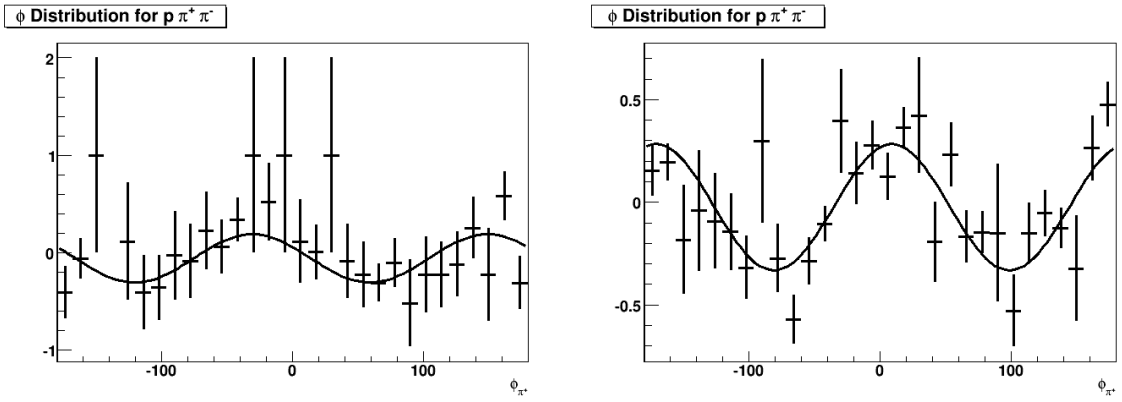

Figure 2.5: Examples of ϕ-distributions generated using the asymmetry between PARA and PERP which have been fitted with the final state equation (Equation (2.11)). The distribution seen in (a) corresponds to 1.1 GeV $< E_\gamma <$ 1.15 GeV, $-0.9 < \cos\theta^*_{\pi^+} < -0.8$, $108^\circ < \phi^*_{\pi^+} < 126^\circ$ and the distribution seen in (b) corresponds to 1.25 GeV $< E_\gamma <$ 1.3 GeV, $-1 < \cos\theta^*_{\pi^+} < -0.9$, $180^\circ < \phi^*_{\pi^+} < 198^\circ$). Both distributions were generated for a $p\,\pi^+\pi^-$ final state. By using the asymmetry between the PARA and the PERP settings to generate the ϕ-distributions, the number of data points is greater and the error bars for these points smaller leading to a much better fit.

with m standing for the invariant $p\pi^+$ mass and I having the form seen in Equation (2.6) with I^{PARA} and I^{PERP} being defined as:

$$I^{PARA} \;=\; I_0 \,\{\, 1 \;+\; \delta_l \,[\mathbf{I^s}\,\sin(2\beta) \;+\; \mathbf{I^c}\,\cos(2\beta)\,]\,\} \tag{2.9}$$

and

$$I^{PERP} \;=\; I_0 \,\{\, 1 \;-\; \delta_l \,[\mathbf{I^s}\,\sin(2\beta) \;+\; \mathbf{I^c}\,\cos(2\beta)\,]\,\}\,, \tag{2.10}$$

where δ_l represents the degree of linear polarization. The orthogonality of the two polarization settings, PARA and PERP, gives rise to the minus sign seen in Equation (2.10). Again, the angle β denotes the azimuthal angle being a combination of $\phi_{\,\mathrm{lab}}$ and the orientation of linear polarization ($\beta = \alpha - \phi_{\,\mathrm{lab}}$) where α equals 0° or 90° (0 or $\frac{\pi}{2}$ radians) for PARA and PERP, respectively. For this approach, the corresponding histograms for PARA and PERP need to be properly normalized. Placing equations (2.9) and (2.10) in equation (2.8) then gives (after simplification):

$$A(E_\gamma, \theta^*_{\pi^+}, \phi^*_{\pi^+}) \;=\; y_0 + B(E_\gamma, \theta^*_{\pi^+}, \phi^*_{\pi^+}) \tag{2.11}$$

where y_0 is the vertical offset of the distribution and

$$B(E_\gamma, \theta^*_{\pi^+}, \phi^*_{\pi^+}) \;=\; \frac{(\delta_l^{\parallel} \;+\; \delta_l^{\perp})\;\mathbf{I^s}\,\sin(2\beta) \;+\; (\delta_l^{\parallel} \;+\; \delta_l^{\perp})\;\mathbf{I^c}\,\cos(2\beta)}{2 \;+\; (\delta_l^{\parallel} \;-\; \delta_l^{\perp})\;\mathbf{I^s}\,\sin(2\beta) \;+\; (\delta_l^{\parallel} \;-\; \delta_l^{\perp})\;\mathbf{I^c}\,\cos(2\beta)} \tag{2.12}$$

(here $\parallel$ represents the PARA setting and $\perp$ represents the PERP setting). Normalization issues can be observed in systematic shifts of the vertical offsets, y_0, from zero.

The resulting ϕ-distribution can then be fit to this asymmetry equation (2.11). Provided as an example, the fits of two ϕ-distributions to this equation for a $p\,\pi^+\pi^-$ final state can

be seen in Figure 2.5. Once the fit is performed, the polarization observables (being simply the constants in front of the cosine and sine terms) can be extracted.

Normalizing PARA and PERP Distributions in Method 2 (obsolete). We have normalized, for each kinematic bin, our PARA $\phi_{\rm lab}$ distributions to the corresponding PERP $\phi_{\rm lab}$ distributions. Under the assumption that PARA and PERP data are subject to the same detector acceptance, simply the number of entries in each histogram could be used. To avoid such (probably minor acceptance issues), we extracted the normalization (or scaling factors) from corresponding PARA/AMO and PERP/AMO distributions. We have not observed significant differences in our results for either approach.

For the final results, we decided to introduce the PARA and PERP fluxes as fit parameters in our fit function. This will be discussed in the following section.

Extraction of the photon beam asymmetry without needing to explicitly know the fluxes of the datasets. The following derivation has been taken partially from the CLAS Note 2012-010 [58] and expanded to cover the production of two pseudoscalar mesons. Ideally, the photon flux, F, is known, from some independent monitor. However, it is often not known accurately enough. We can show that this can be extracted from the fitted data. The procedure works amazingly well. In the more general situation, $\delta_l^{\parallel} \neq \delta_l^{\perp}$, the flux is also not known well enough to scale the datasets such that $F_{\parallel} = F_{\perp}$. This leads to the following expressions, similar to Equations 2.9 and 2.10:

$$I^{PARA} \;=\; I_0 \,\{\; 1 \;+\; F_{\parallel}\,\delta_l \,[\mathbf{I^s}\,\sin(2\beta) \;+\; \mathbf{I^c}\,\cos(2\beta)\;]\;\} \tag{2.13}$$

and

$$I^{PERP} \;=\; I_0 \,\{\; 1 \;-\; F_{\perp}\,\delta_l \,[\mathbf{I^s}\,\sin(2\beta) \;+\; \mathbf{I^c}\,\cos(2\beta)\;]\;\}\,. \tag{2.14}$$

Placing equations 2.13 and 2.14 in equation 2.8 then gives (in analogy to equation 2.12):

$$B \;=\; \frac{F_R - 1 + \frac{F_R\,\delta_R+1}{\delta_R+1}\;2\,\delta_S\;\mathbf{I^s}\,\sin(2\beta) \;+\; \frac{F_R\,\delta_R+1}{\delta_R+1}\;2\,\delta_S\;\mathbf{I^c}\,\cos(2\beta)}{2\,F_R \;+\; 2 \;+\; \frac{F_R\,\delta_R-1}{\delta_R+1}\;2\,\delta_S\;\mathbf{I^s}\,\sin(2\beta) \;+\; \frac{F_R\,\delta_R-1}{\delta_R+1}\;2\,\delta_S\;\mathbf{I^c}\,\cos(2\beta)}\,, \tag{2.15}$$

where $F_R \;=\; F_{\parallel}\,/\,F_{\perp}$ and $\delta_R \;=\; \delta_l^{\parallel}\,/\,\delta_l^{\perp}$ as well as $\delta_S \;=\; \delta_l^{\parallel} \;+\; \delta_l^{\perp}$. With $F_R \;=\; 1$, this equation reduces to Equation 2.12. Equation 2.15 is our final fit function. We have used measured values for $\delta^{\parallel}$ and $\delta^{\perp}$, but have introduced the ratio of the fluxes as a fit parameter.

We have determined one normalization factor for each energy bin and subsequently used this one factor for all kinematic bins belonging to this energy bin. This approach is better justified than the extraction of the normalization (or scaling factors) from corresponding PARA/AMO and PERP/AMO distributions, but does not give visibly different results for the observables. There are small changes in the numerical values, though. Figure 2.6 shows examples of the extracted flux ratios for the four different topologies for $E_\gamma \in\; [\,1150,\,1200\,]$ MeV after using the fitted normalization factors. Only one factor was used for all fits in this energy bin. The ratios are all fairly centered at one and Gaussian in shape.

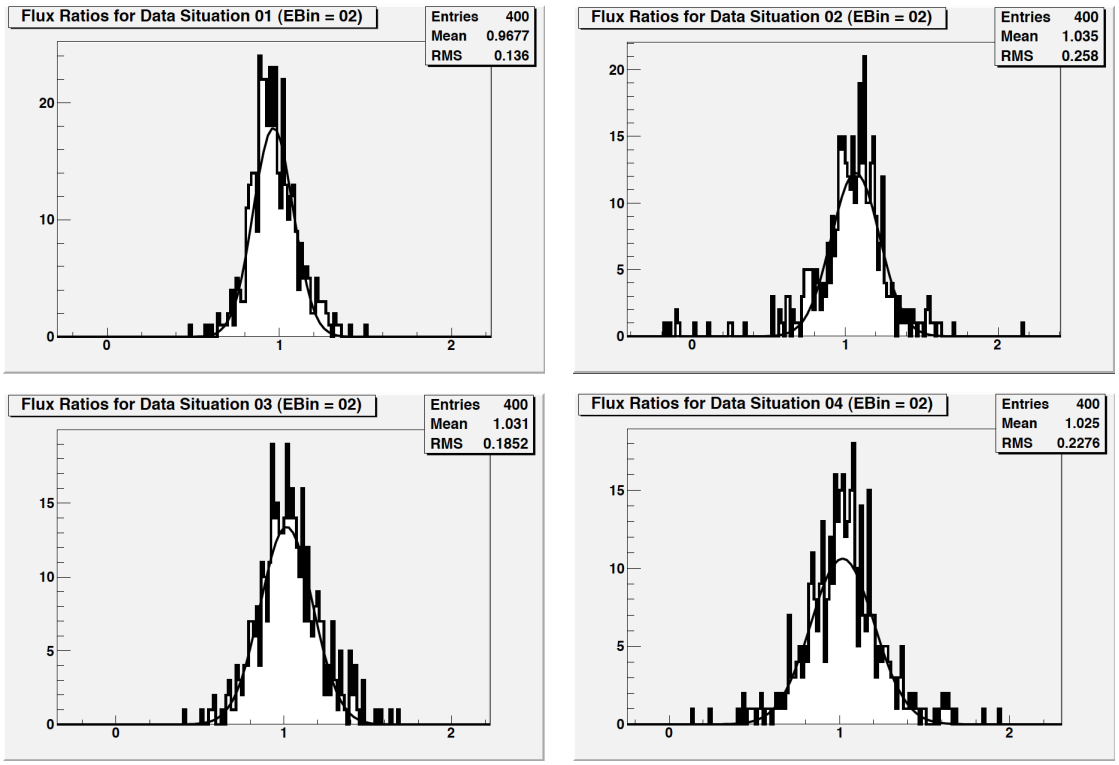

Figure 2.6: Fitted flux ratios for the four different topologies for $E_\gamma \in [1150, 1200]$ MeV after using the normalization factors extracted from the data. Only one factor was used for all fits in this energy bin.

Comparing PARA and PERP Distributions in Kolmogorov Tests

We have further tested the compatibility between corresponding PARA and PERP distributions before extracting the physics observables. In each kinematic bin, we compared PARA/AMO and PERP/AMO histograms by applying a Kolmogorov test, which provides a statistical test of compatibility in shape between two histograms [59]. For this test, the experimental PERP distributions were shifted by 90° to match the PARA distributions. Figure 2.7 shows typical p-value distributions for the topologies $\gamma p \to p\,\pi^+\pi^-_{\rm miss}$ (left) and $\gamma p \to p\,\pi^+\pi^-$ (right) integrated over all kinematic bins. Two histograms are usually considered similar if $p > 0.05$. We applied a cut of $p > 0.1$ and excluded such kinematic bins from the analysis.

2.3 χ^2 Values of Fits to $\phi_{\rm lab}$-Distributions

The high amount of statistics available in the g8b data set results in the ability to bin in three or more of the independent kinematical variables (although the statistics contained in each bin combination decreases as the number of binning variables used increases). The cost of this however (whether binning in all or three of the kinematic variables), is the large number of possible bin combinations and therefore a large number of $\phi_{\rm lab}$-distributions to be fit.

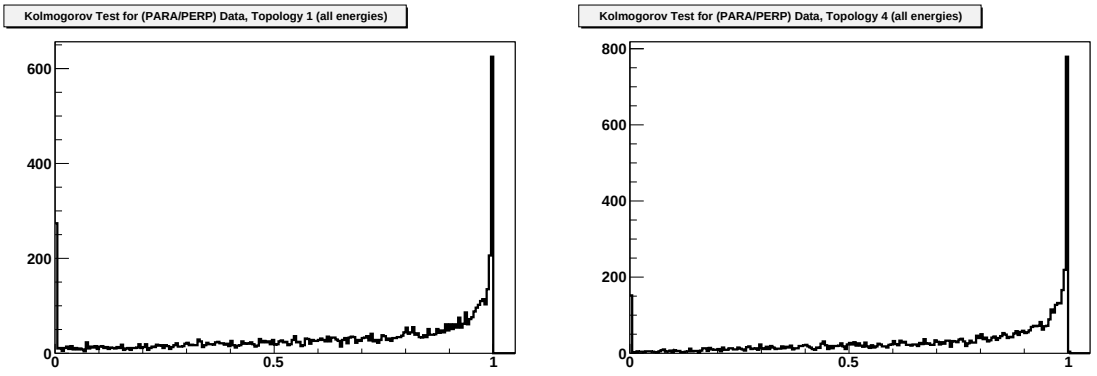

Figure 2.7: Comparing histograms of PARA and PERP distributions in a Kolmogorov Test. The distributions show typical p-value distributions for $\gamma p \to p\pi^+\pi^-_{\rm miss}$ (left) and $\gamma p \to p\pi^+\pi^-$ (right) integrated over all kinematic bins.

For example, binning in only three of the five kinematic variables for each final state topology leads to $32000 = 4 \cdot 20 \cdot 20 \cdot 20$ individual fits of the generated $\phi_{\rm lab}$-distributions. When considering the methods used to produce the fitted histograms (PARA/AMO, PERP/AMO, and the asymmetry between PARA and PERP), this total increases to $96000 = 3 \cdot 32\,000$. This makes it such that there are too many individual fits to be checked by eye. Due to this large number of individual fits, the most efficient method for judging the quality of the fits is to examine the distribution of the (reduced) χ^2 values for the fits. Such distributions can be seen in Figure 2.8 for all topologes and for all bin combinations. The distribution seen in Figure 2.8 all peak very close to one, indicating quality fitting of the $\phi_{\rm lab}$-distributions generated from the data. Less than 1 % of the bins have a reduced χ^2 value greater than three, about 0.2 % have a reduced χ^2 value greater than four.

2.4 Comparing Results from Different Topologies

In spite of the low statistics, we have compared results from our analysis using only PARA data with those from our analysis using only PERP data (Method 1) to check the consistency of the PARA and PERP datasets. Figure 2.9 shows the difference distributions ($I^s_{\rm PARA} - I^s_{\rm PERP}$) for all four topologies integrated over all kinematic bins. We list our (topology) naming scheme here as a reminder (see also Chapter 1):

Topology 1: $\vec{\gamma}\, p \to p\, \pi^+(\pi^-)$ (π^- not detected)

Topology 2: $\vec{\gamma}\, p \to p\, \pi^-(\pi^+)$ (π^+ not detected)

Topology 3: $\vec{\gamma}\, p \to \pi^+\pi^-(p)$ (proton not detected)

Topology 4: $\vec{\gamma}\, p \to p\,\pi^+\pi^-$ (all particles detected).

The distributions are Gaussian in shape and all centered at zero. This indicates the good consistency between the PARA and PERP datasets.

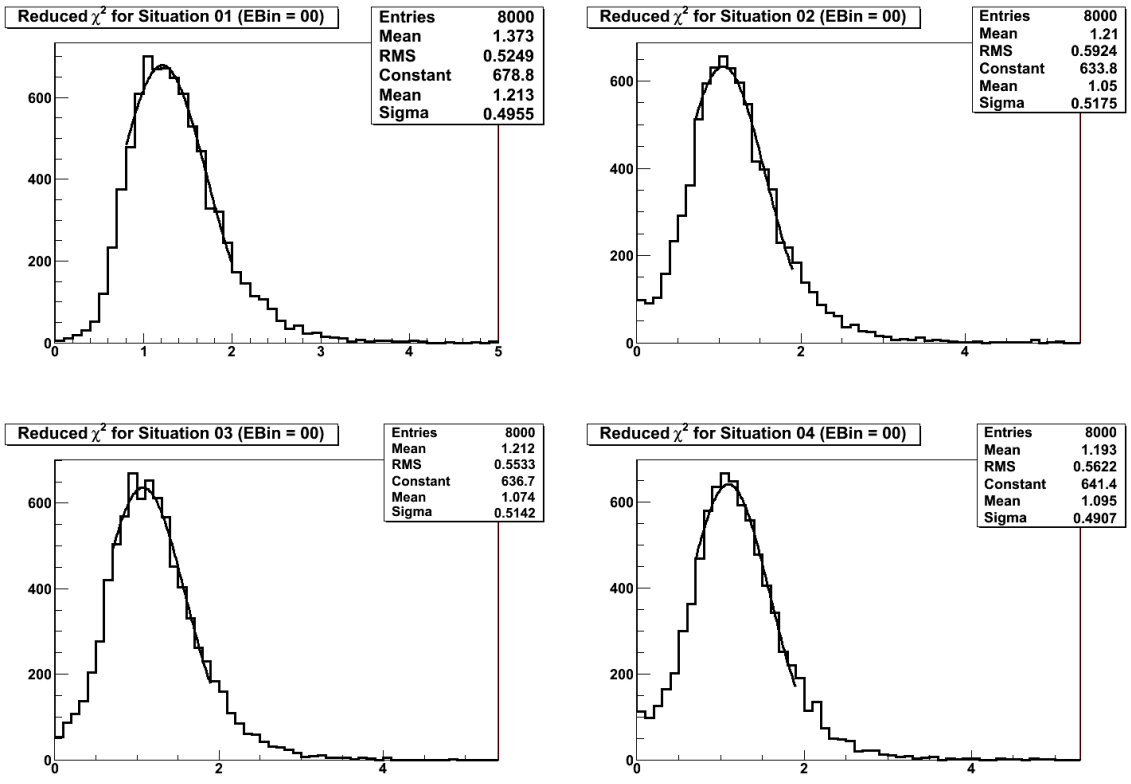

Figure 2.8: Reduced χ^2 values for the four different topologies integrated over all energies. All distributions peak very close to one indicating that the fit quality is good.

In a second step, we compared the results for different topologies using Method 2. Figure 2.11 shows the differences $(I^s_{\text{Topology X}} - I^s_{\text{Topology Y}})$ for all combinations of the four topologies integrated over all kinematic bins. The distributions are all Gaussian in shape and centered at zero hinting at the good consistency between the results from different topologies. It also indicates that the results from different topologies are equal in shape. Figure 2.12 shows similar results for the second observable, I^c. Again, plotted are the difference distributions:

$$(I^c_{\text{Topology X}} - I^c_{\text{Topology Y}}), \quad \text{X, Y} = 1, 2, 3, 4,$$

for all combinations among the four topologies integrated over all kinematic bins. The I^c distributions appear somewhat broader and show significant deviations from zero when Topology 3 is involved. This is the reason, why we decided not to use this topology in the analysis.

To improve statistics and to obtain a better kinematic coverage, the results for Topologies 1, 2 and 4 have been averaged (based on the good agreement seen in Fig. 2.11 and Fig. 2.12). It is important to keep in mind though that the two-pion final state requires five independent kinematic variables. At this point, we have only binned in three of them. For

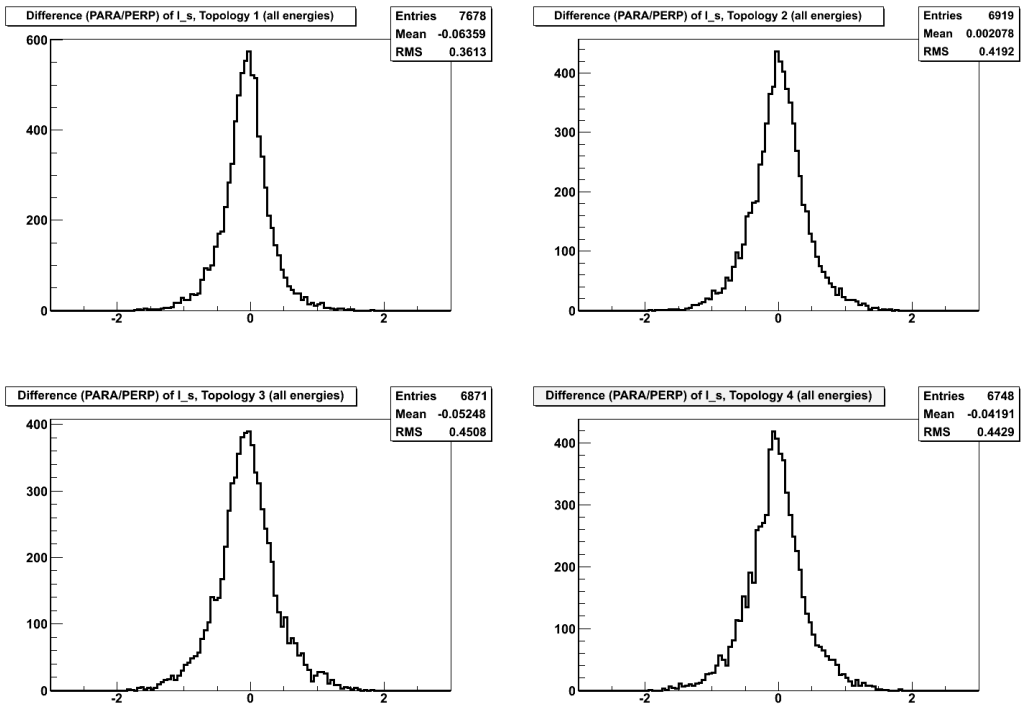

Figure 2.9: Comparisons (differences) between independent results for I^s from PARA/AMO and PERP/AMO integrated over all energies. The distributions are all Gaussian in shape and centered at zero showing the good consistency between PARA and PERP data.

this reason, there may direct acceptance effects associated with the variables used in the analysis (these effects however mostly cancel out) and indirect effects due to the integration over the remaining variables not used. We have formed the average in two different ways to obtain a feeling for the (remaining) acceptance effects. The two approaches are called Topologies 0 and 5:

1. **Topology 0** Used for the final results of our analysis: Final physics results for the observables I^s and I^c have been averaged.

2. **Topology 5** $\phi_{\rm lab}$-distributions for the different topologies have been averaged before the fits to extract the observables. We have done this only to study acceptance effects; this topology has not been used for our final results.

A comparison between Topologies 0 and 5 should reveal how big the impact of possible topology-dependent acceptance effects is since the detector acceptance drops out for Topology 0, but does not for Topology 5. The following example for the case of only two topologies, Topology X and Topology Y, illustrates this. The left side represents Topology 0 and the right side represents Topology 5:

$$\frac{(PARA-PERP)^X}{(PARA+PERP)^X}+\frac{(PARA-PERP)^Y}{(PARA+PERP)^Y} \neq \frac{(PARA-PERP)^X+(PARA-PERP)^Y}{(PARA+PERP)^X+(PARA+PERP)^Y}\,.$$

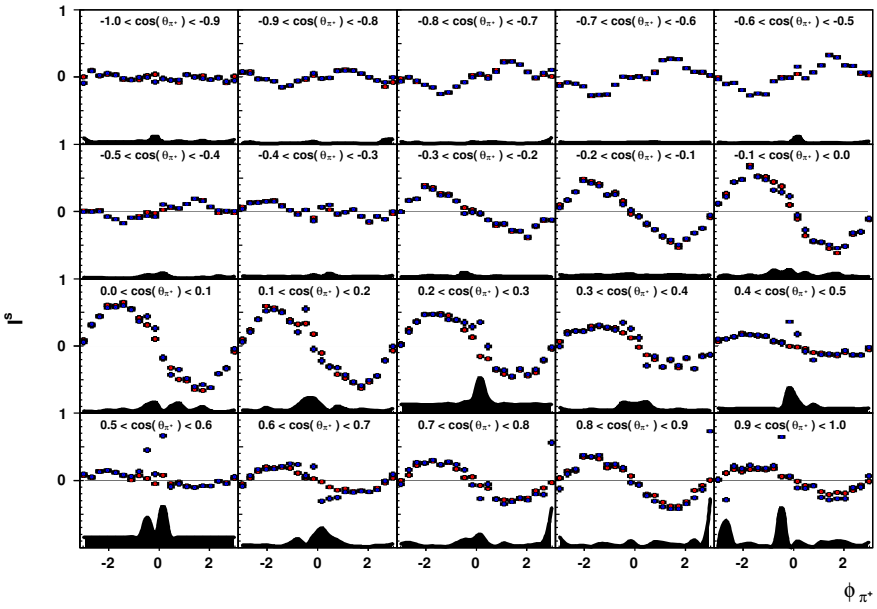

Figure 2.10: Comparison between Topology 0 (red points), where final results are averaged and acceptance effects mostly drop out, and Topology 5 (blue points), where the original ϕ_{lab} distributions have been averaged before the extraction of the observables. Shown is the Observable I^s for $1100 < E_\gamma < 1150$ MeV. The difference between the topologies is shown as systematic error band at the bottom of each distribution.

Fig. 2.10 shows the observable I^s for $1100 < E_\gamma < 1150$ MeV. The red points denote Topology 0 and the blue points denote Topology 5. The difference between the two topologies is given as an error band at the bottom of each distribution and for this reason, also includes statistical errors. In addition to the binning in incoming photon energy, the observable I^s is plotted in bins of $\cos\theta^*_{\pi^+}$ and versus $\phi^*_{\pi^+}$; the angles represent the azimuthal and polar angle of the π^+ in the rest frame of the two pions. Overall, the effects are fairly small and mostly statistical in nature.

2.5 Accounting for Detector Acceptance

In this work, the analysis techniques used to produce observable measurements mostly account for the kinematically-dependent acceptance rendering a Monte Carlo simulation of the data unnecessary. First of all, both methods used to extract I^s and I^c use only ϕ_{lab}-distributions with matching bin combinations to produce the observable measurements for each final state topology. Additionally, each kinematic variable that is used for binning the data (E_γ, $\theta^*_{\pi^+}$, $\phi^*_{\pi^+}$) is divided into 20 bins. This leads to bin widths that are small enough for the kinematic acceptance to not vary much within a particular bin combination. Therefore the combination of (sufficiently) small bins and the two methods used to extract the observables lead to this kinematically-dependent acceptance being accounted for (divided out) by comparing the same regions of phase space.

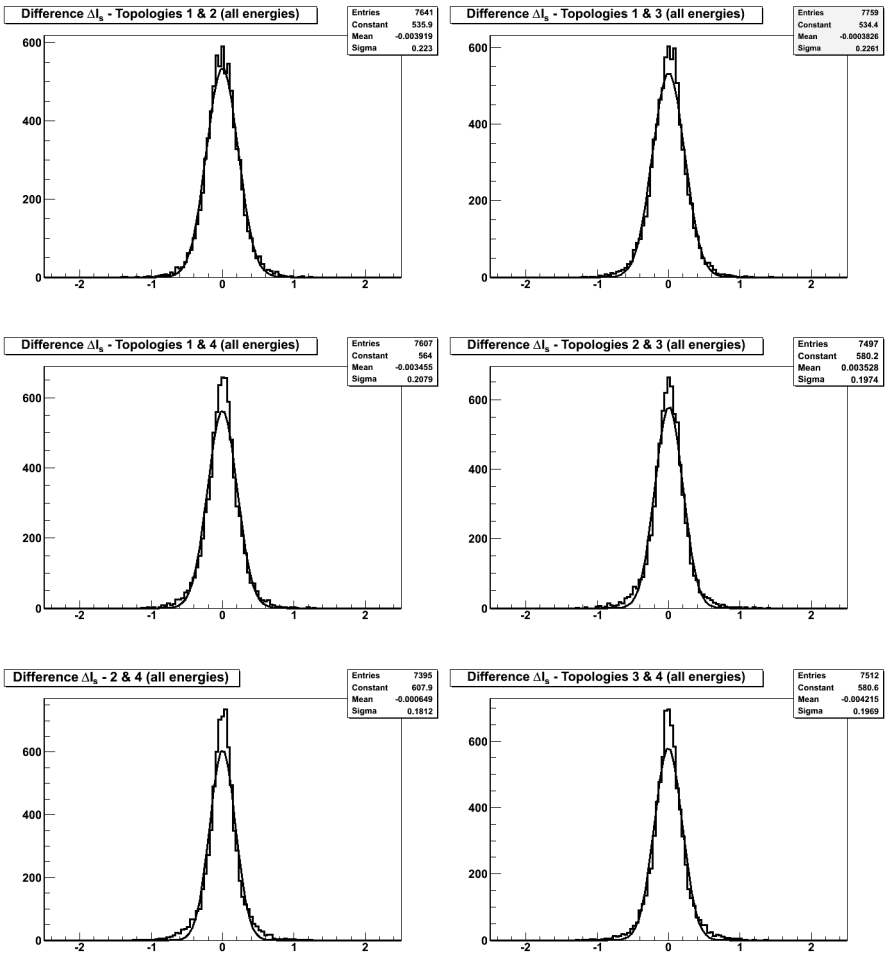

Figure 2.11: Comparisons (differences) between results for I^s from different topologies integrated over all energies. The distributions are all Gaussian in shape and centered at zero hinting at the good consistency between the results from different topologies.

Since $\gamma p \to p\pi\pi$ requires five independent kinematic variables, acceptance effects may still originate from integrating over the remaining two variables. For this reason, we added the differences between Topologies 1, 2 & 4 and the average, Topology 0, to the systematic error. The procedure is described in more details in the next section.

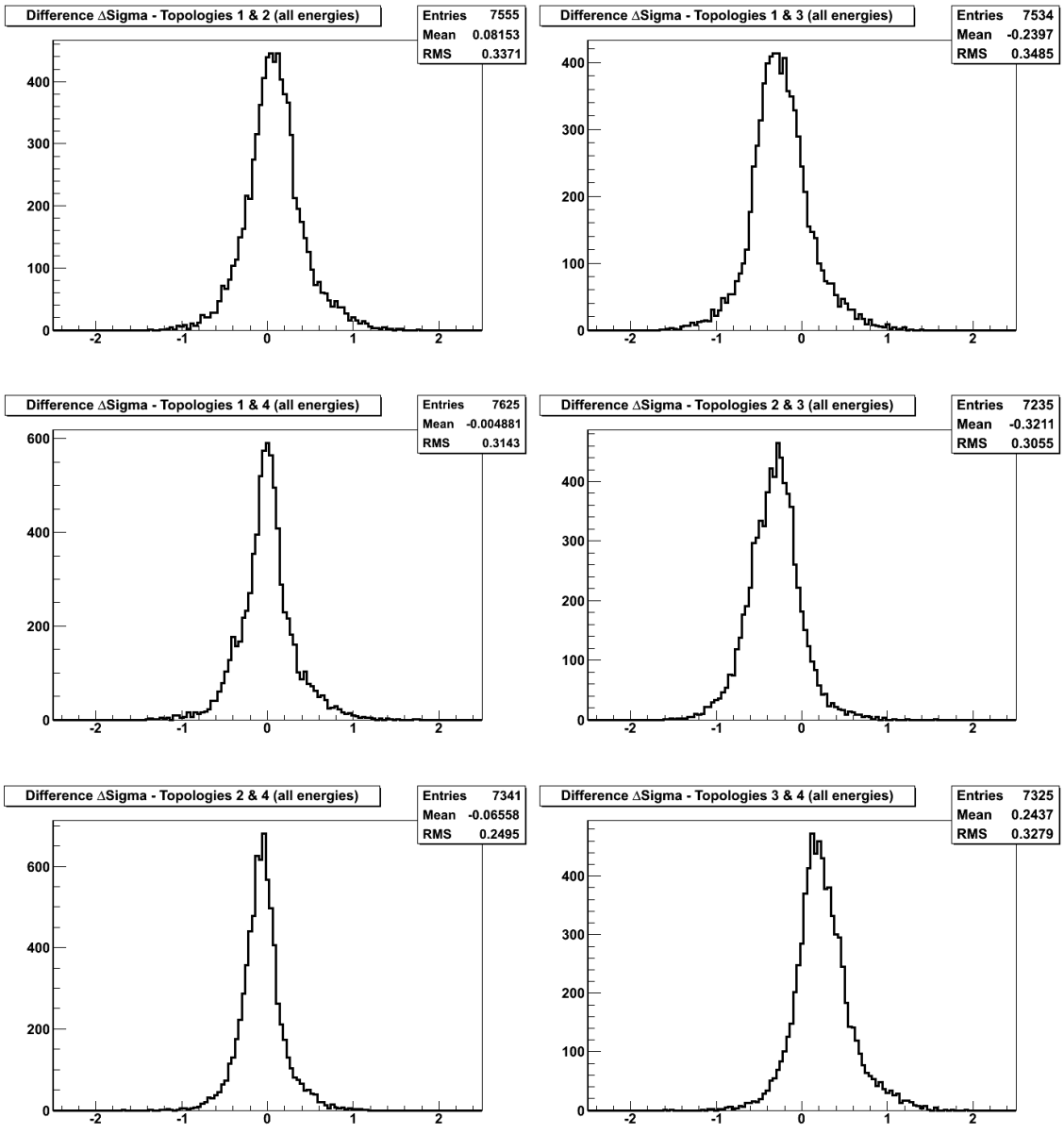

Figure 2.12: Comparisons (differences) between results for I^c from different topologies integrated over all energies. On average, the distributions are slightly broader and significant shifts from zero are observed for those distributions involving Topology 3. For this reason, Topology 3 is not used in this analysis for the final results.

2.6 Systematic Uncertainties

2.6.1 Degree of photon polarization (δ_l)

One important source of systematic uncertainty in this analysis comes from the determination of the degree of polarization of the photons, δ_l, which cannot directly be measured. In order to carry out the calculation, the position of the coherent edge, defined as the part of the photon energy spectrum with the highest negative gradient, must be determined. Naively, this is done by producing a photon enhancement plot (such as the one seen in Figure 2.13 (left)) and then fitting this enhancement plot over the range of the coherent peak. This peak position (determined from the enhancement plot) is then compared to the ANB analytic bremsstrahlung calculation [60]. This calculation models the production of linearly polarized photons produced via an electron beam and a diamond radiator. This modeling allows for the consideration of (and adjustment of) the electron beam divergence as well as the size of the beam spot, both affecting the coherent edge position. This calculation is run many times, varying parameters which affect the degree of polarization such as the electron beam energy, radiator thickness and the geometry of collimator. A more detailed description of these parameters may be found in [61].

All the calculations of the degree of polarization for the g8b run group have been carried by the Glasgow group [62]. Since the position of the coherent peak is not constant over long periods of time, the coherent edge has been determined on an event basis (event edge) and assumed constant only for small groups of about 15,000-20,000 events. As mentioned earlier and can be seen from Figure 2.13 (left), the degree of polarization and statistics of polarized events are largest within 200 MeV below the coherent edge. In addition, our overlap studies between different polarization settings (e.g. the overlap between the 1.3 and 1.5 GeV dataset) confirmed that events outside the 200 MeV window should be excluded from the analysis [63]. We applied the following cut on an event-by-event basis:

$$\text{event edge} - 200\ \text{MeV} < E_\gamma < \text{event edge}\,.$$

The systematic uncertainty involved in the calculation of the photon's degree of linear polarization can be attributed to four sources. The first of these sources arises from the dependence of the degree of polarization on the energy measurement of the photon coming from the Tagger E-plane. In the Tagger hodoscope, up to six of the E-counter bins can be associated with a single T-counter bin. This leads to an uncertainty in the true position of the coherent peak, affecting the calculated degree of polarization. The second source comes from the set of parameters used in the ANB calculations. This uncertainty can be attributed to the fact that there exists a range of values these parameters may possess which would lead to a satisfactory comparison with the data. Thirdly, instabilities in the position of the electron beam lead to instabilities in the position of the coherent edge. This variation in edge position leads to a fluctuation in the degree of polarization of the photons contained in the peak. This fluctuation is of course not handled in the ANB calculations but has been greatly reduced by determining the coherent edge on an event basis. Lastly, the normalization procedure can be affected by the "spikiness" of the photon energy spectra which may cause errors when producing the enhancement plots. All these effects were studied in reference [60]. More practically (and to determine a number for

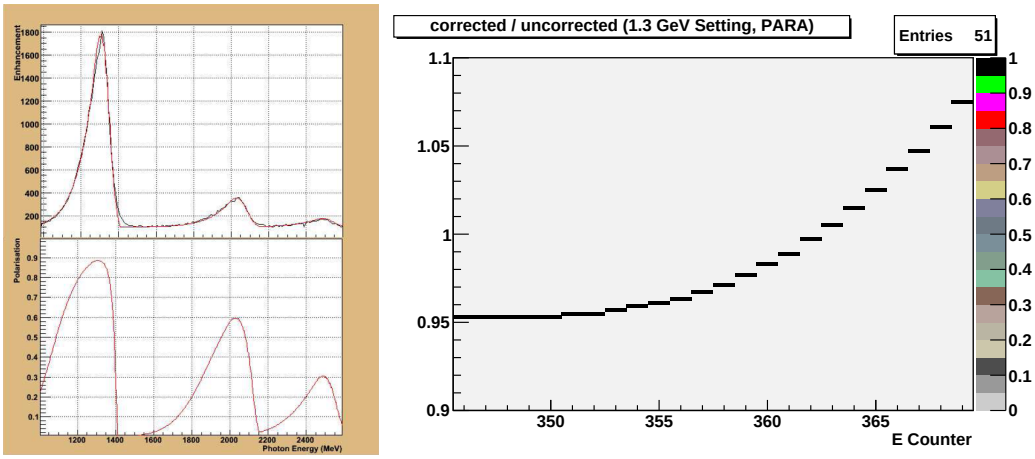

Figure 2.13: (Color online) The top plot of this left figure shows the collimated photon energy spectra compared with the result from the ANB calculation for the 1.3 GeV coherent edge. The bottom (left) plot here shows the degree of photon polarization versus photon energy. The right plot gives an example of the ration corrected / uncorrected degree of polarization (1.3 GeV PARA setting).

the systematic error), we have studied intensively the overlap regions between the different polarization settings [63]. Since the single-pion channel has the best statistics, most of our conclusions are based on this channel. From the comparison of overlapping energy regions between, and within, the different data sets, modifications to the CBSA (Coherent Bremsstrahlung Spectral Analysis) estimated polarizations were developed that improve the self-consistency of the beam asymmetry measurements from g8b data. As a result, the initial event-based polarization values (as determined by the Glasgow group) have been corrected to achieve a self-consistency between the datasets to better than 4 %. Consequently, we have used this number as a fair estimate of the contribution to the total systematic error. Figure 2.13 (right) shows an example of the corrections we have applied to the initial degree of polarization in this analysis. The plot shows the corrections for the 1.3 GeV PARA setting. The use of the 2.1 GeV setting has been somewhat controversial because of our overlap studies. The systematic error is certainly larger and we believe that self-consistency can be achieved only to about 10 %, which is our contribution to the systematic error for this setting.

2.6.2 Effects from averaging

Forming the average value for the polarization observables I^s and I^c provides a way of kinematically extending the observable measurements across topology dependencies. These average values are determined by first extracting the polarization observables per kinematic bin combination per final state topology. Once all of the observable measurements have been made, this average value is determined.

Fig. 2.14 shows ratio and difference plots for the observable I^s comparing Topologies 1 (missing π^-), 2 (missing π^+), and 4 (all particles detected) with Topology 0 (average). The top row shows the ratios and the bottom row shows the differences integrated over all energies. The differences are all symmetric around zero and very narrow which indicates

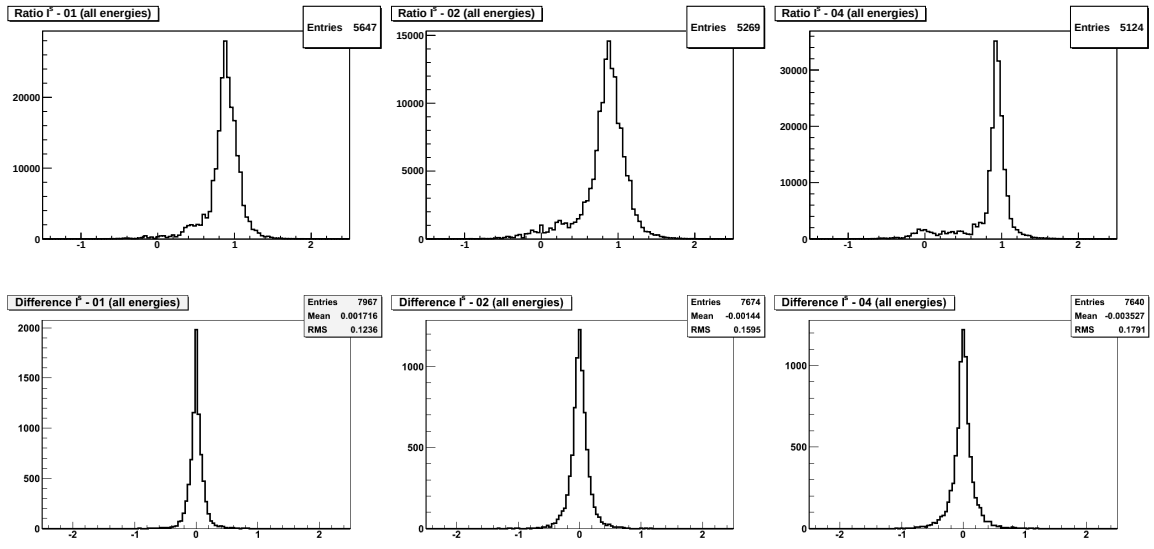

Figure 2.14: Comparisons (differences and ratios) of results for I^s from Topologies 1, 2, 4 with Topology 0 integrated over all energies and angles. The top plots show the ratios and the bottom plots the differences.

that the shape of the observables is very similar for all topologies. The peak values for the ratios are fairly close to one. Note that the ratio plots (integrated over all energies and angles) do not represent statistical distributions (we do not necessarily expect a perfect Gaussian shape) but partially depend on the different shape of the observables for different energies. Since we have applied a binning in only three of the five independent variables (for Fig. 2.14, we have used E_γ, $\cos\theta^*_{\pi^+}$, and $\phi^*_{\pi^+}$), we conclude that deviations of the peak value from one originate from integrating over the remaining two variables (here: $\cos\theta^{\text{c.m.}}_{\text{proton}}$ and a mass, e.g. $m_{p\pi^+}$).

Although the ratio may aquire, in some cases, values far away from one, we have observed that the corresponding (absolute) differences are still very small. We found that the left-side tails (top row: < 0.5) are mostly based on two issues. Fig. 2.15 shows the observable I^s for $1150 < E_\gamma < 1200$ MeV. The red points denote Topology 0 (average of Topologies 1, 2, and 4) and the blue points denote Topology 2. Fig. 2.16 shows a similar comparison between Topology 0 and Topology 4. Since the observable aquires very small values for $-1.0 < \cos(\theta^*_{\pi^+}) < -0.9$ and is almost consistent with zero, very small absolute differences between two data points can result in large ratios although the data points are still statistically consistent. In addition, statistical fluctuations due to small detector efficiencies are large around $\phi^*_{\pi^+} = 0.0$ for $0.0 < \cos(\theta^*_{\pi^+}) < 1.0$ (Topology 2) and $-0.5 < \cos(\theta^*_{\pi^+}) < 0.5$ (Topology 4). Our studies confirmed that almost all entries in the left-side tails (< 0.5) in Fig. 2.14 (top row) are based on these two issues.

For this reason, we have added the differences between individual topologies (1, 2, and 4) and the average to the total systematic error to account for the remaining accpetance effects. We have however weighted the difference for a particular topology with the corresponding statistical difference error in order to reduce effects due to statistical fluctuations.

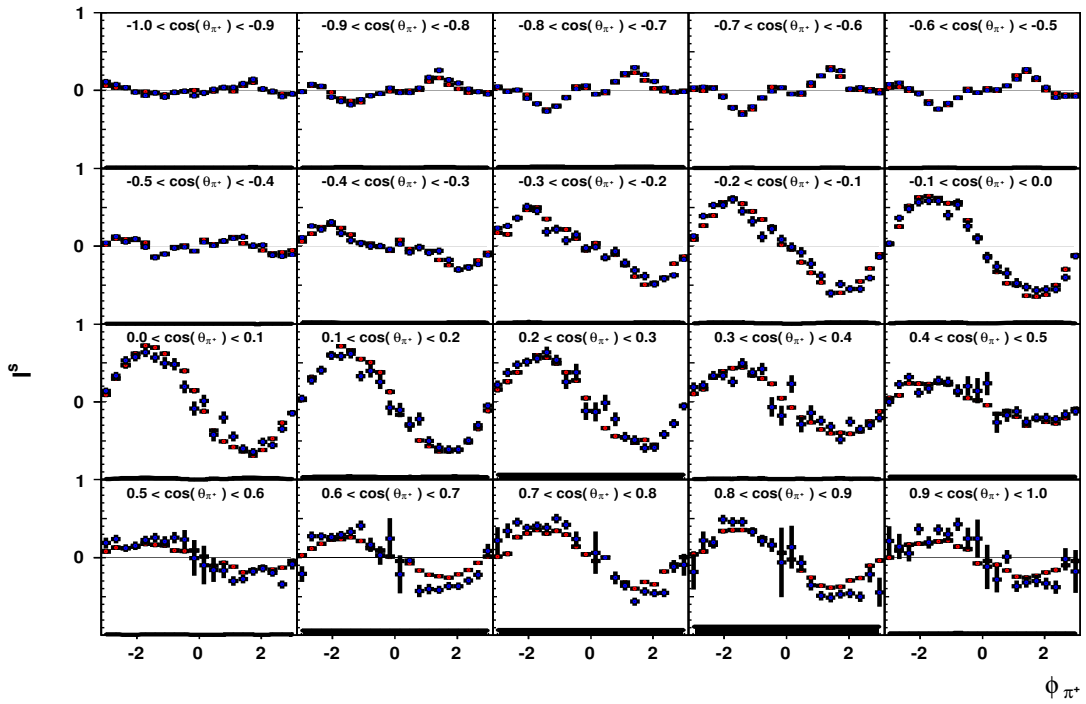

Figure 2.15: Comparison between Topology 0 (red points) and Topology 2 (blue points, reaction: $\gamma p \to p\pi^-\pi^+_{\text{missing}}$). Shown is the Observable I^s for $1150 < E_\gamma < 1200$ MeV. The error band at the bottom includes contributions from offset and symmetry effects (for the particular topology) and from the polarization. See text for more details.

2.6.3 Symmetry effects

Symmetry properties allow for a further cross check of our data. The observable I^s has to vanish for coplanar kinematics ($I^s(\phi^* = -\pi) = I^s(\phi^* = 0) = I^s(\phi^* = \pi) = 0$) and the transition $\phi^* \to 2\pi - \phi^*$ is equivalent to a mirror operation with respect to the reaction plane. In the case of linear polarization this leads to the transition $\beta \to 2\pi - \beta$ and because $\sin(2\cdot(2\pi - \beta)) = -\sin(2\beta)$ to $I^s \to -I^s$ (see Eqs. (2.9) and (2.10)). A very similar argument is true for Σ so that $\Sigma \to \Sigma$ for the above transition. These symmetry properties are clearly visible in the data. Since we use 20 bins in ϕ^*, we have determined the average value of all I^s (bin i) + I^s (bin 21 - bin i) pairs as well as all I^c (bin i) − I^c (bin 21 - bin i) pairs. These values are extremely small but have also been added to the total systematic error.

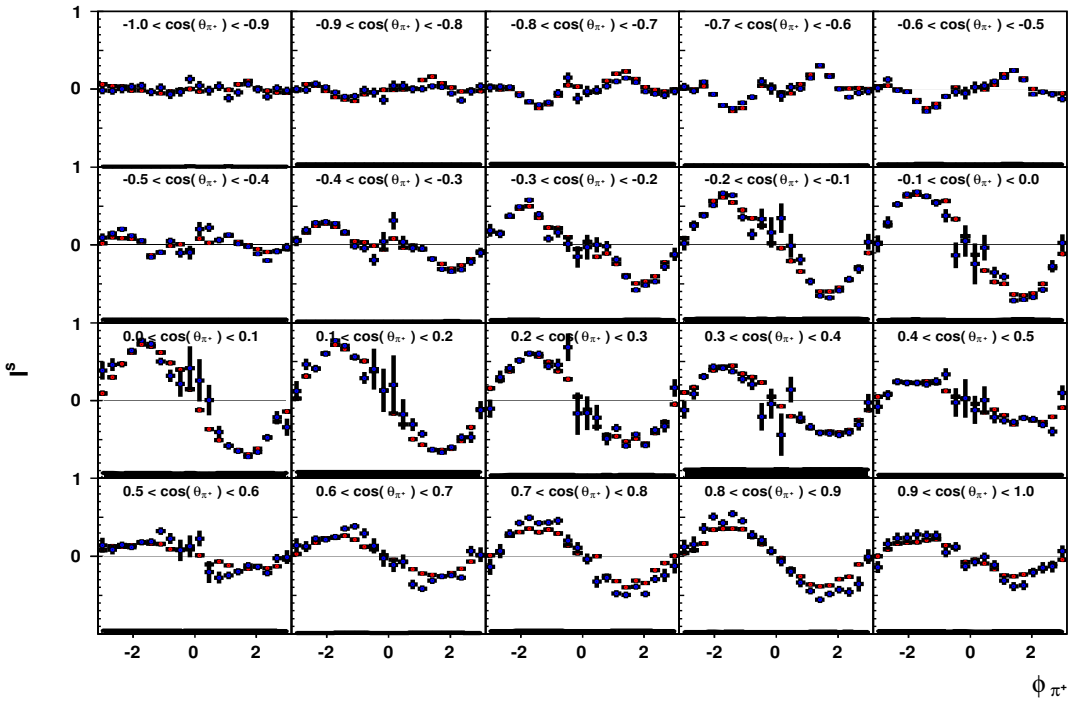

Figure 2.16: Comparison between Topology 0 (red points) and Topology 4 (blue points, reaction: $\gamma p \to p\pi^-\pi^+$). Shown is the Observable I^s for $1150 < E_\gamma < 1200$ MeV. The error band at the bottom includes contributions from offset and symmetry effects (for the particular topology) and from the polarization. See text for more details.

CHAPTER 3

MEASUREMENT RESULTS AND DISCUSSION

The following pages show our experimental results for the two beam asymmetries in two-pion photoproduction. These beam asymmetries using a linearly-polarized beam are first-time measurements and have not been published before. Figures 3.1-3.20 give the results for I^s and Figures 3.21-3.40 the results for the independent observable I^c, which is traditionally called Σ for single-meson final states. As a reminder, a two-meson final states results in two beam asymmetries due to the fact that the decay or reaction plane forms an angle with the production plane. If this angle has a value of $-\pi$, 0, or π, the final state is considered *in plane* and the observable I^s vanishes. This behavior is clearly visible in the following figures. We also point out that I^s shows the expected odd behavior when plotted versus ϕ^*. Moreover, I^c shows the expected even behavior when plotted versus ϕ^*.

Each figure has a "fixed" energy in terms of 50 MeV-wide bins ranging from 1.1 GeV to 2.1 GeV; the energy interval is given in the figure caption. Moreover, the observables are displayed in two different ways. For the top plot in each figure, we have used the three independent variables, E_γ, ϕ^*, and $m_{p\pi^+}$; the observable is plotted in 20 bins of ϕ^* from $-\pi$ to π versus $m_{p\pi^+}$ ranging from 1.0 GeV/c^2 to 2.0 GeV/c^2. For the bottom plot in each figure, we have used the three independent variables, E_γ, ϕ^*, and θ^*; the observable is plotted in 20 bins of $\cos\theta^*$ from -1.0 to 1.0 versus ϕ^*. The two angles ϕ^* and θ^* represent the polar and azimuthal angle of the π^+ meson in the rest frame of the two pions. Since the two-pion final state requires five independent kinematic variables, many other ways to display the observables are possible. At this point, there is no standard or clear convention as to how to display the observables for a two-meson final state. The current choice of variables may not be final.

At this point of the review, the figures only show the experimental results. A physics interpretation of the data is under development, but will require more time. Unfortunately, the standard MAID, SAID or Bonn-Gatchina solutions are not available for the photoproduction of more than one meson in the final state. We are working with theorists on including these data in various partial-wave analyses and models. While this analysis note only describes the experimental procedure to extract the observables, Charles Hanretty's thesis discusses somewhat more physics in chapter 5.

Finally, Figure 3.41 shows typical ϕ_{lab} distributions for the reaction $\gamma p \to p\pi^+\pi^-_{\text{missing}}$ corresponding to results shown in Fig. 3.1 and 3.21 ($E_\gamma \in [1.10, 1.15]$). Thousands of additional figures of this kind are certainly available upon request.

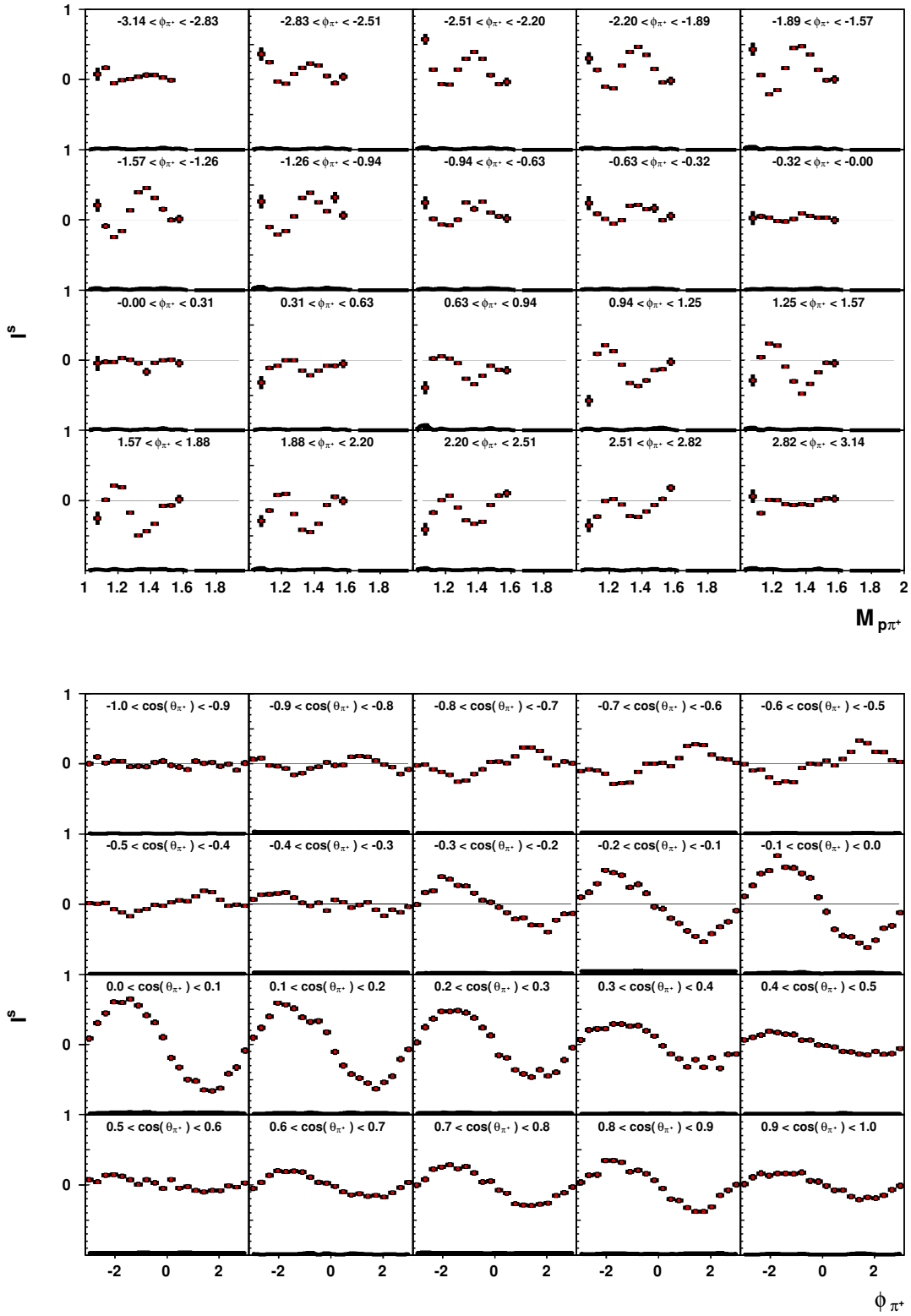

Figure 3.1: Results for the observable I^s, $E_\gamma \in [1.10, 1.15]$ GeV.

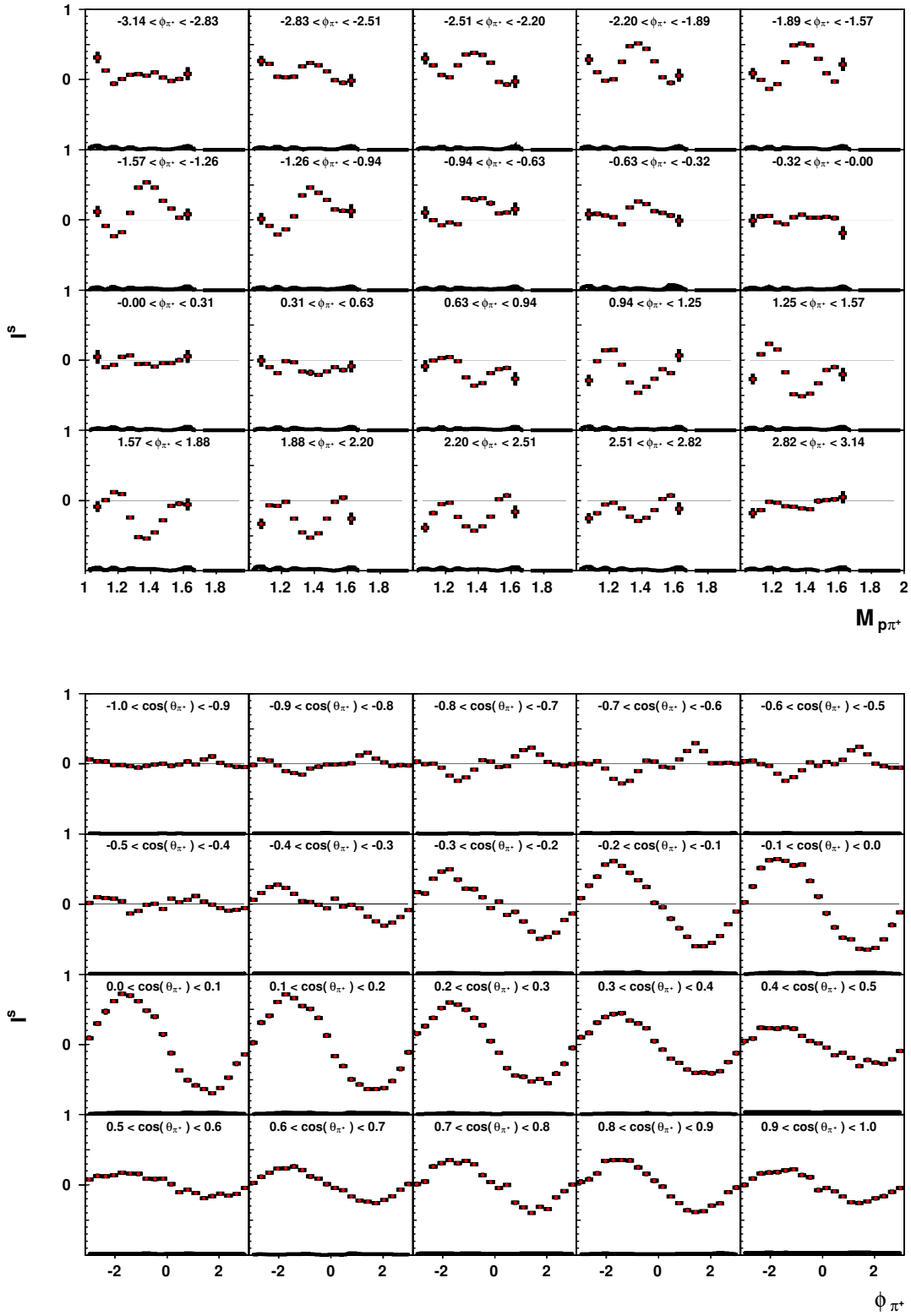

Figure 3.2: Results for the observable I^s, $E_\gamma \in [1.15, 1.20]$ GeV.

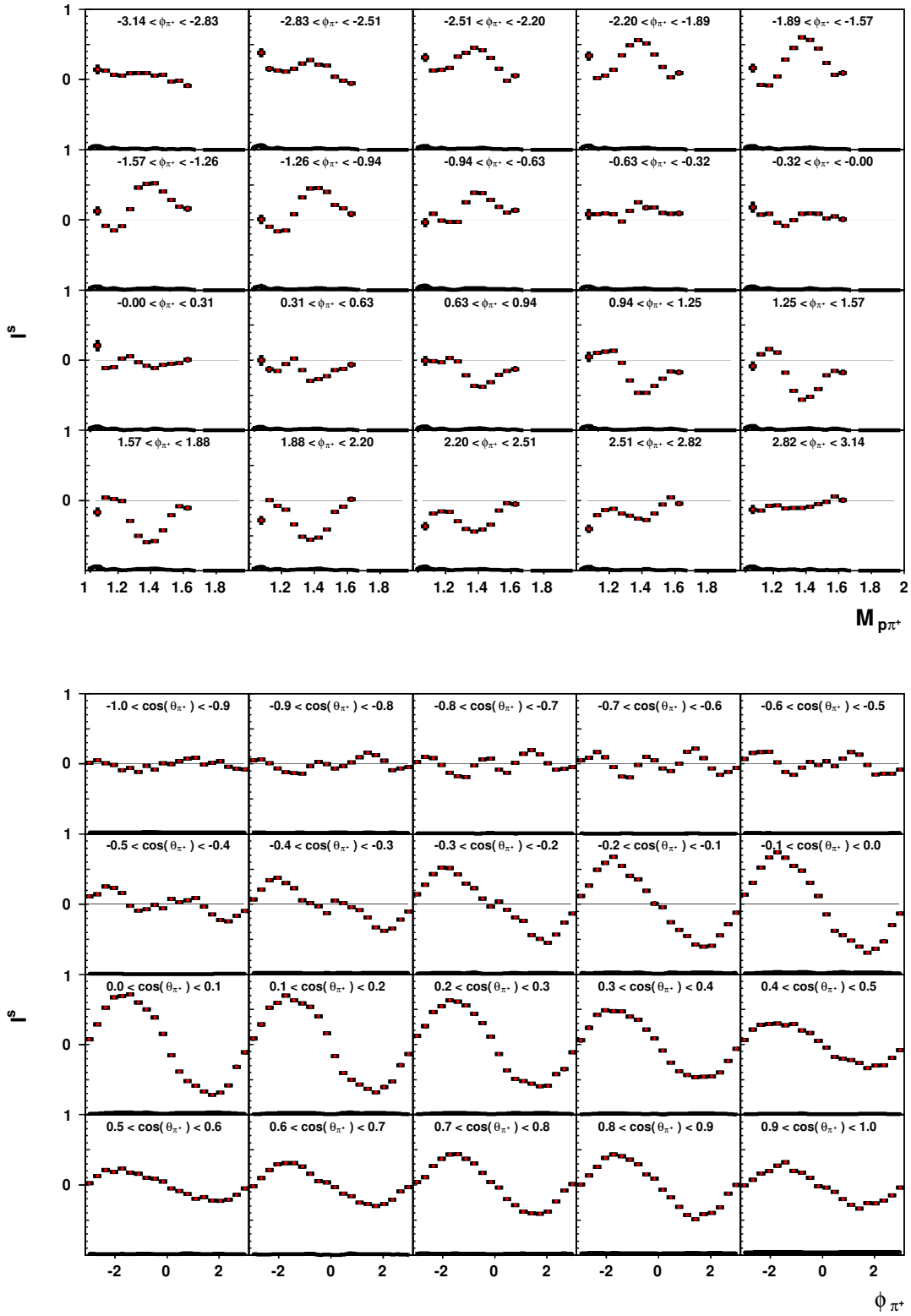

Figure 3.3: Results for the observable I^s, $E_\gamma \in [1.20, 1.25]$ GeV.

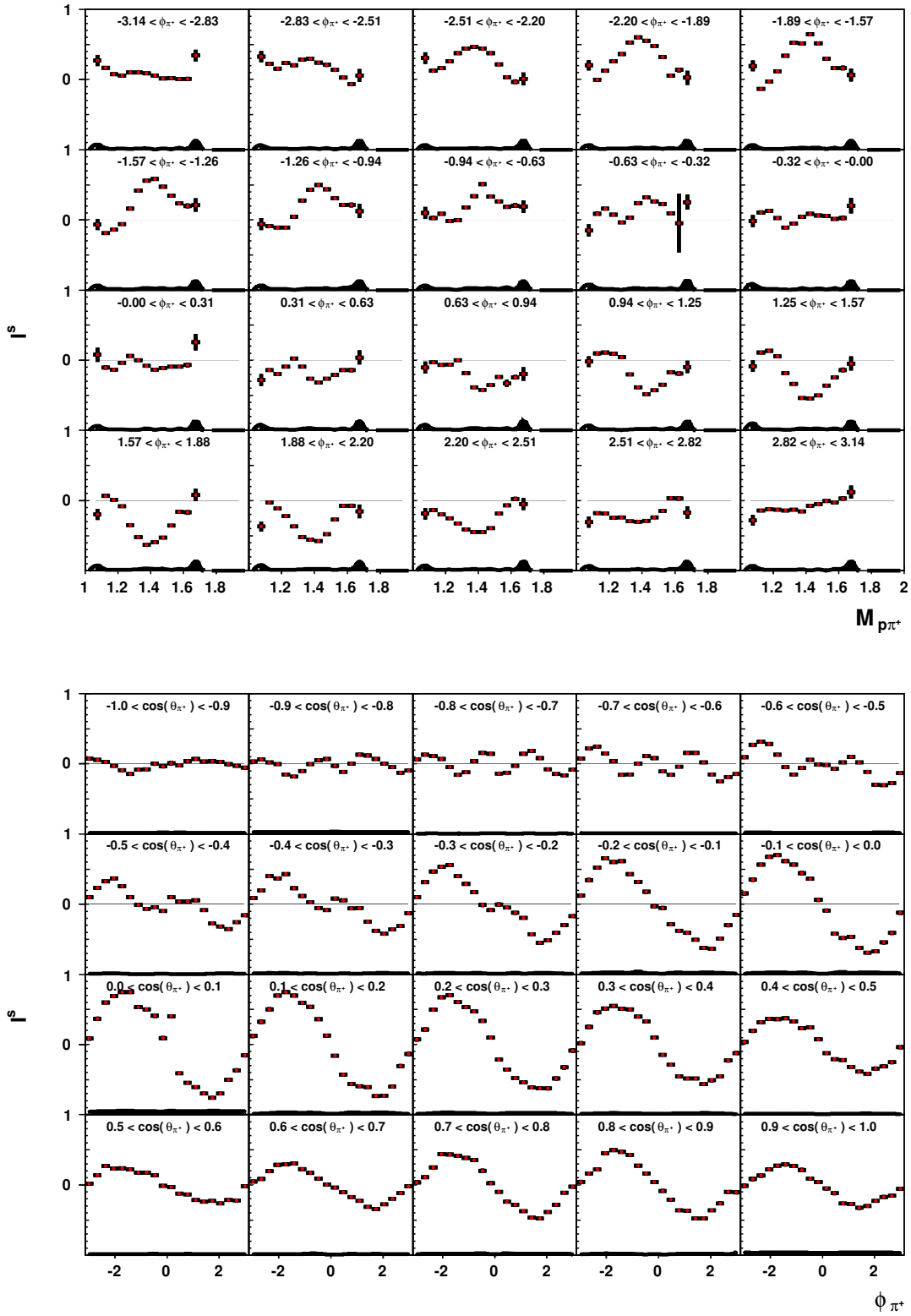

Figure 3.4: Results for the observable I^s, $E_\gamma \in [1.25, 1.30]$ GeV.

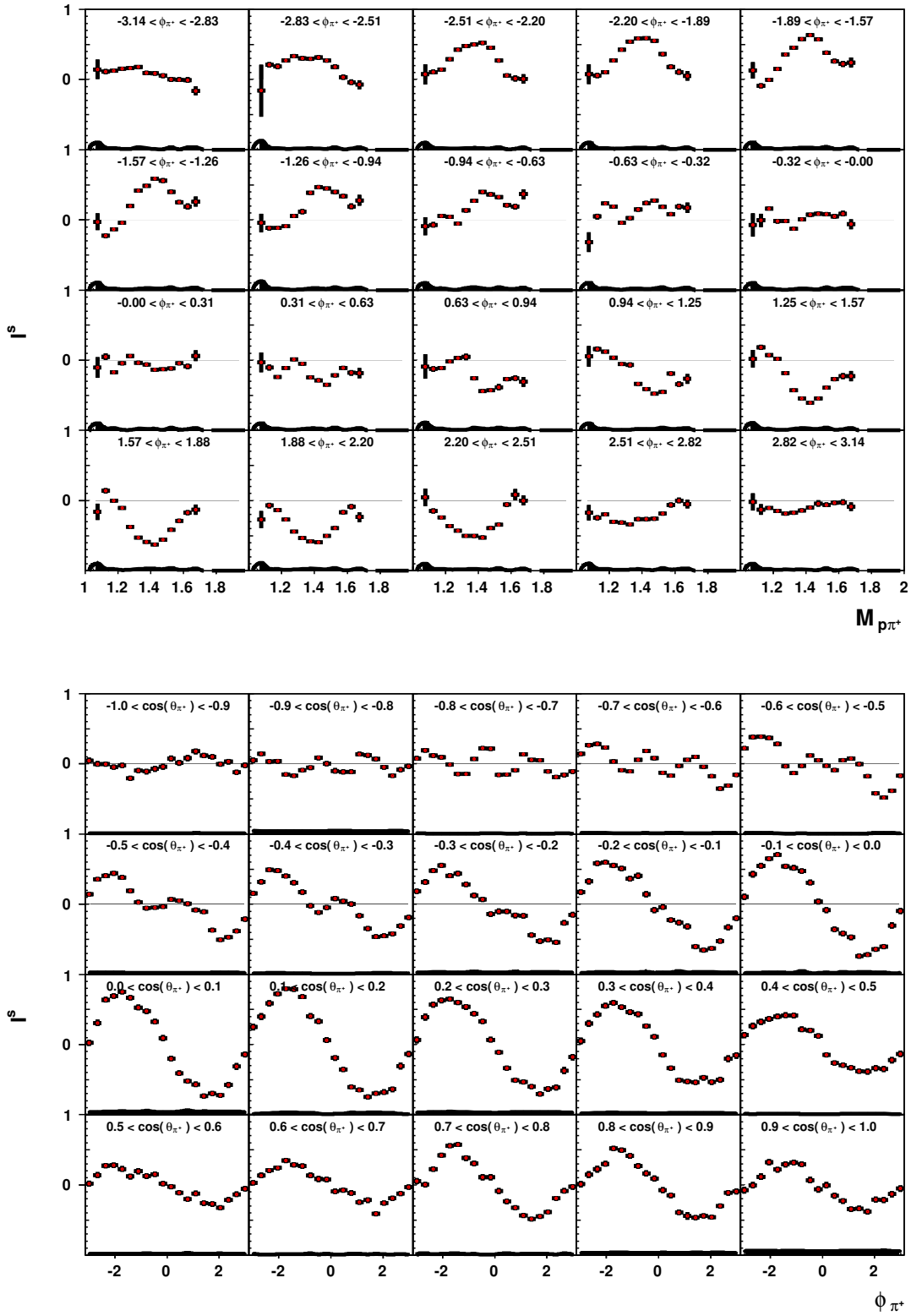

Figure 3.5: Results for the observable I^s, $E_\gamma \in [1.30, 1.35]$ GeV.

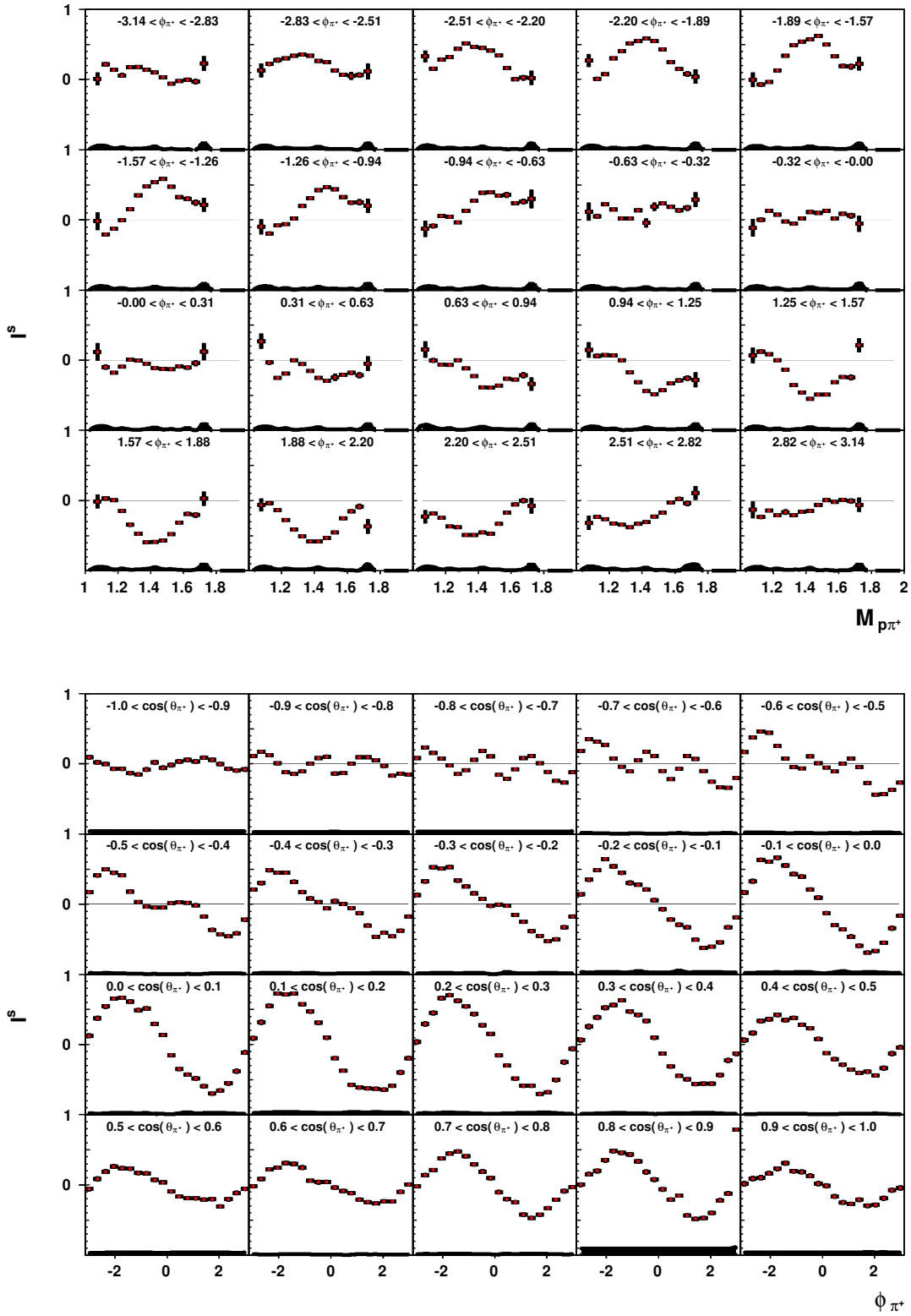

Figure 3.6: Results for the observable I^s, $E_\gamma \in [1.35, 1.40]$ GeV.

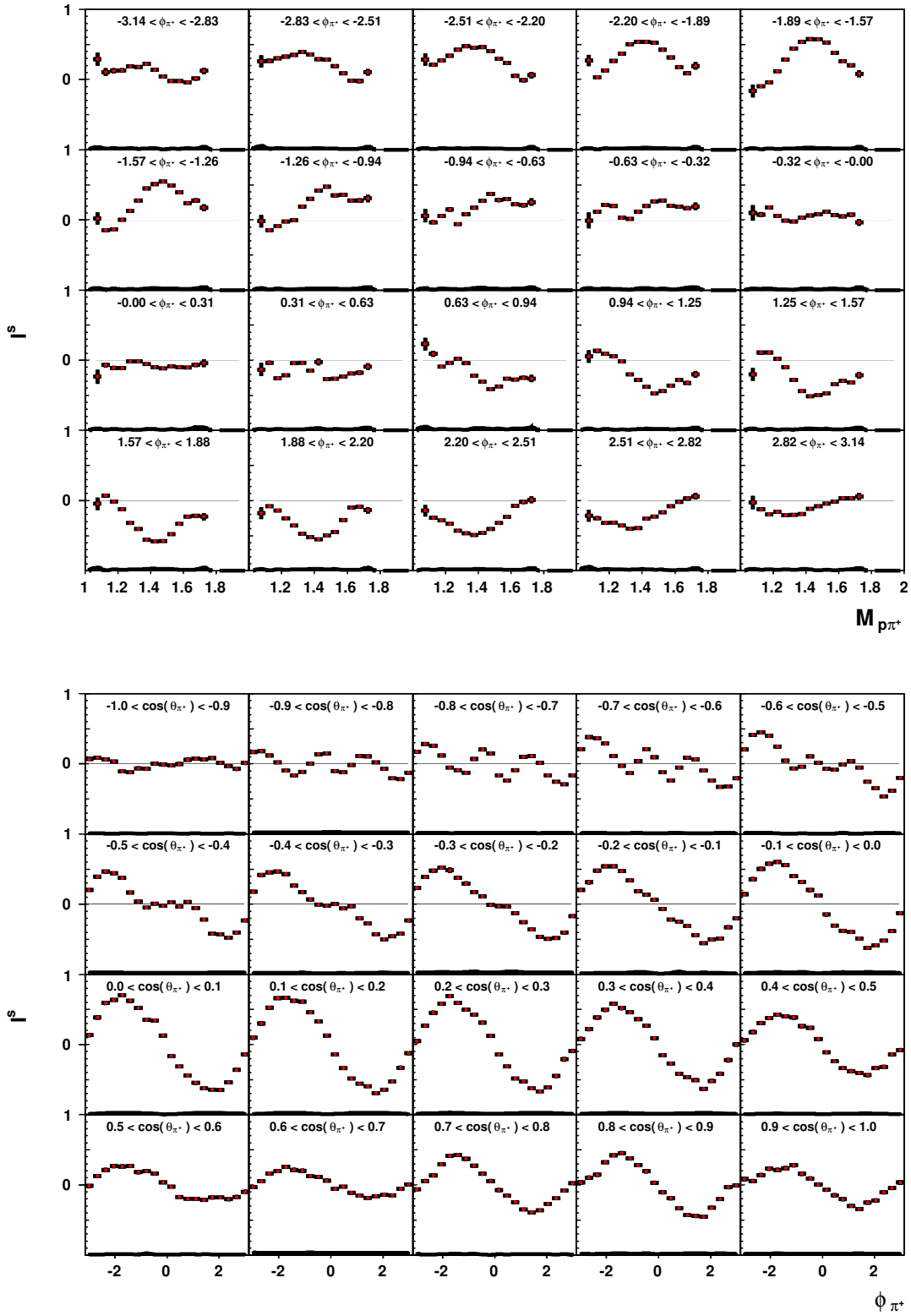

Figure 3.7: Results for the observable I^s, $E_\gamma \in [1.40, 1.45]$ GeV.

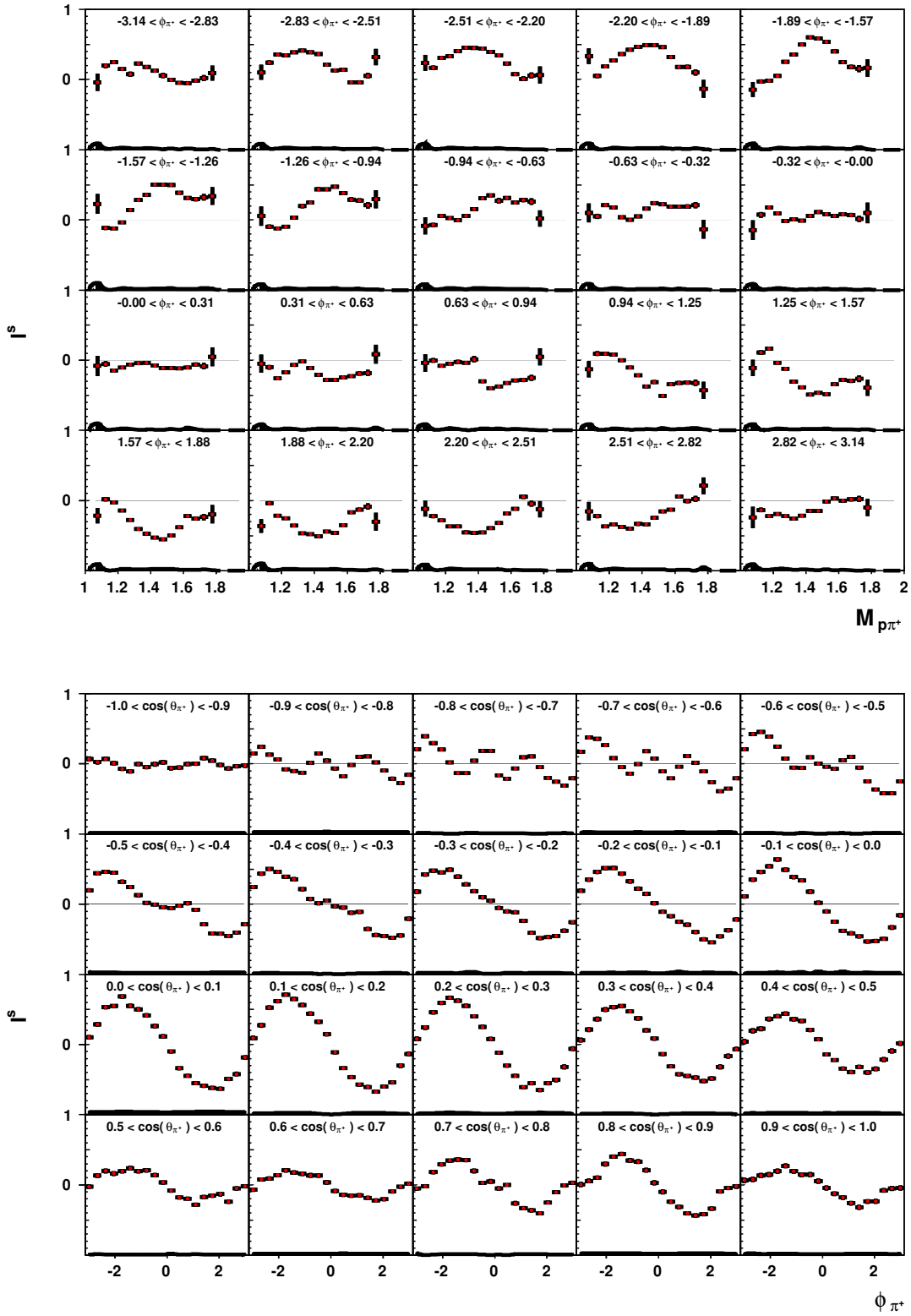

Figure 3.8: Results for the observable I^s, $E_\gamma \in [1.45, 1.50]$ GeV.

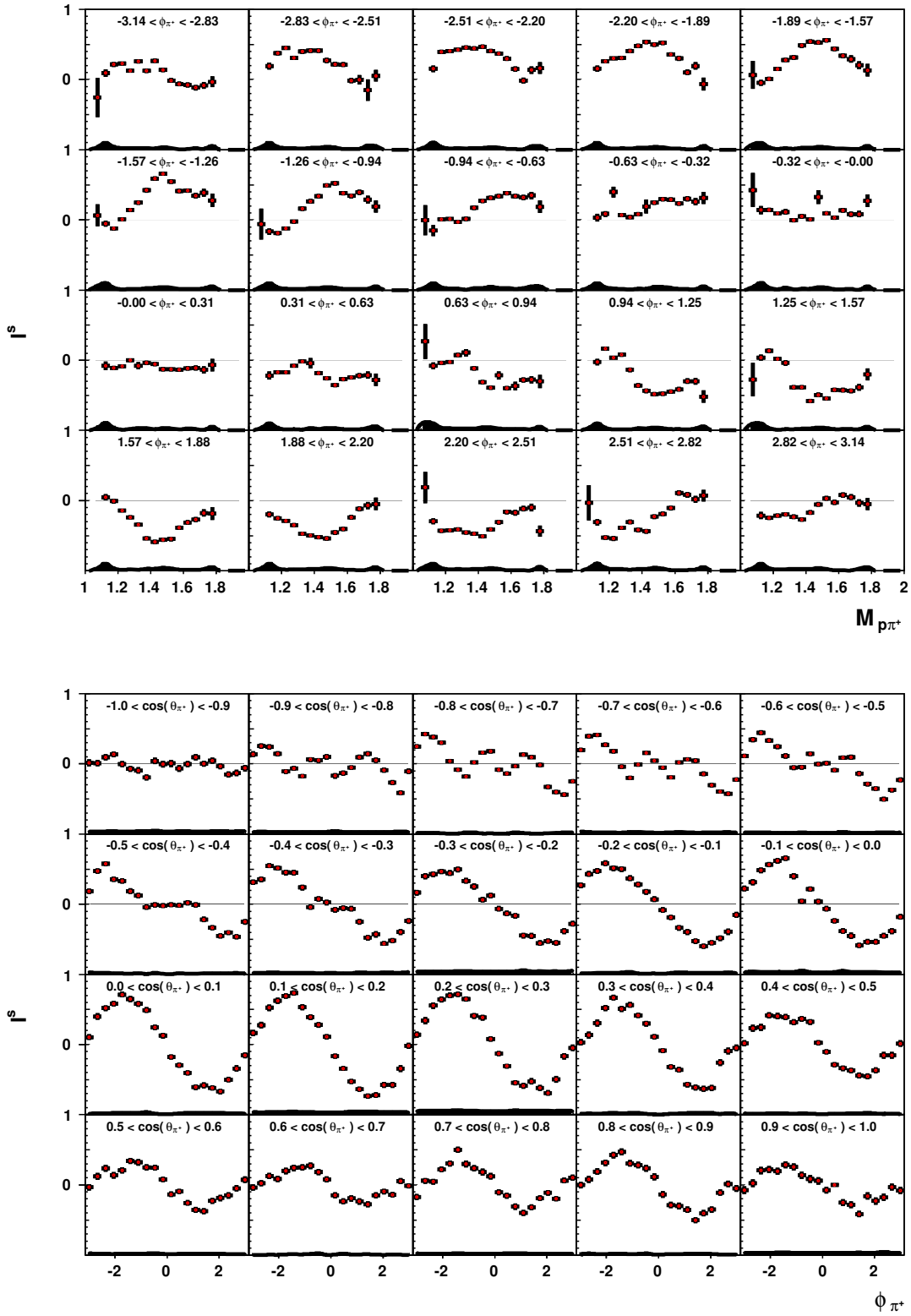

Figure 3.9: Results for the observable I^s, $E_\gamma \in [1.50, 1.55]$ GeV.

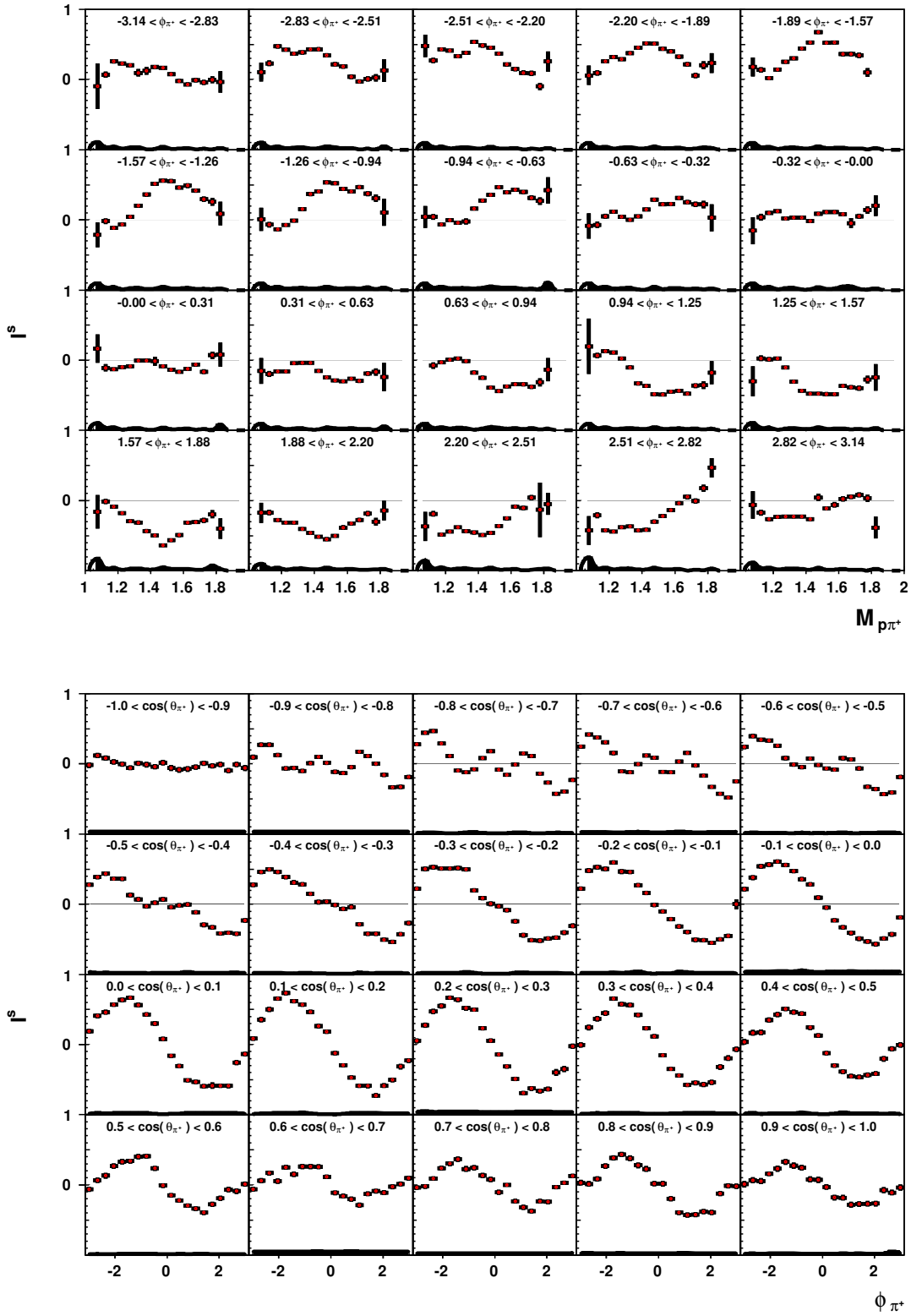

Figure 3.10: Results for the observable I^s, $E_\gamma \in [1.55, 1.60]$ GeV.

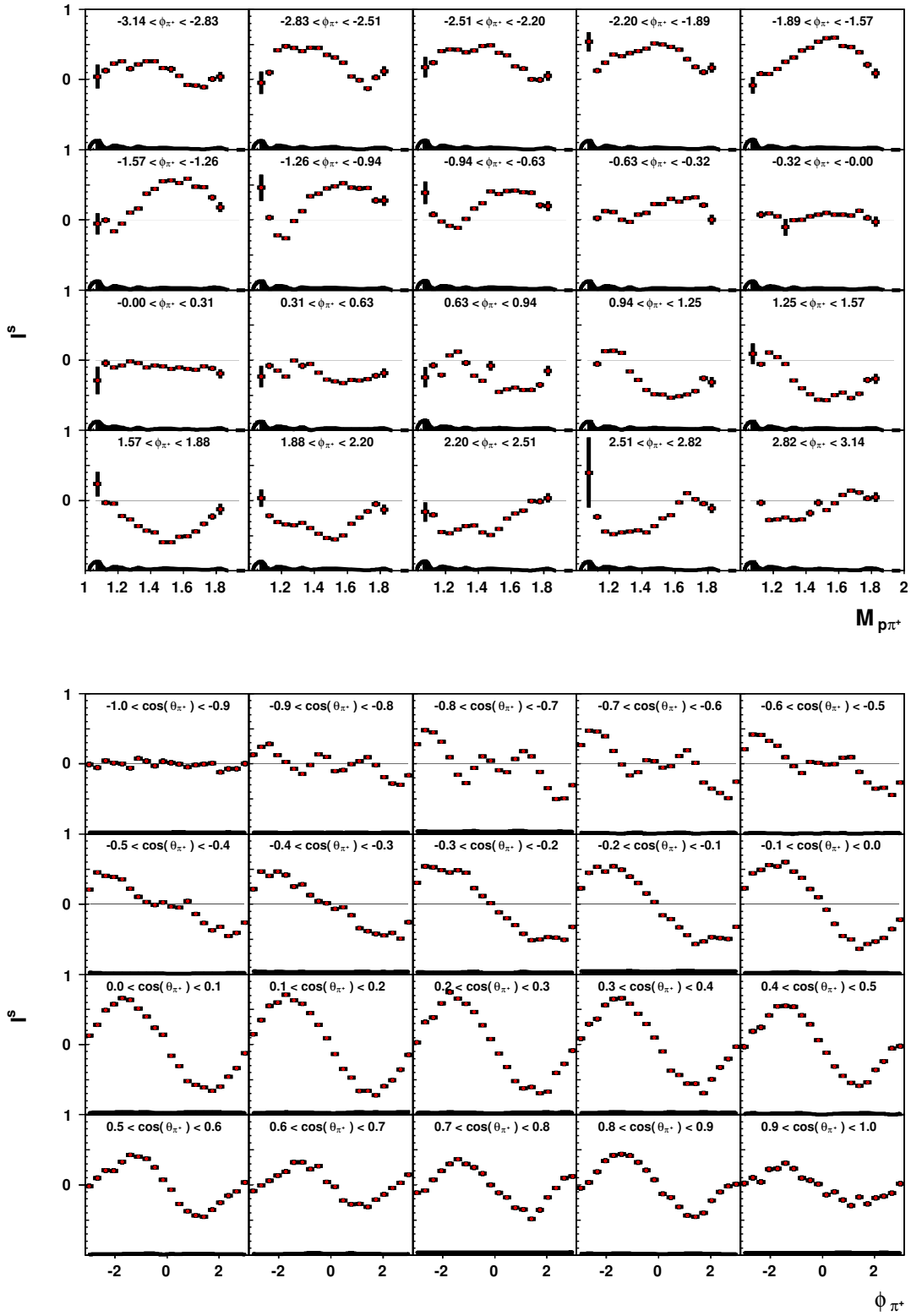

Figure 3.11: Results for the observable I^s, $E_\gamma \in [1.60, 1.65]$ GeV.

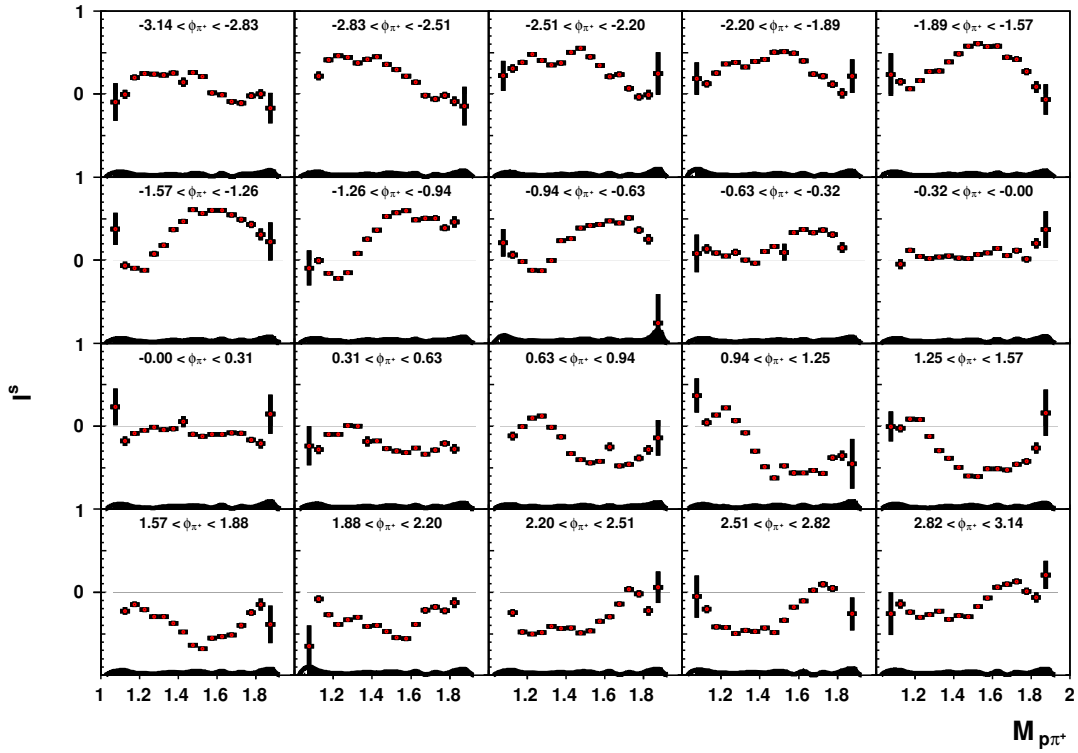

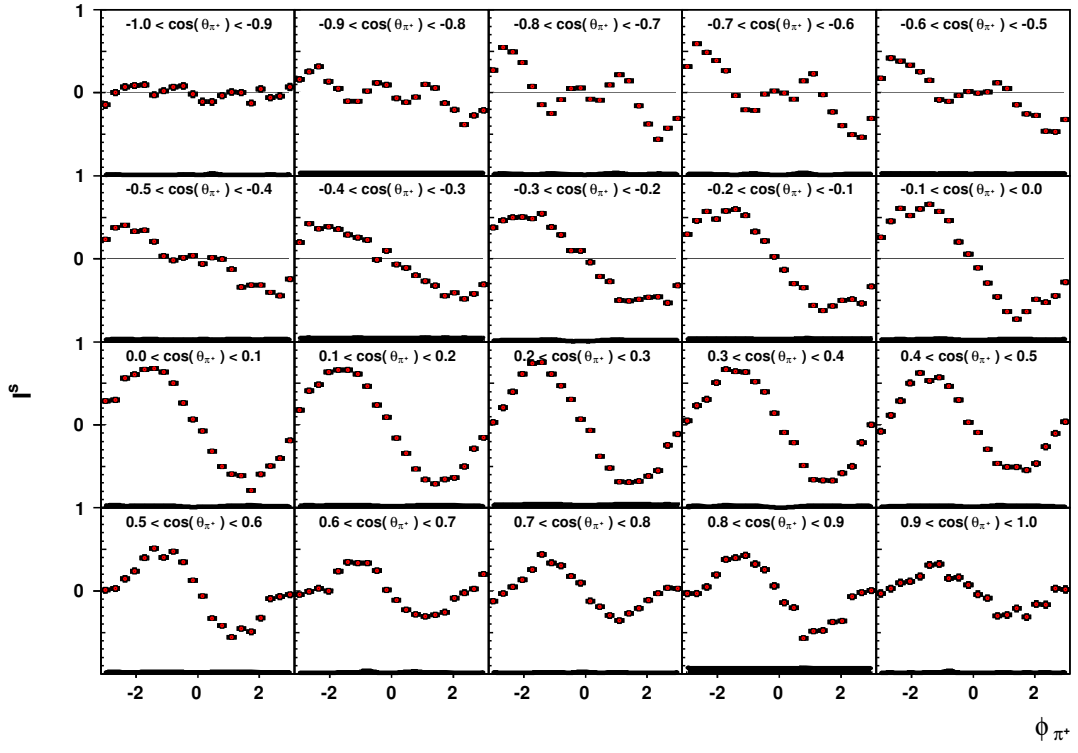

Figure 3.12: Results for the observable I^s, $E_\gamma \in [1.65, 1.70]$ GeV.

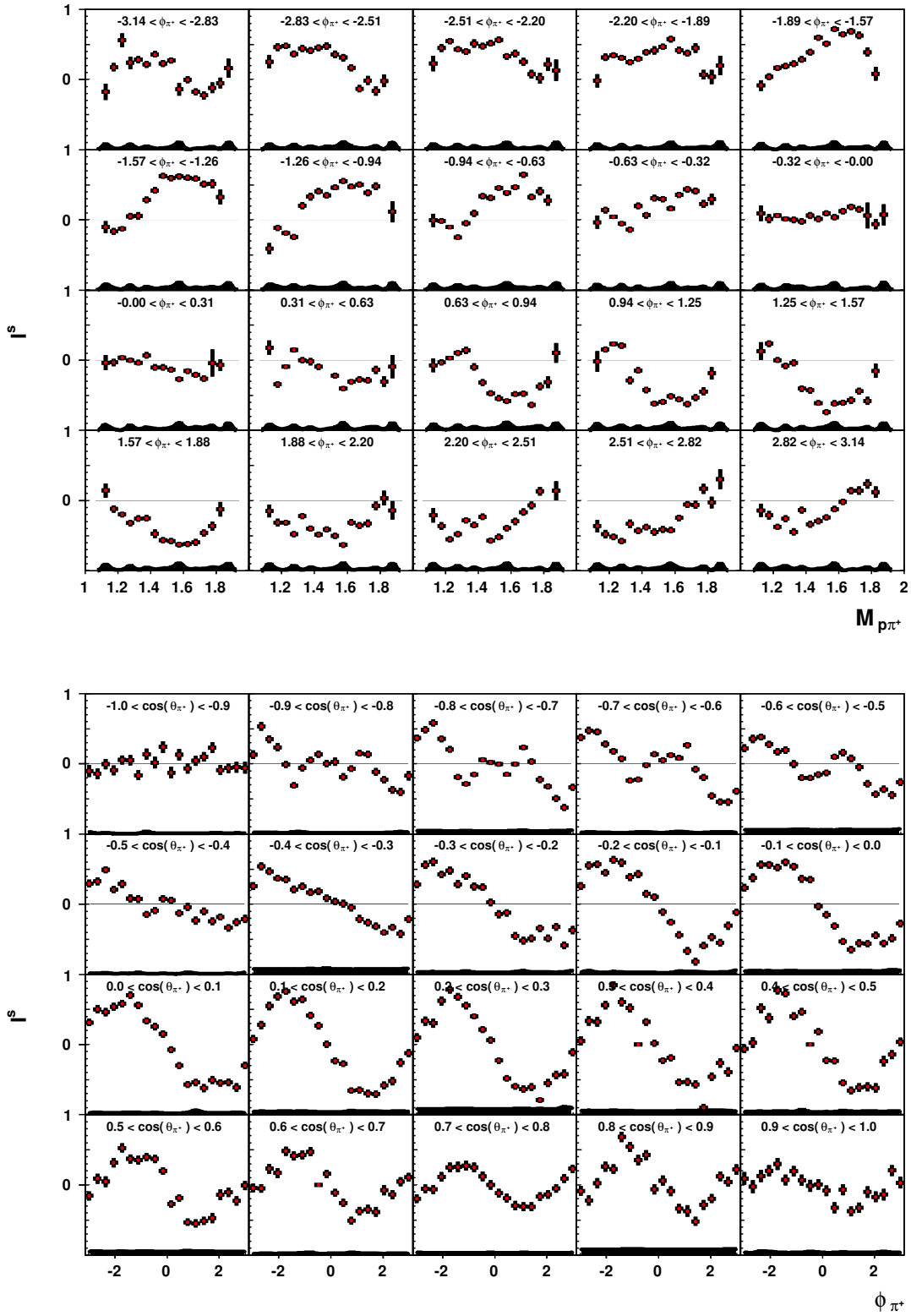

Figure 3.13: Results for the observable I^s, $E_\gamma \in [1.70, 1.75]$ GeV.

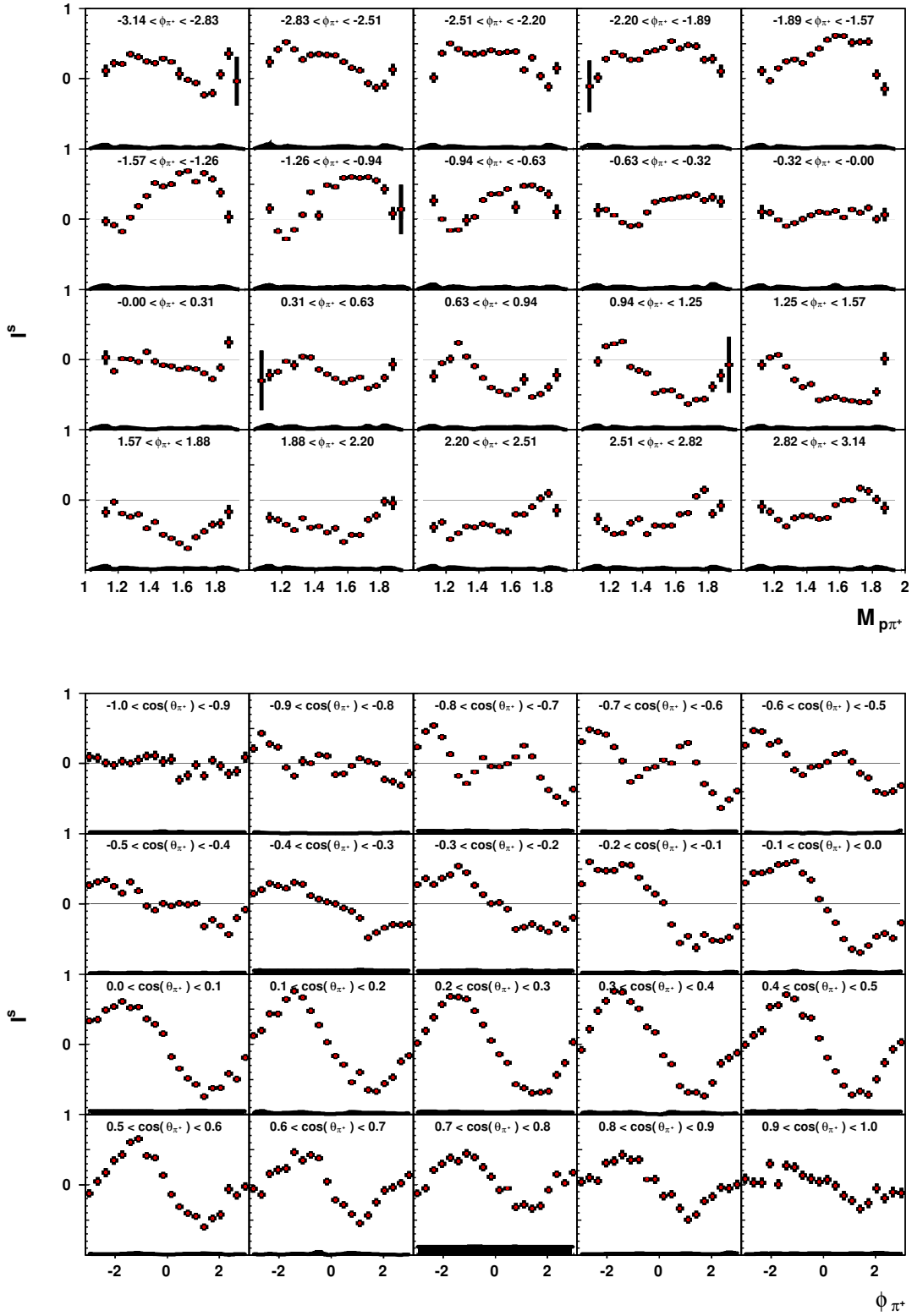

Figure 3.14: Results for the observable I^s, $E_\gamma \in [1.75, 1.80]$ GeV.

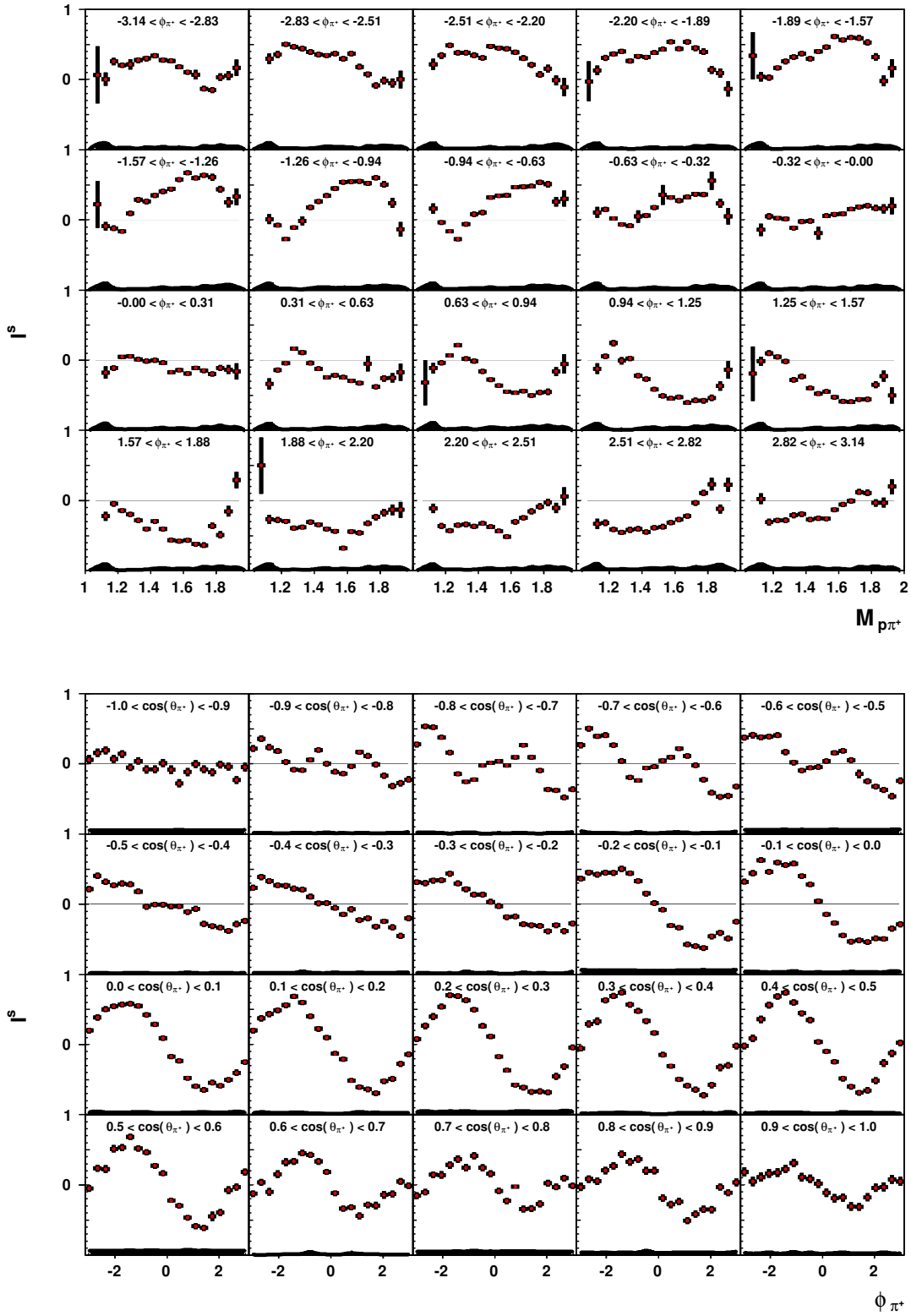

Figure 3.15: Results for the observable I^s, $E_\gamma \in [1.80, 1.85]$ GeV.

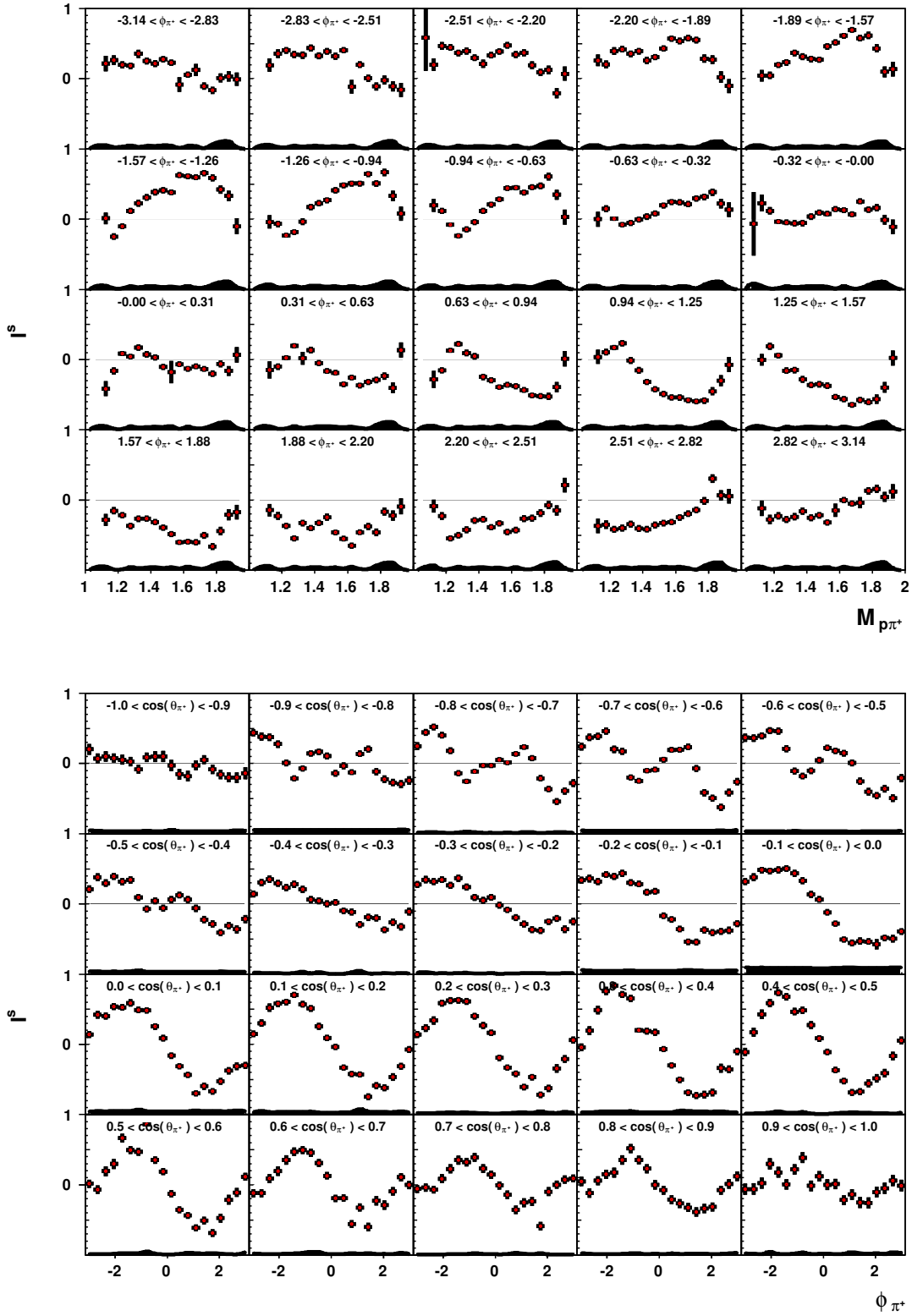

Figure 3.16: Results for the observable I^s, $E_\gamma \in [1.85, 1.90]$ GeV.

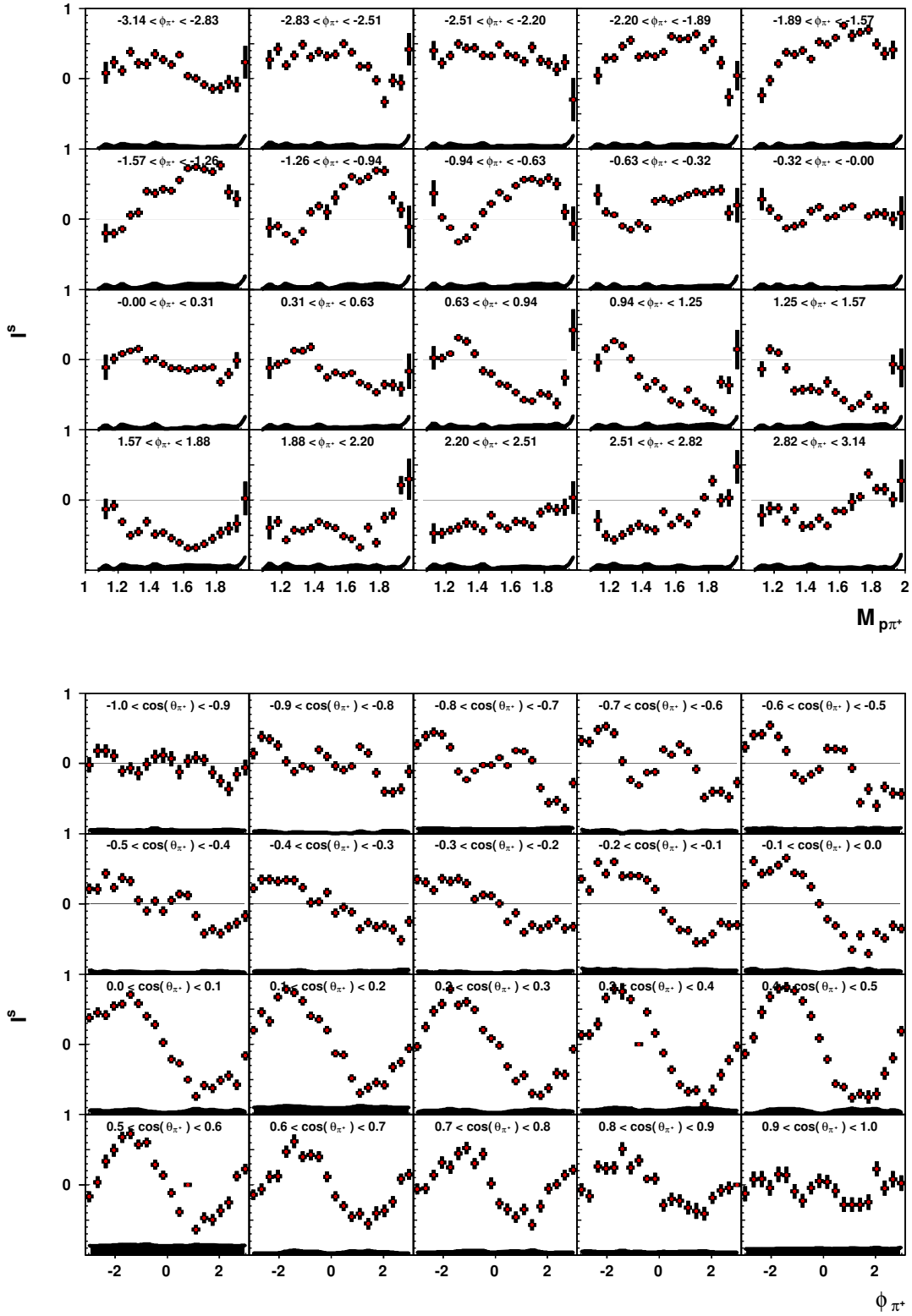

Figure 3.17: Results for the observable I^s, $E_\gamma \in [1.90, 1.95]$ GeV.

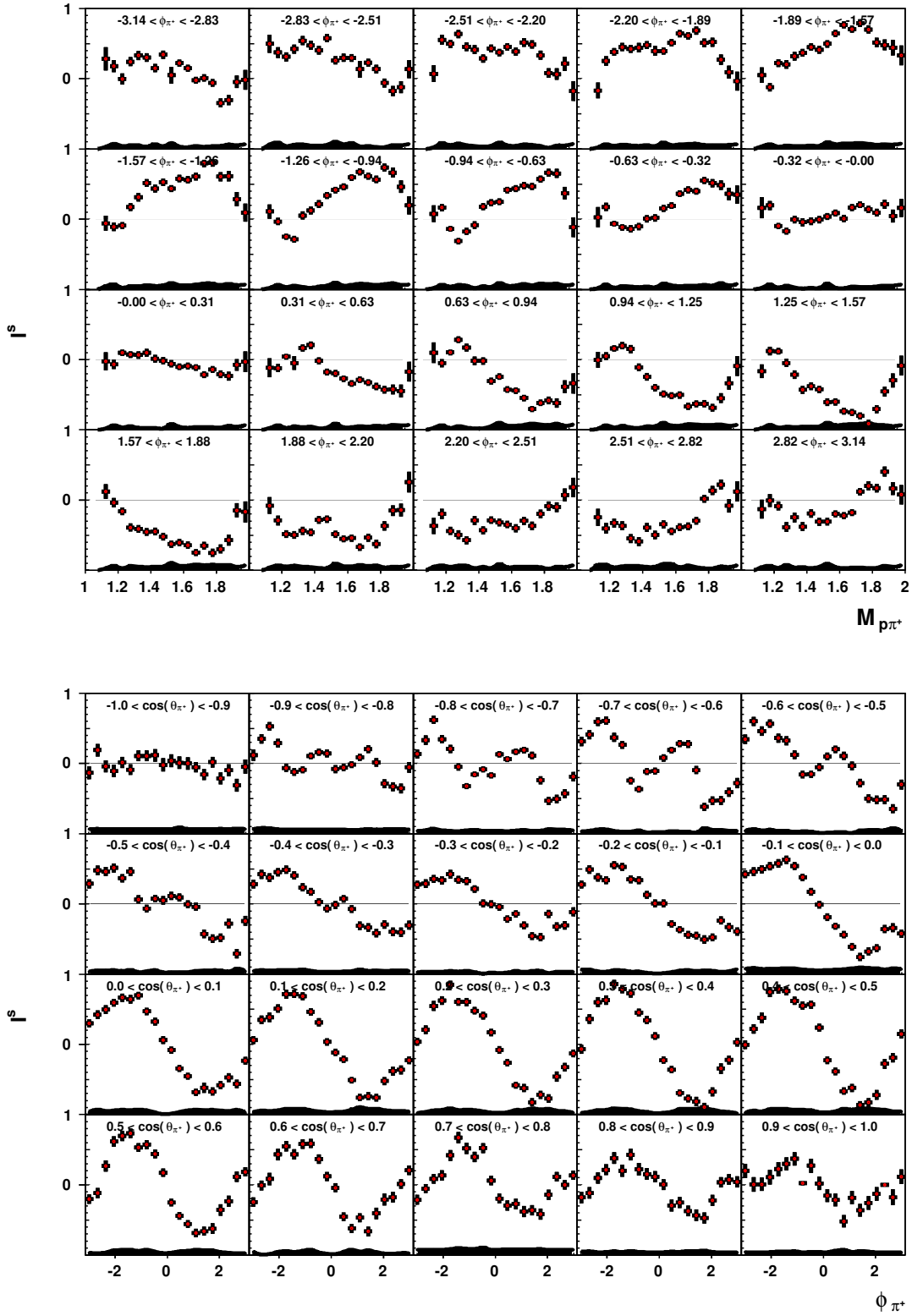

Figure 3.18: Results for the observable I^s, $E_\gamma \in [1.95, 2.00]$ GeV.

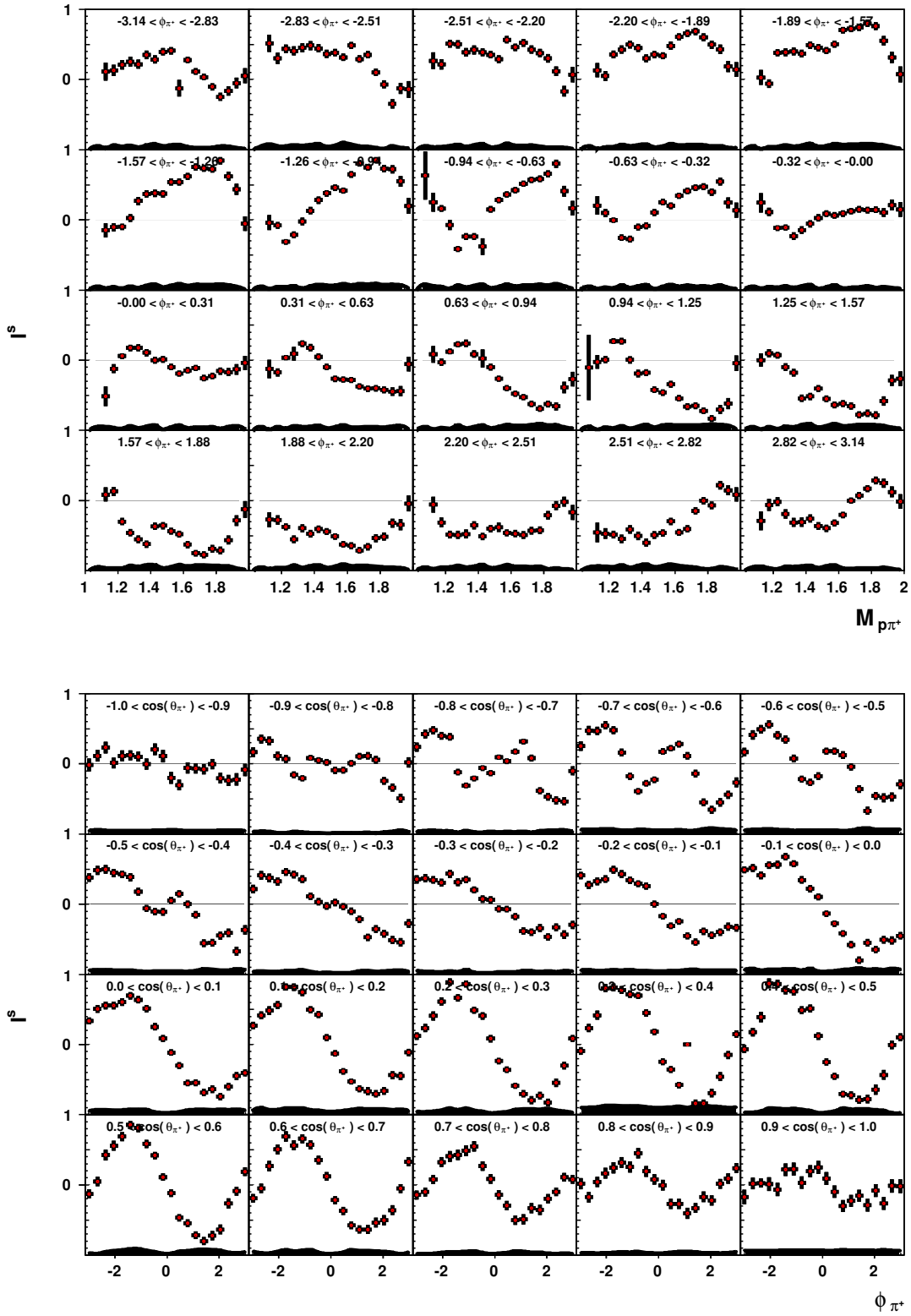

Figure 3.19: Results for the observable I^s, $E_\gamma \in [\,2.00, 2.05\,]$ GeV.

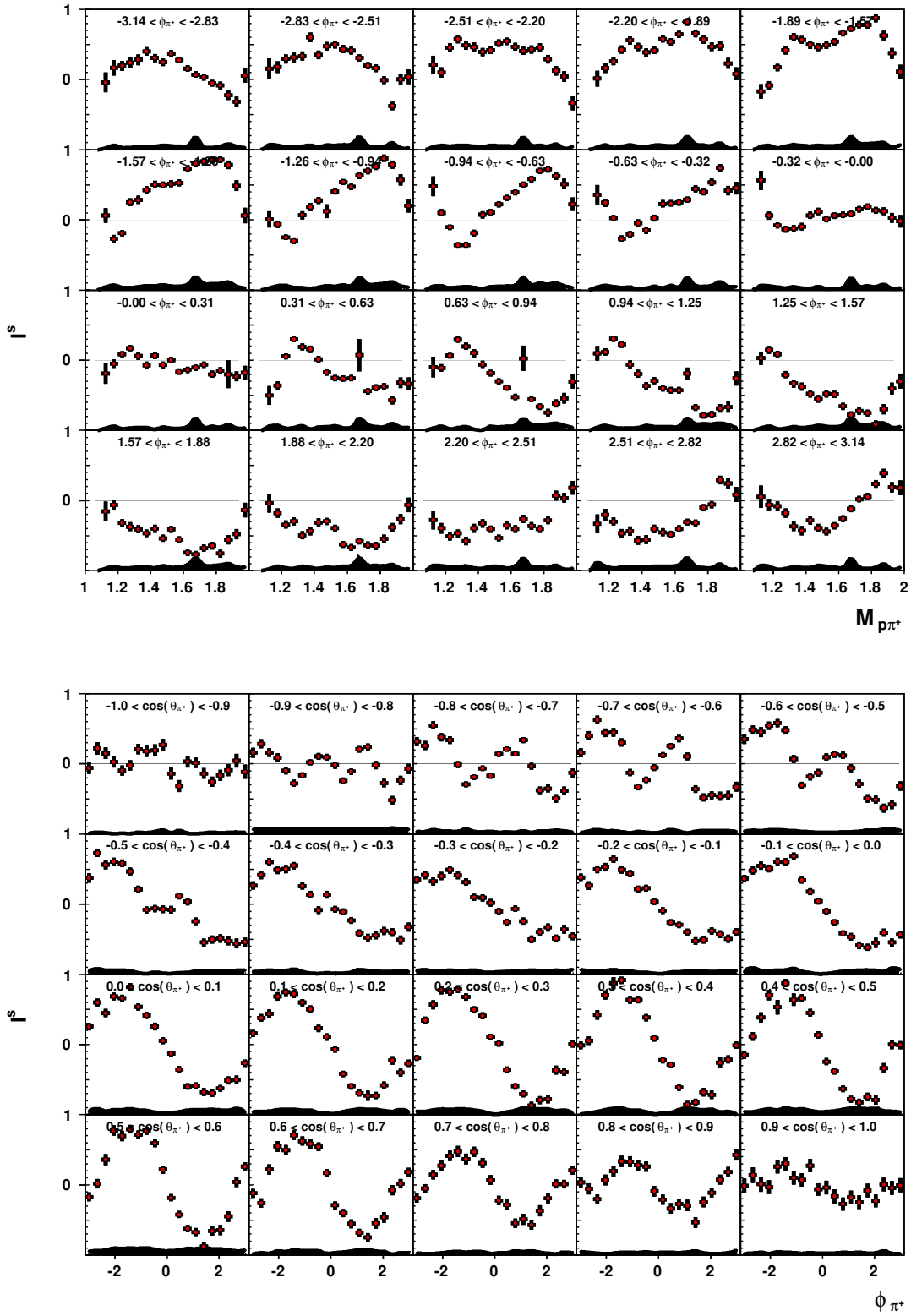

Figure 3.20: Results for the observable I^s, $E_\gamma \in [2.05, 2.10]$ GeV.

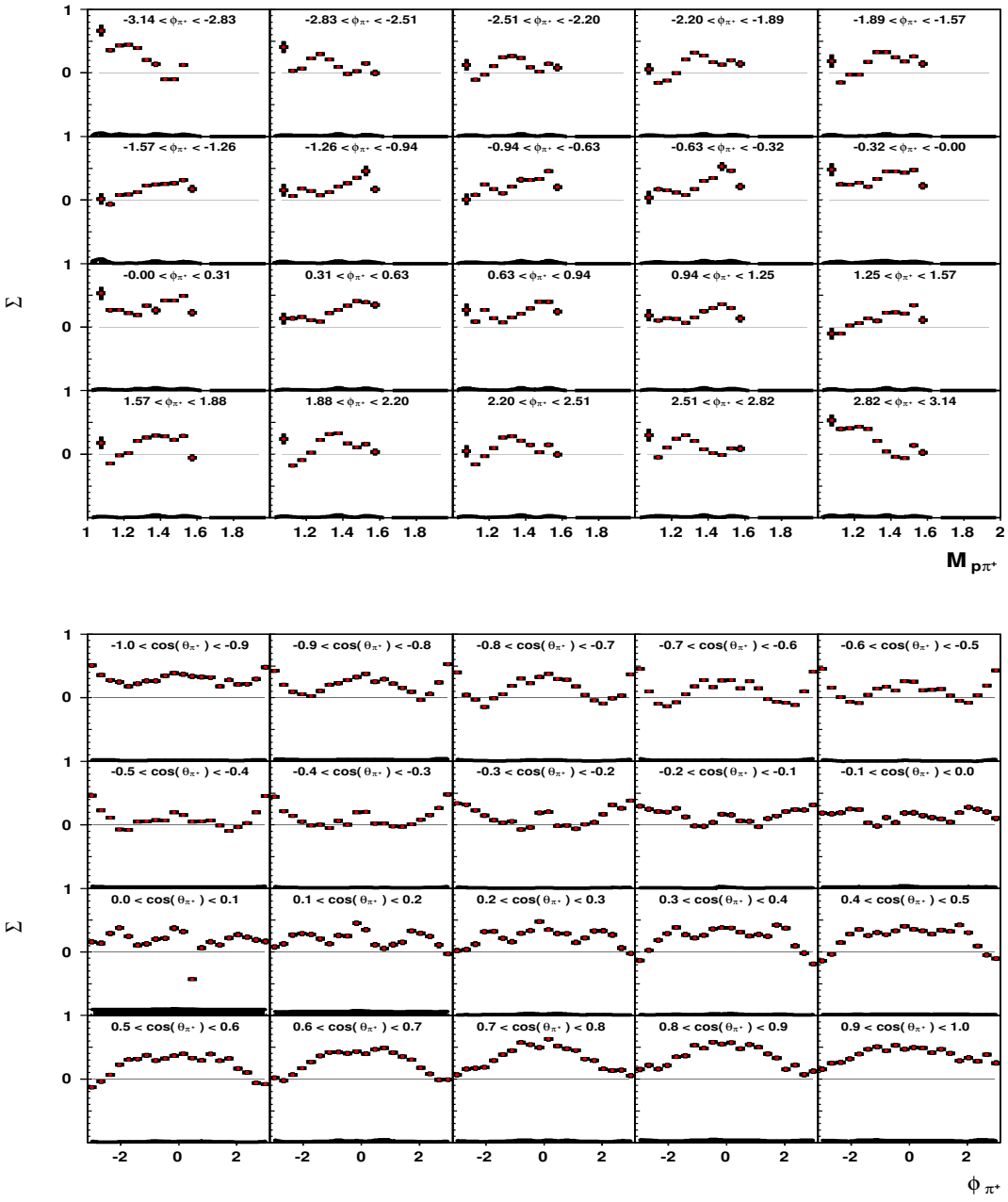

Figure 3.21: Results for the observable Σ, $E_\gamma \in [1.10, 1.15]$ GeV.

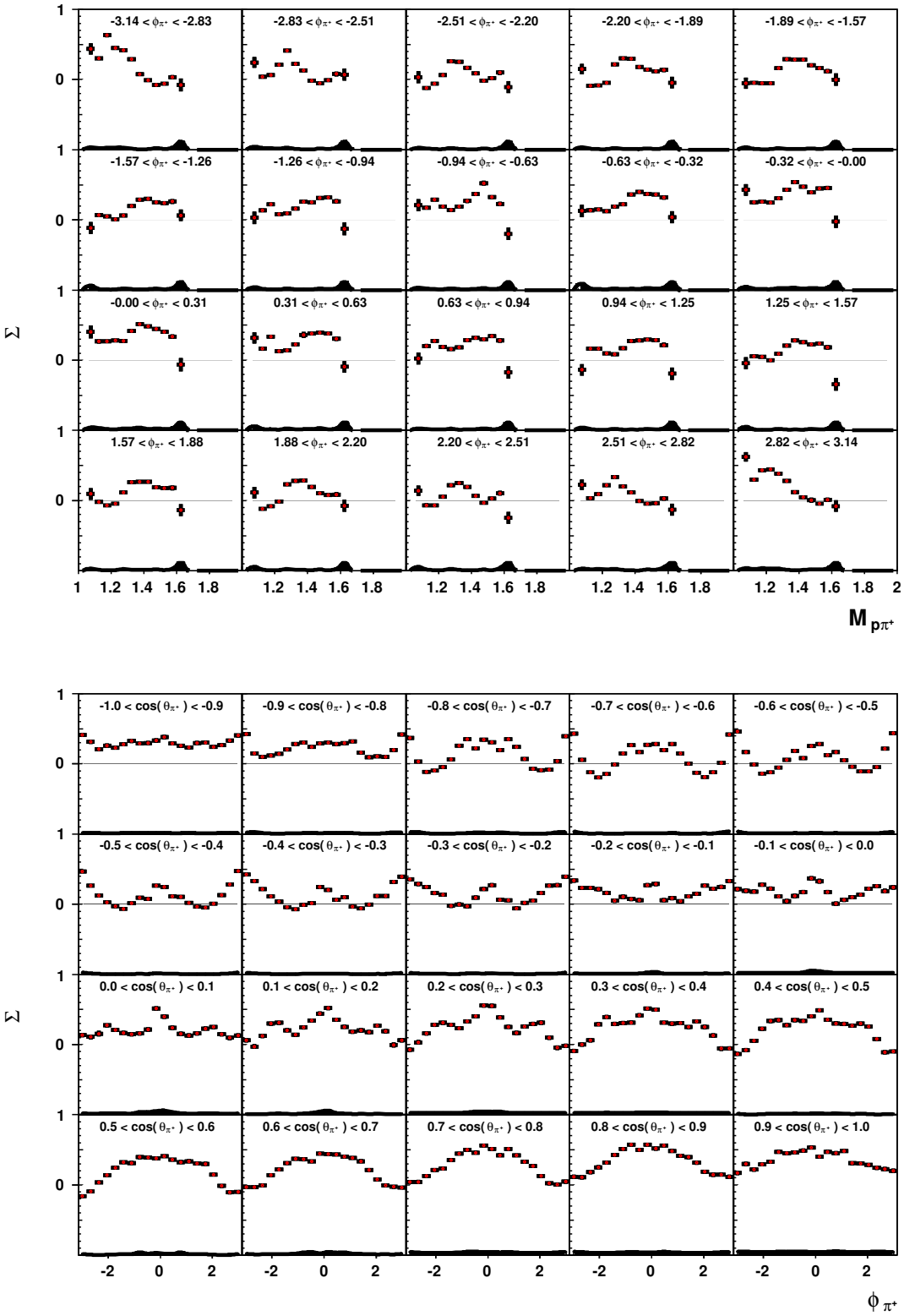

Figure 3.22: Results for the observable Σ, $E_\gamma \in [1.15, 1.20]$ GeV.

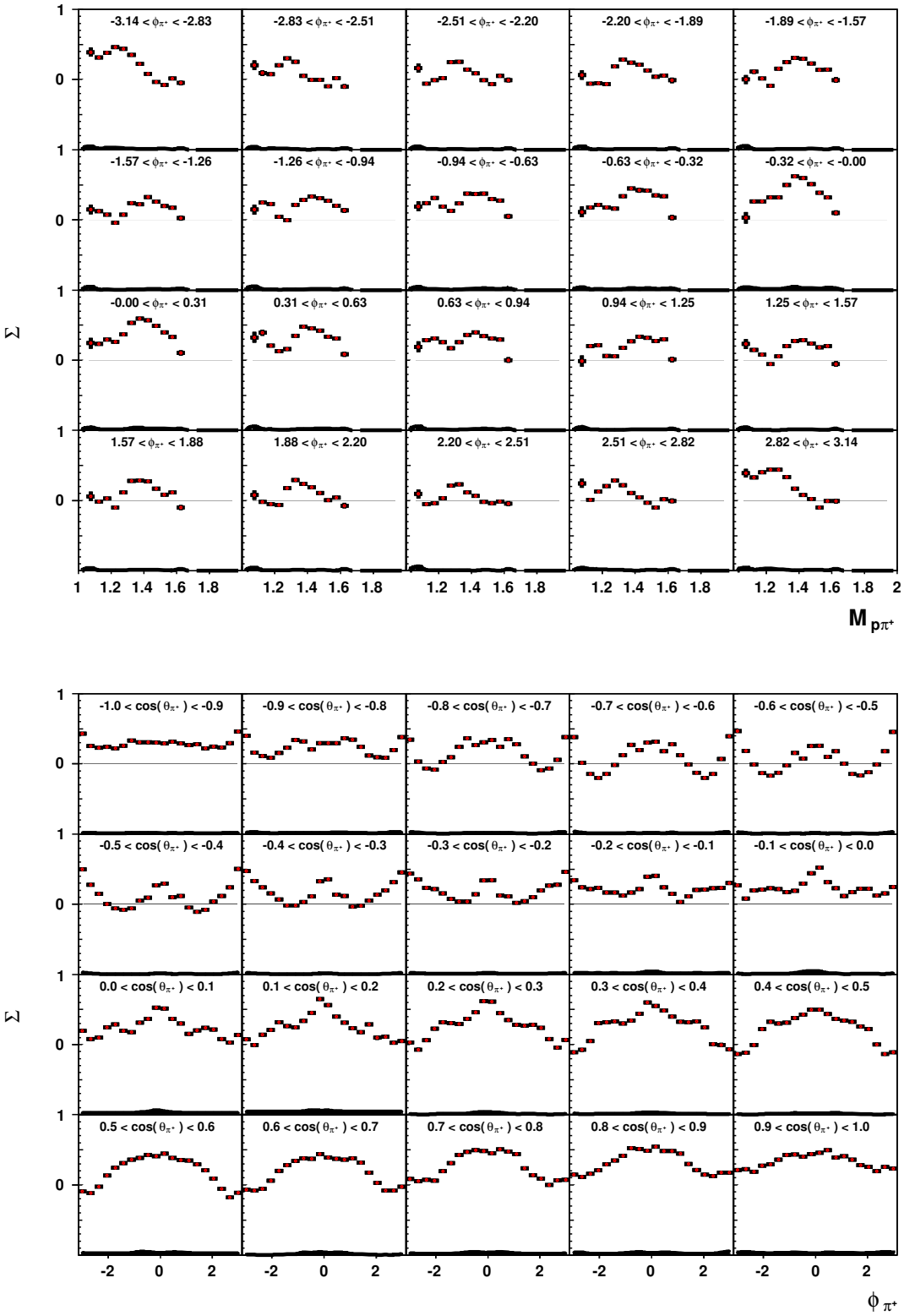

Figure 3.23: Results for the observable Σ, $E_\gamma \in [\,1.20, 1.25\,]$ GeV.

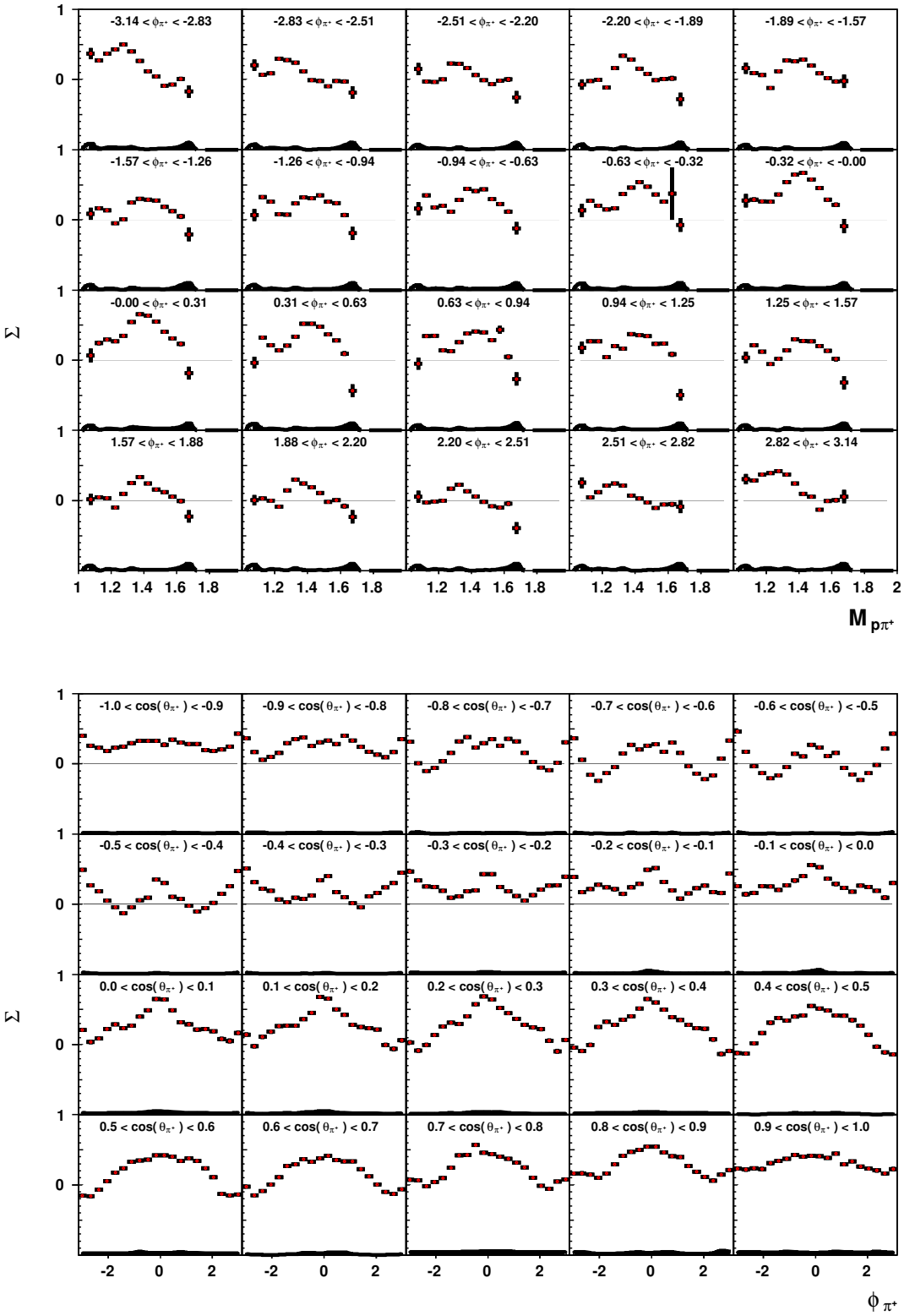

Figure 3.24: Results for the observable Σ, $E_\gamma \in [1.25, 1.30]$ GeV.

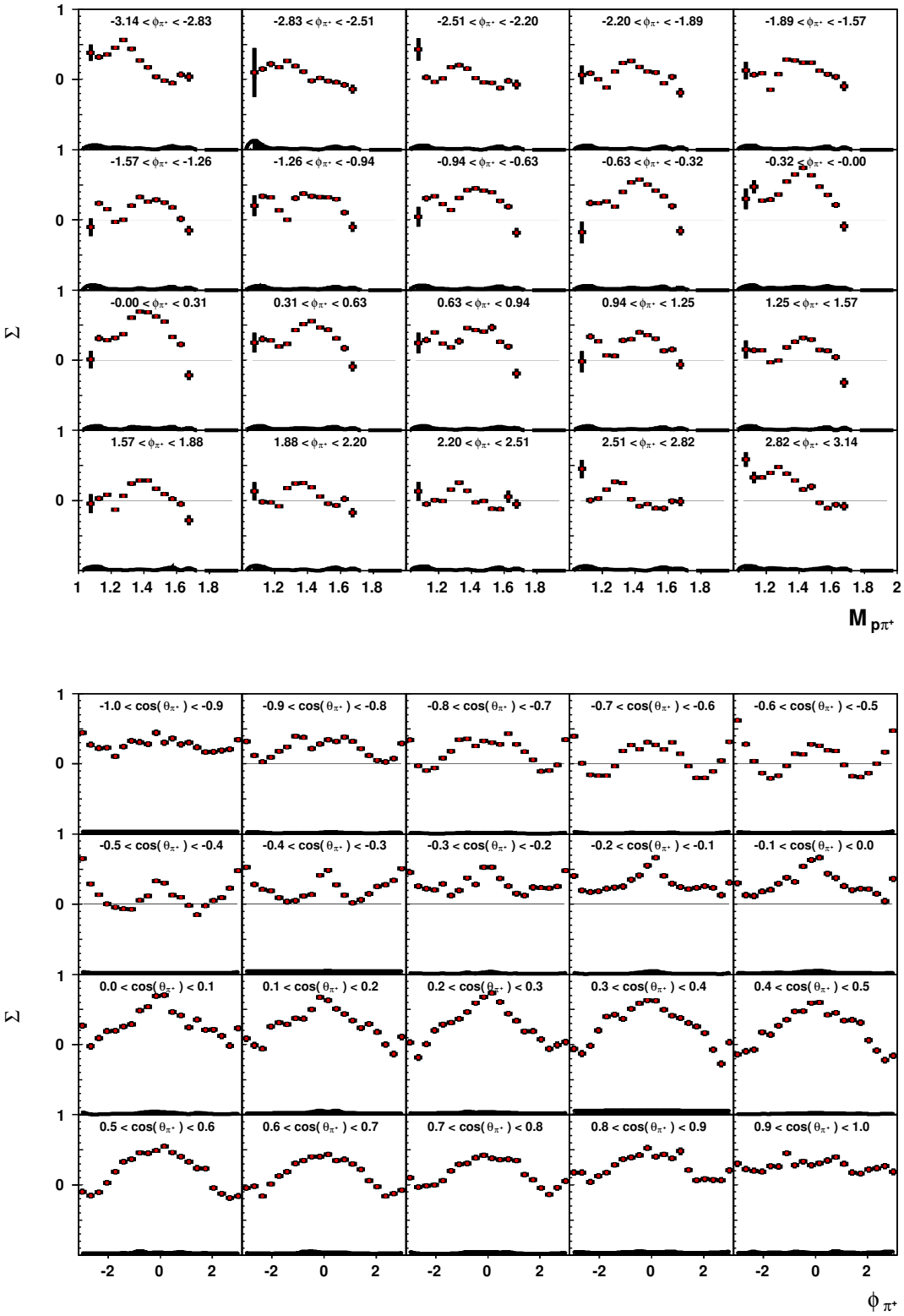

Figure 3.25: Results for the observable Σ, $E_\gamma \in [\,1.30, 1.35\,]$ GeV.

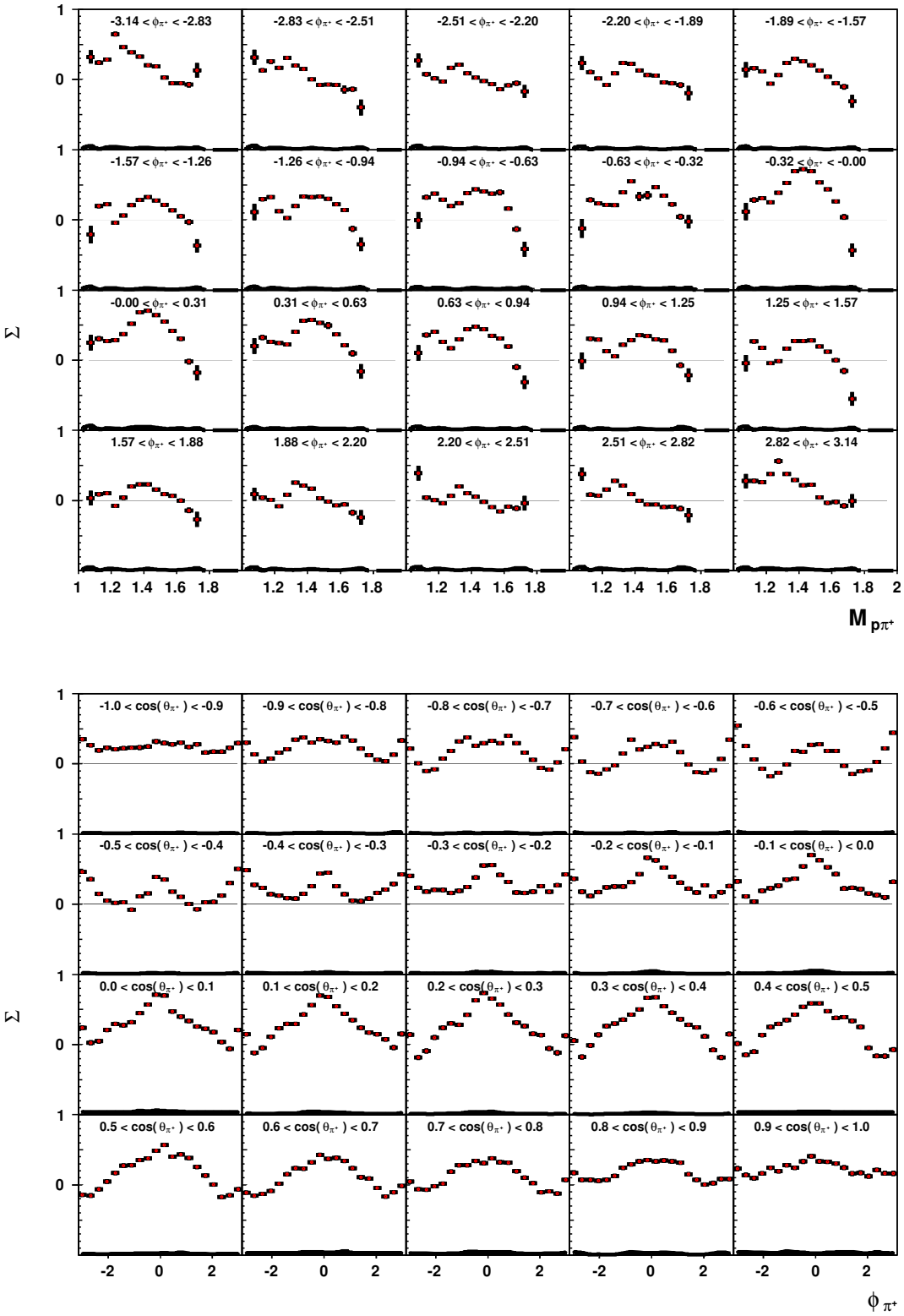

Figure 3.26: Results for the observable Σ, $E_\gamma \in [1.35, 1.40]$ GeV.

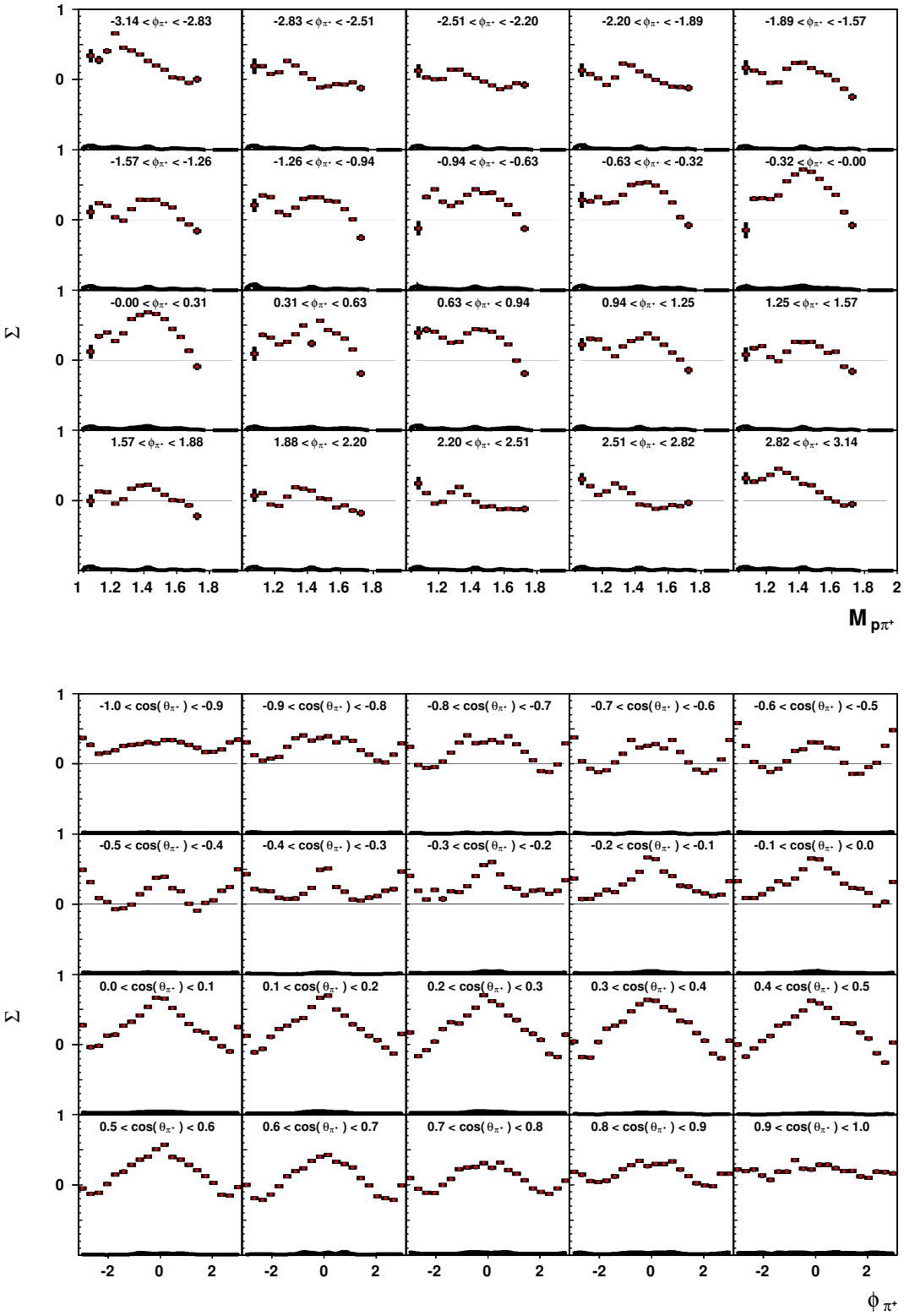

Figure 3.27: Results for the observable Σ, $E_\gamma \in [\,1.40, 1.45\,]$ GeV.

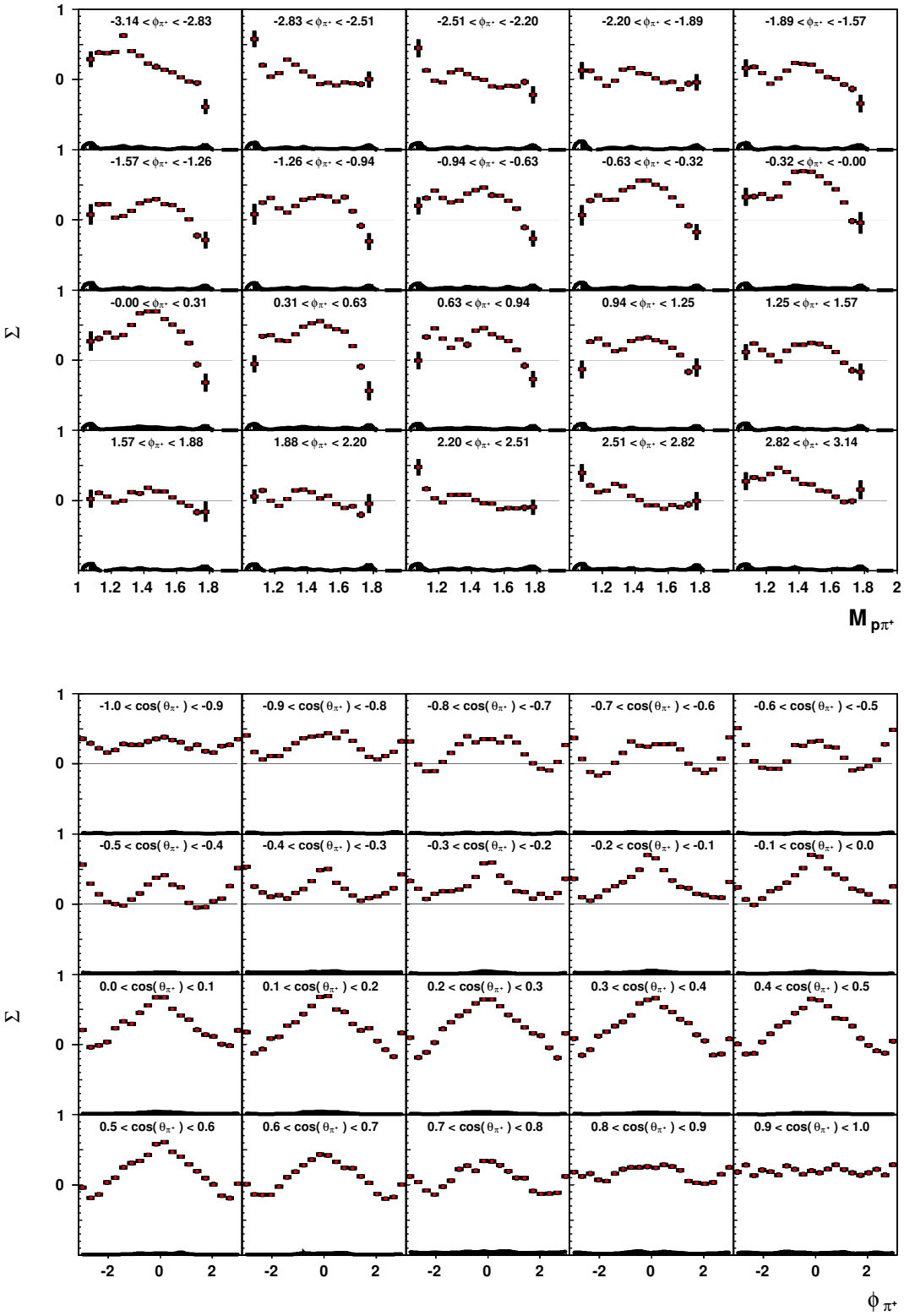

Figure 3.28: Results for the observable Σ, $E_\gamma \in [1.45, 1.50]$ GeV.

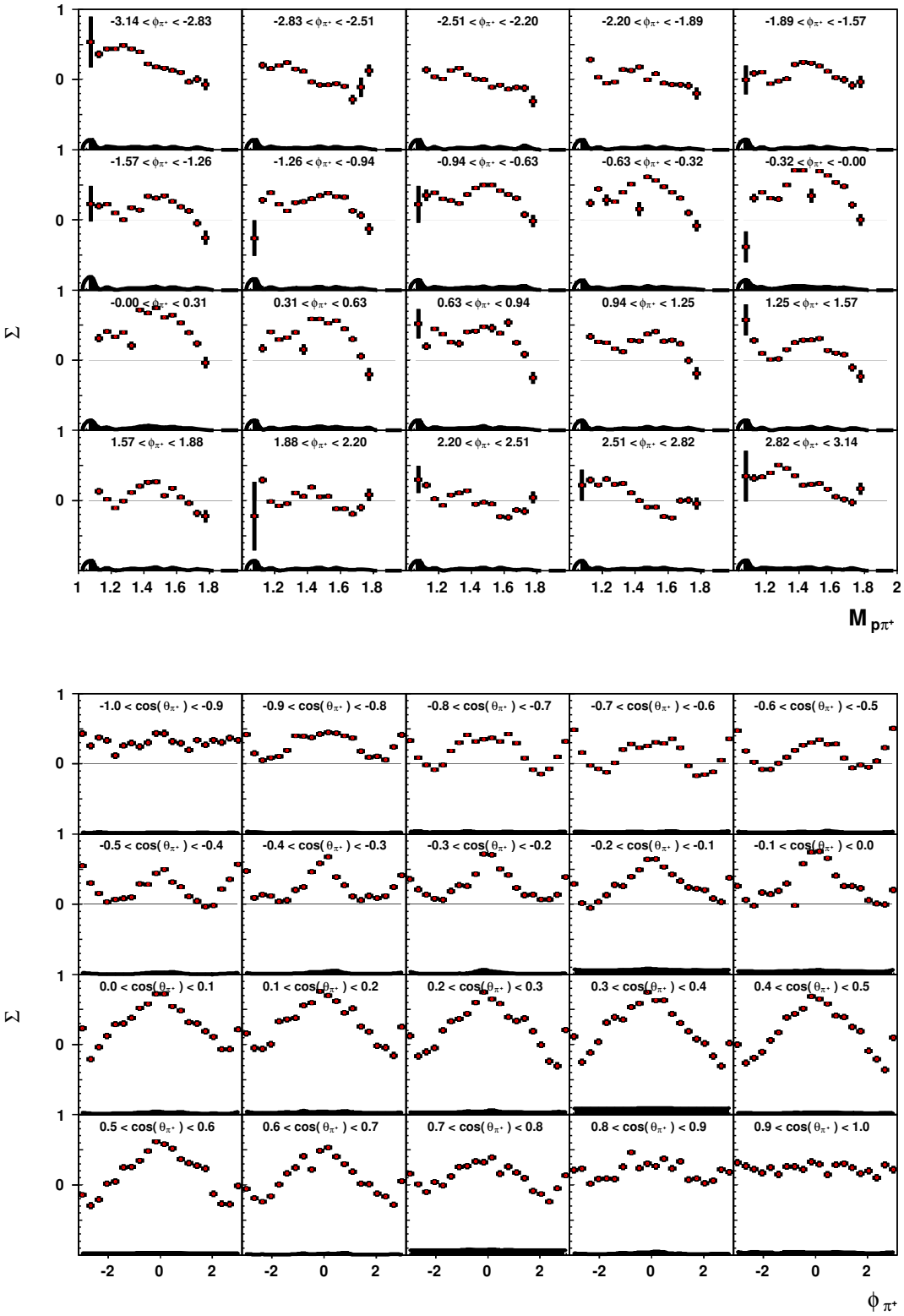

Figure 3.29: Results for the observable Σ, $E_\gamma \in [\,1.50, 1.55\,]$ GeV.

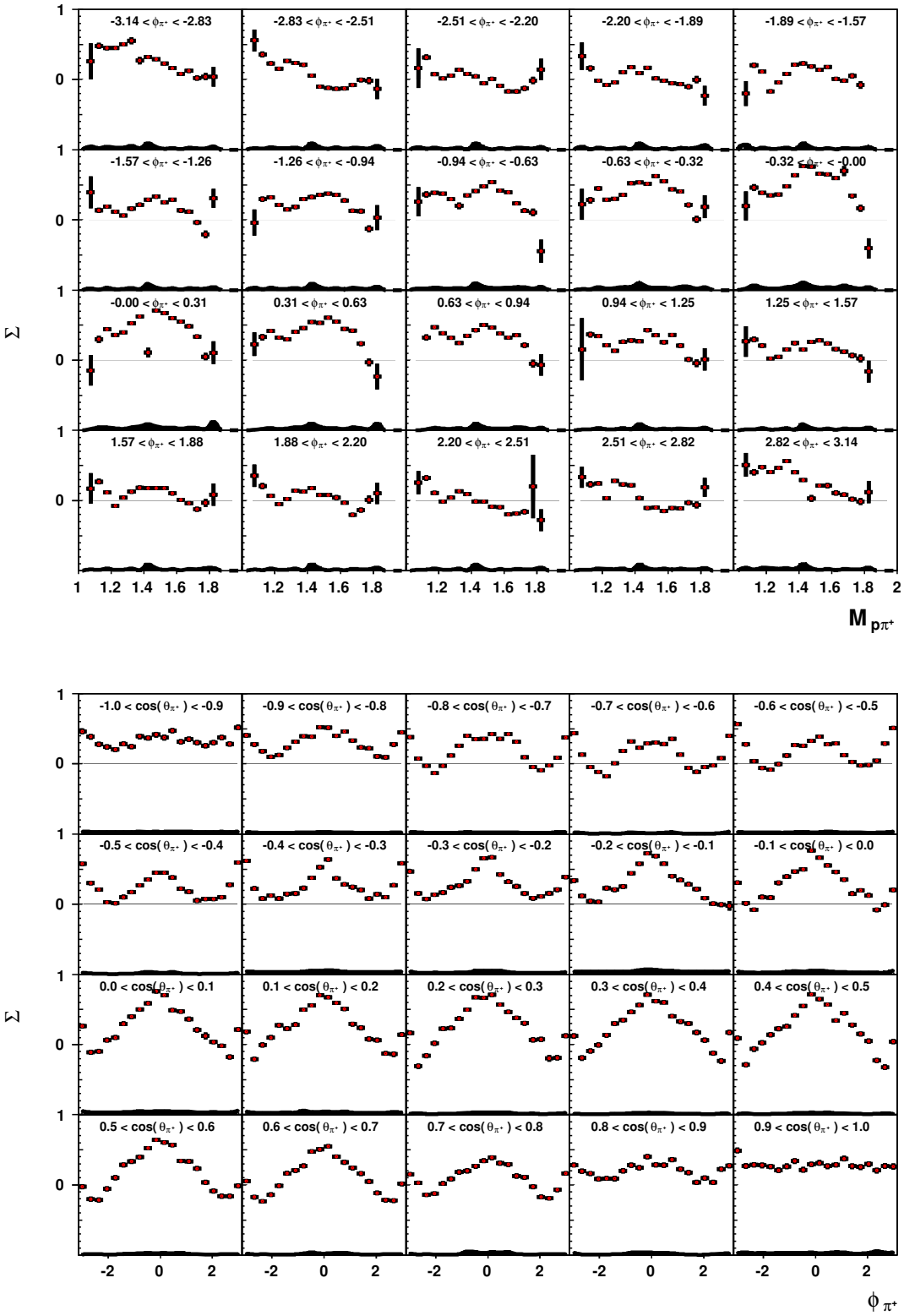

Figure 3.30: Results for the observable Σ, $E_\gamma \in [1.55, 1.60]$ GeV.

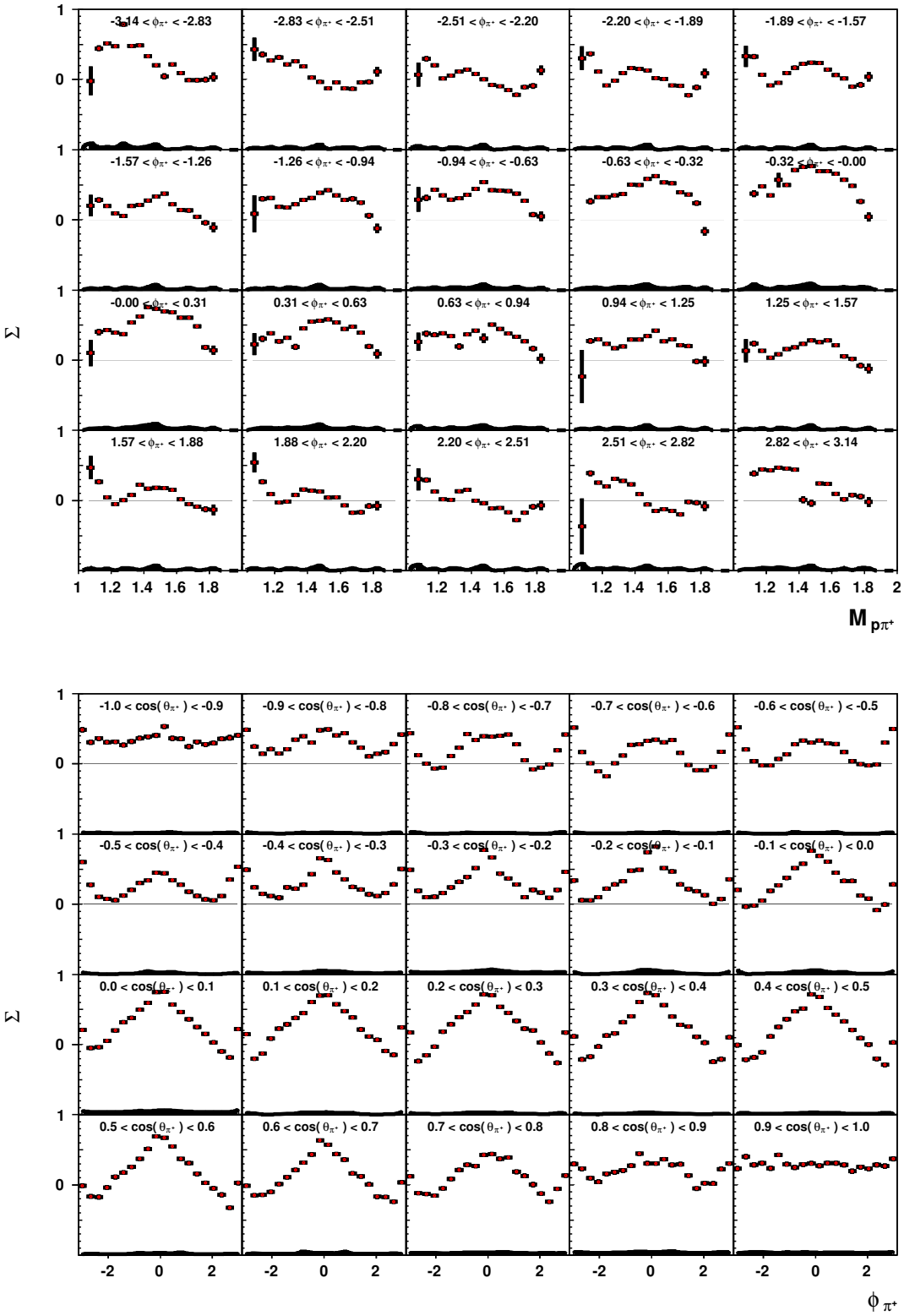

Figure 3.31: Results for the observable Σ, $E_\gamma \in [\,1.60, 1.65\,]$ GeV.

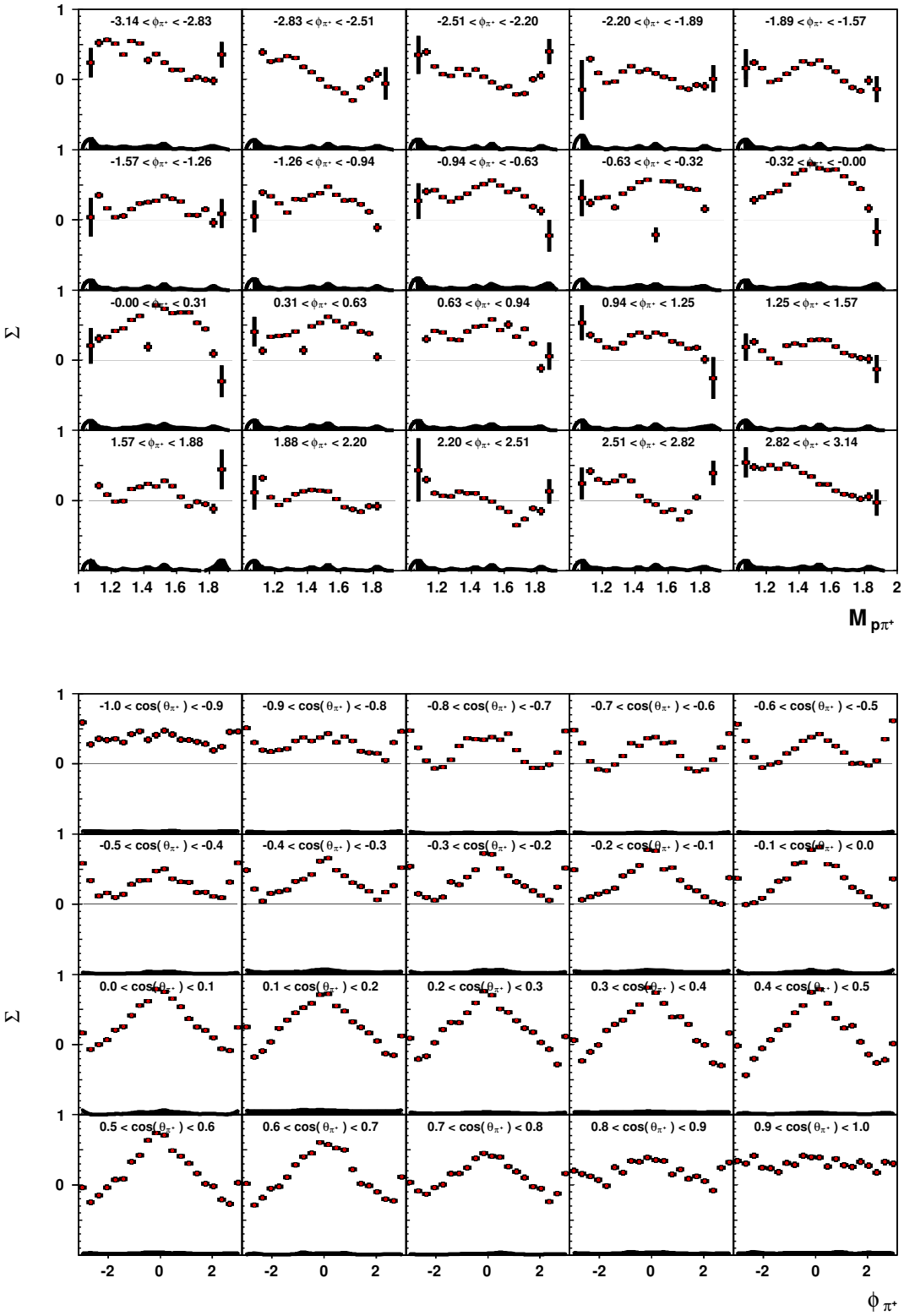

Figure 3.32: Results for the observable Σ, $E_\gamma \in [1.65, 1.70]$ GeV.

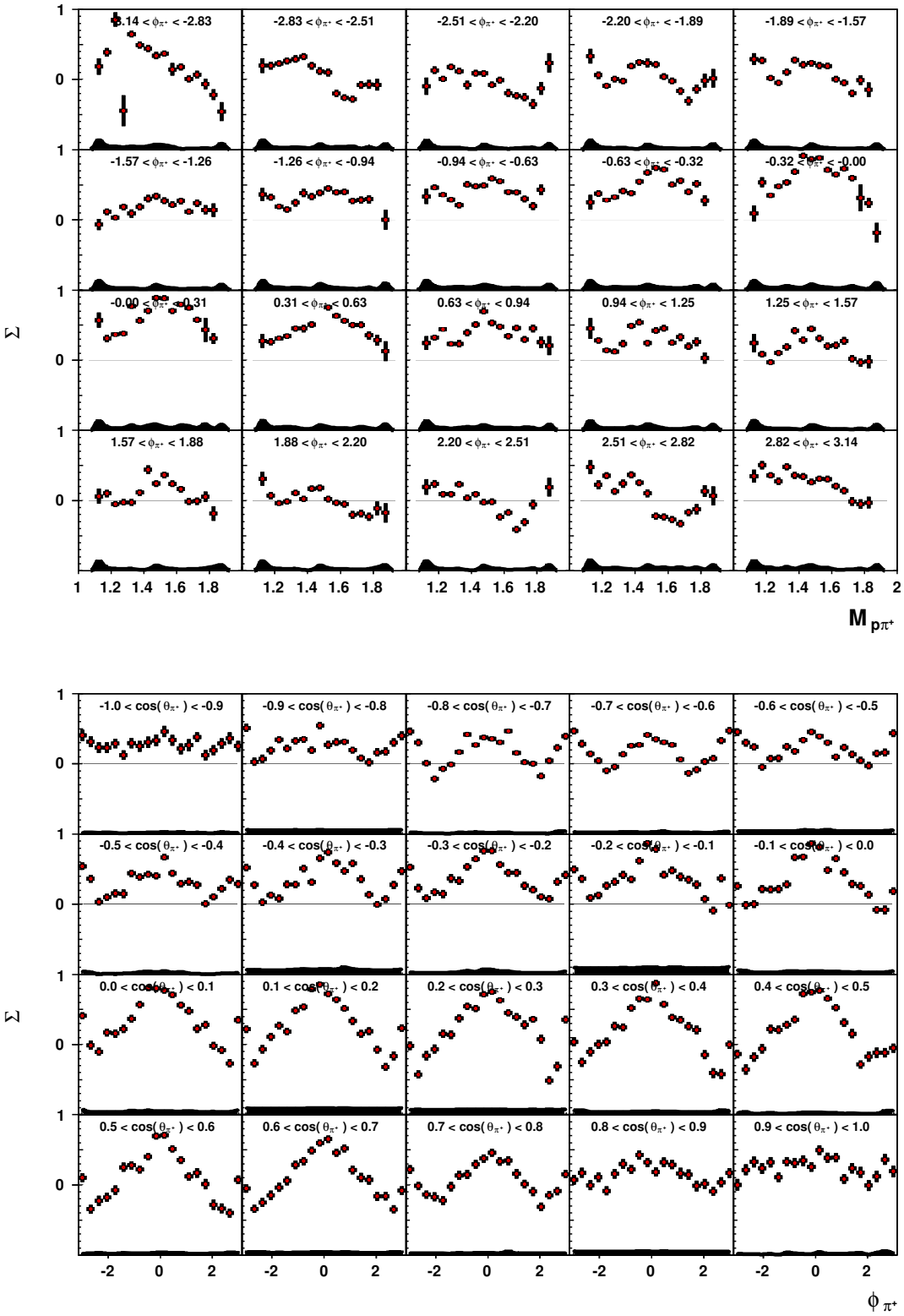

Figure 3.33: Results for the observable Σ, $E_\gamma \in [\,1.70, 1.75\,]$ GeV.

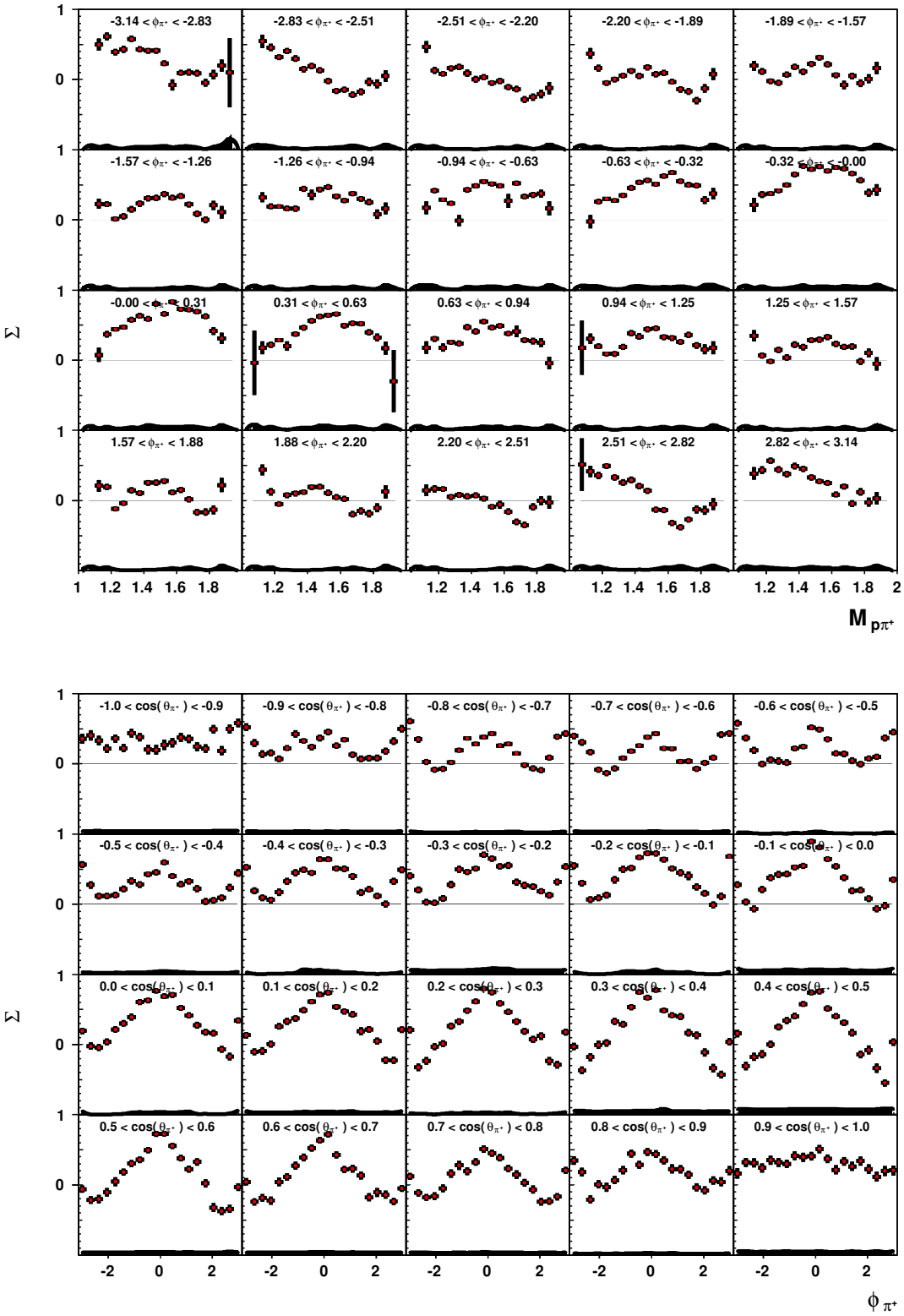

Figure 3.34: Results for the observable Σ, $E_\gamma \in [1.75, 1.80]$ GeV.

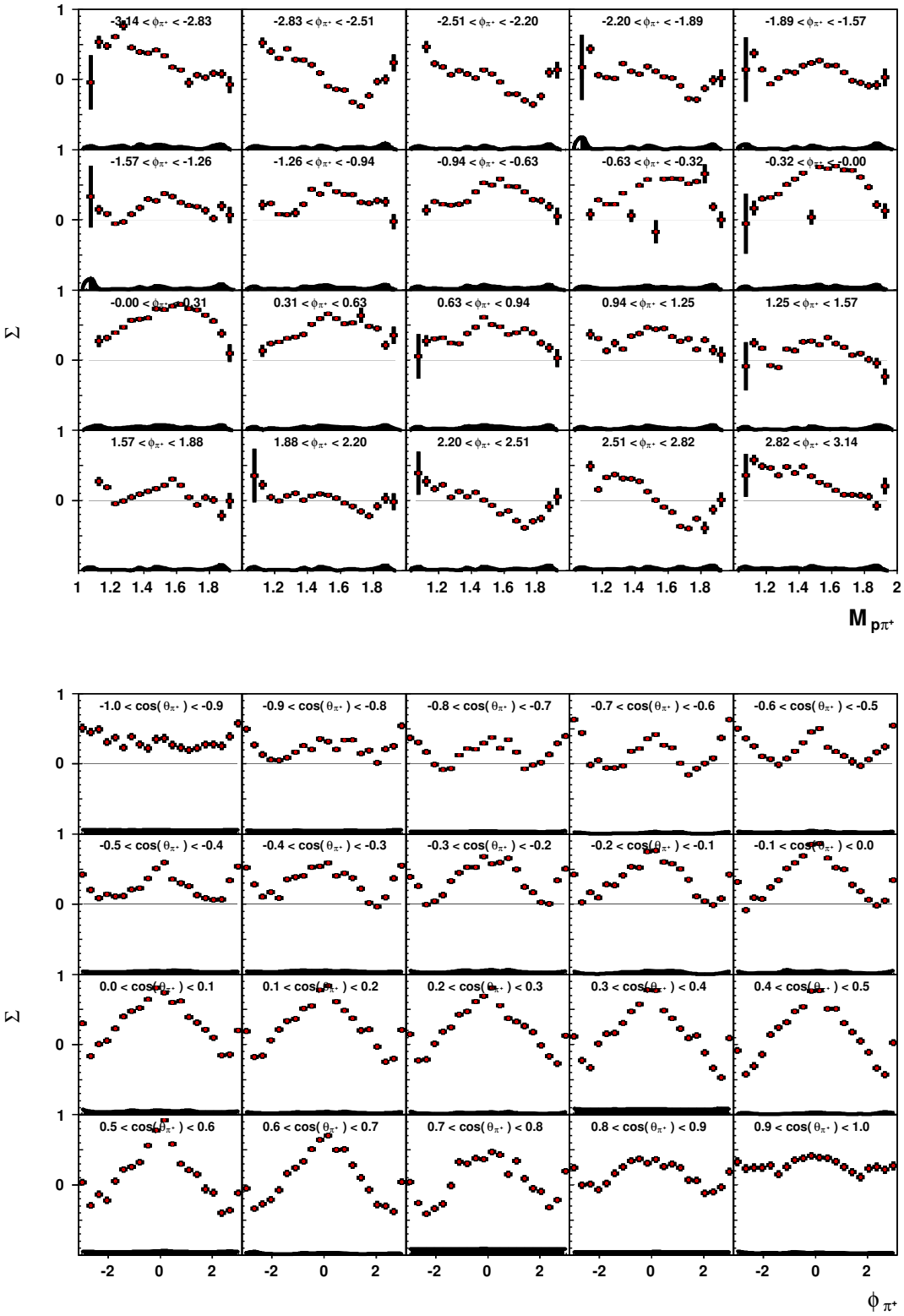

Figure 3.35: Results for the observable Σ, $E_\gamma \in [1.80, 1.85]$ GeV.

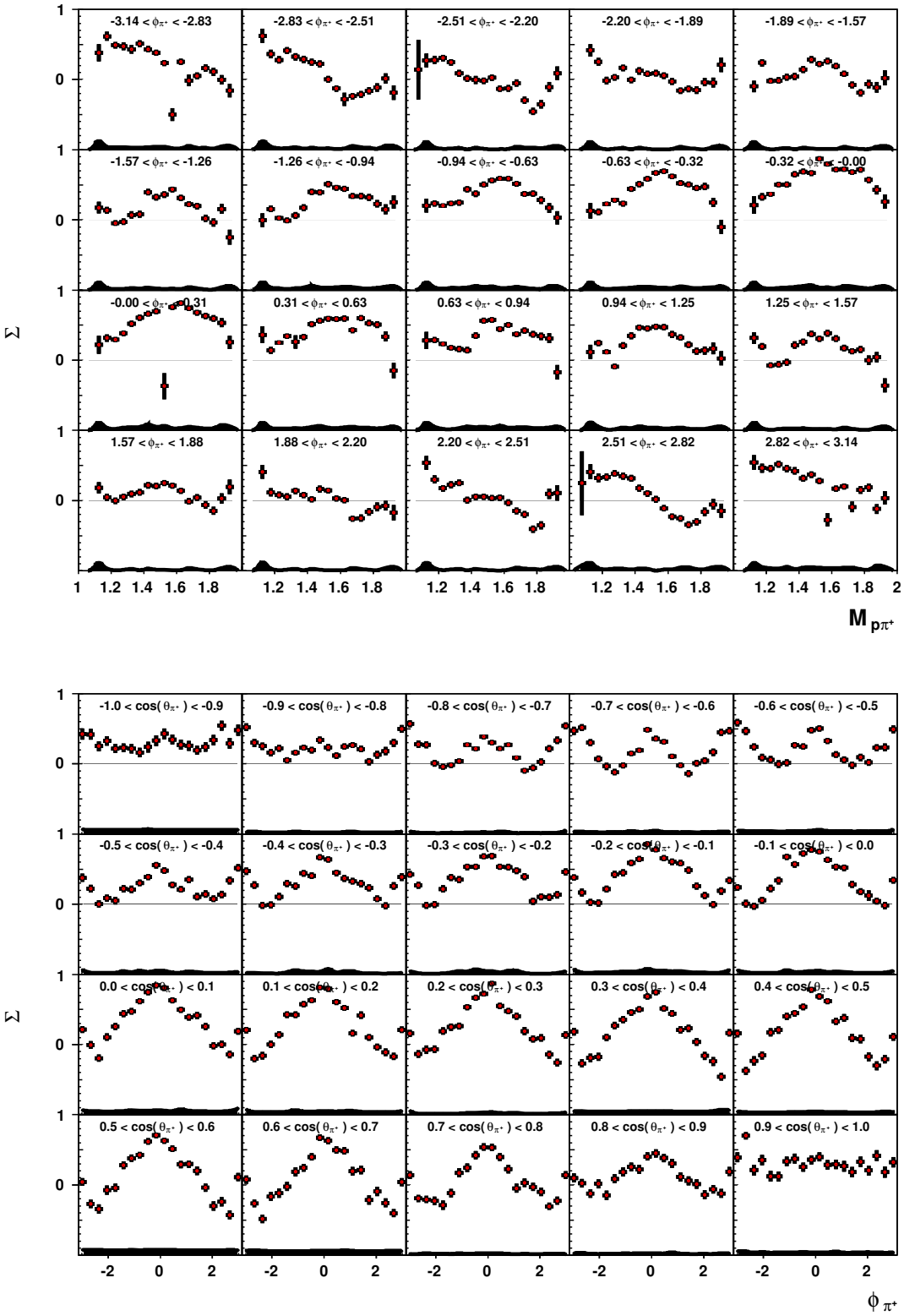

Figure 3.36: Results for the observable Σ, $E_\gamma \in [1.85, 1.90]$ GeV.

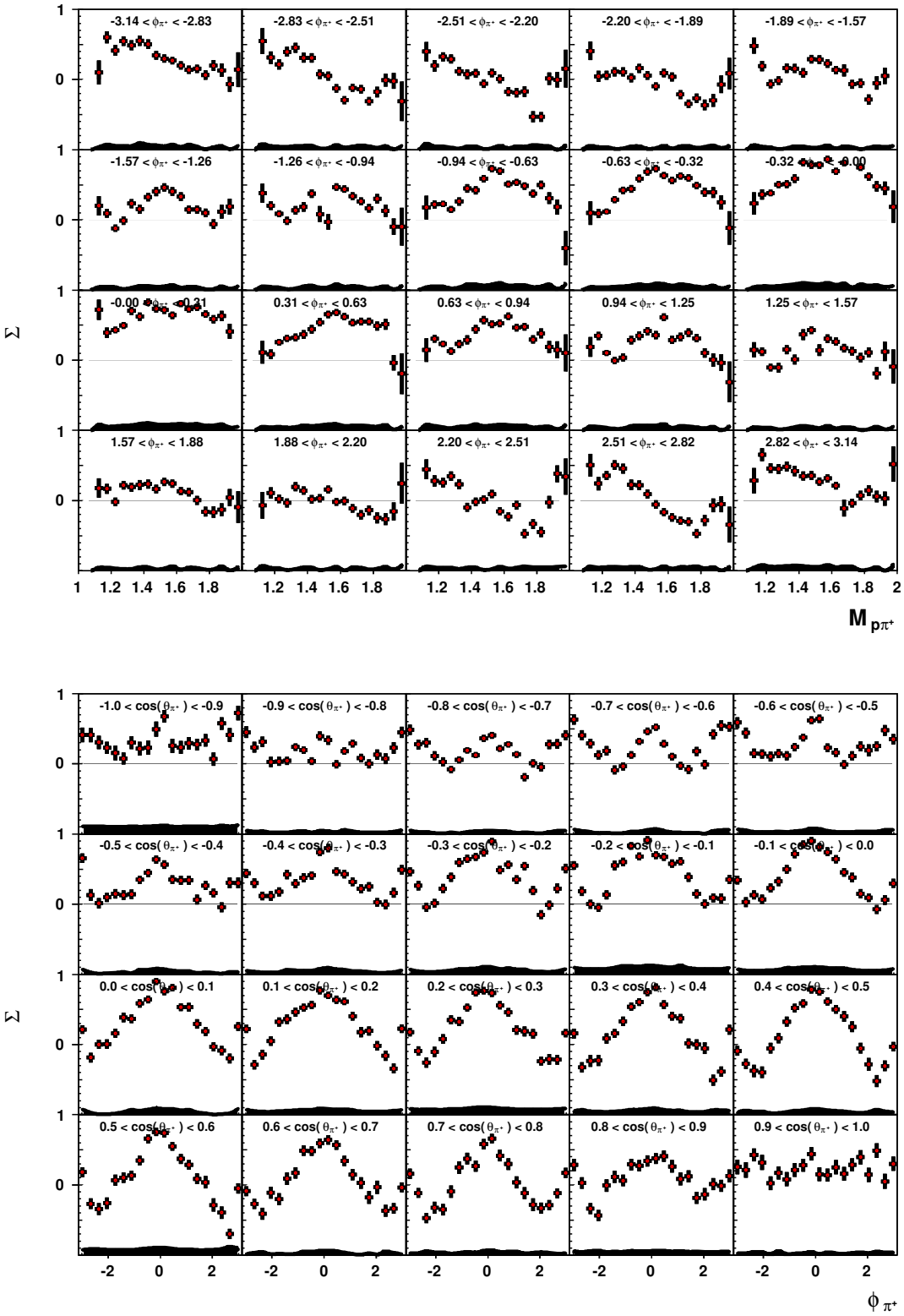

Figure 3.37: Results for the observable Σ, $E_\gamma \in [\,1.90, 1.95\,]$ GeV.

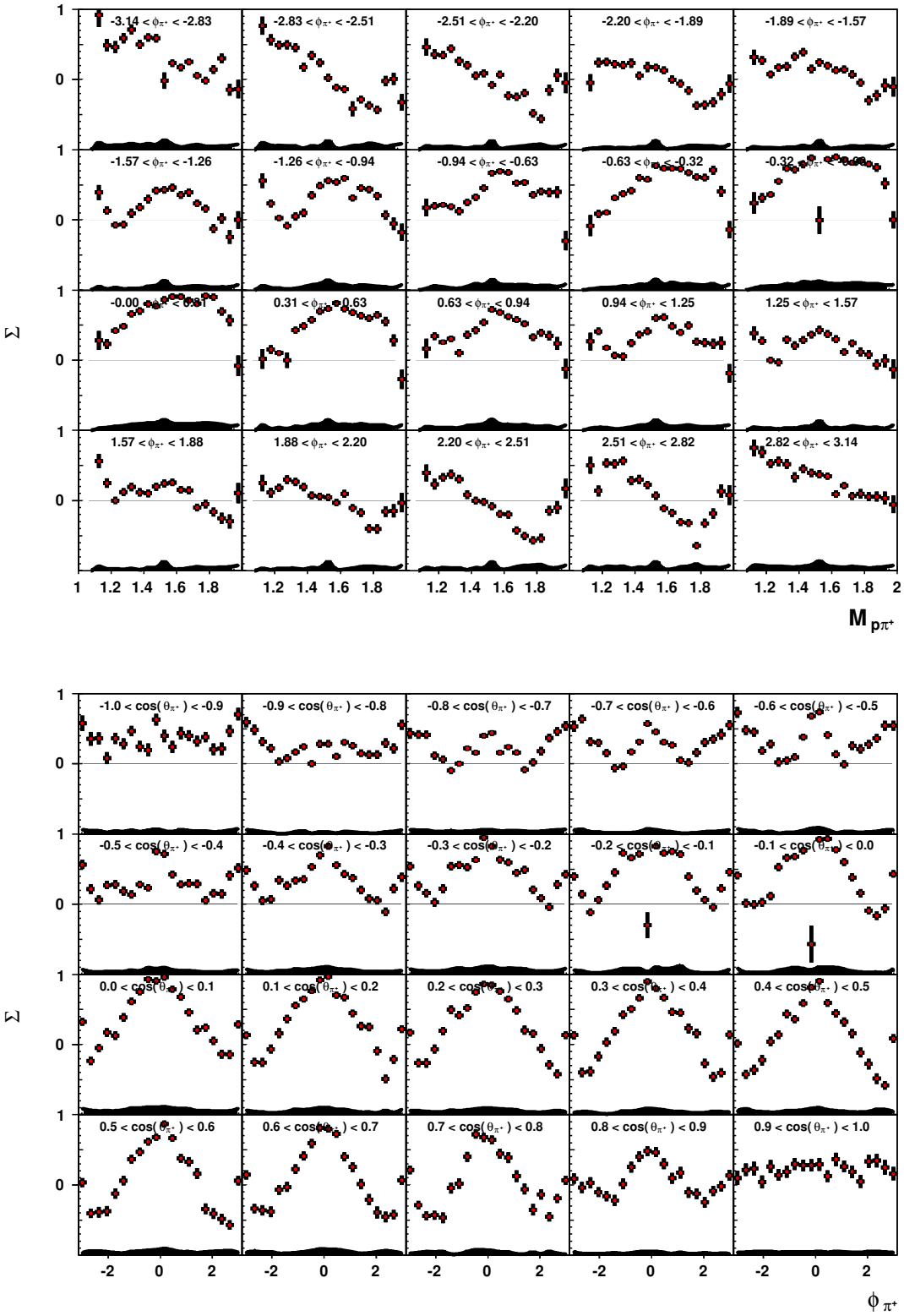

Figure 3.38: Results for the observable Σ, $E_\gamma \in [1.95, 2.00]$ GeV.

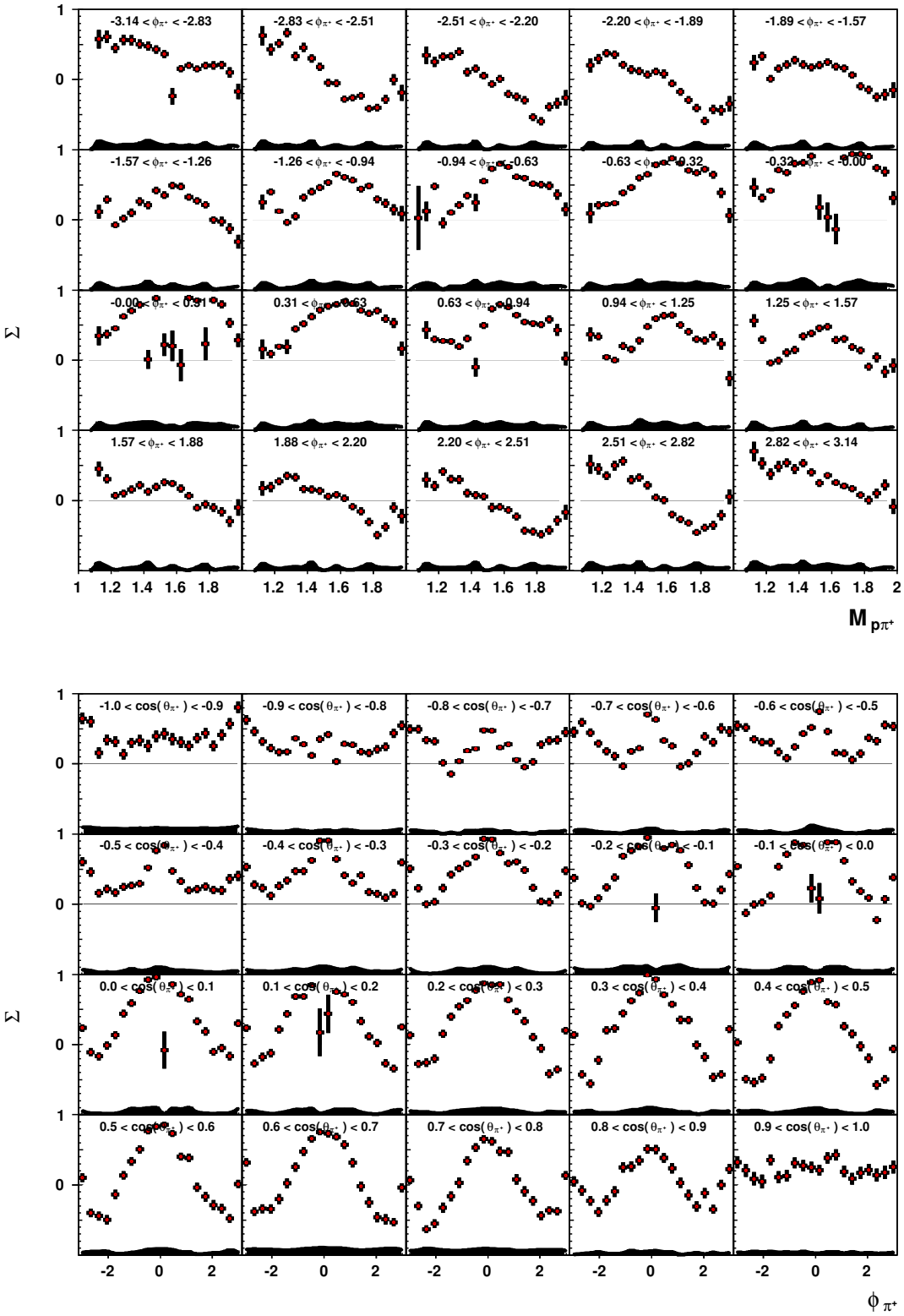

Figure 3.39: Results for the observable Σ, $E_\gamma \in [\,2.00, 2.05\,]$ GeV.

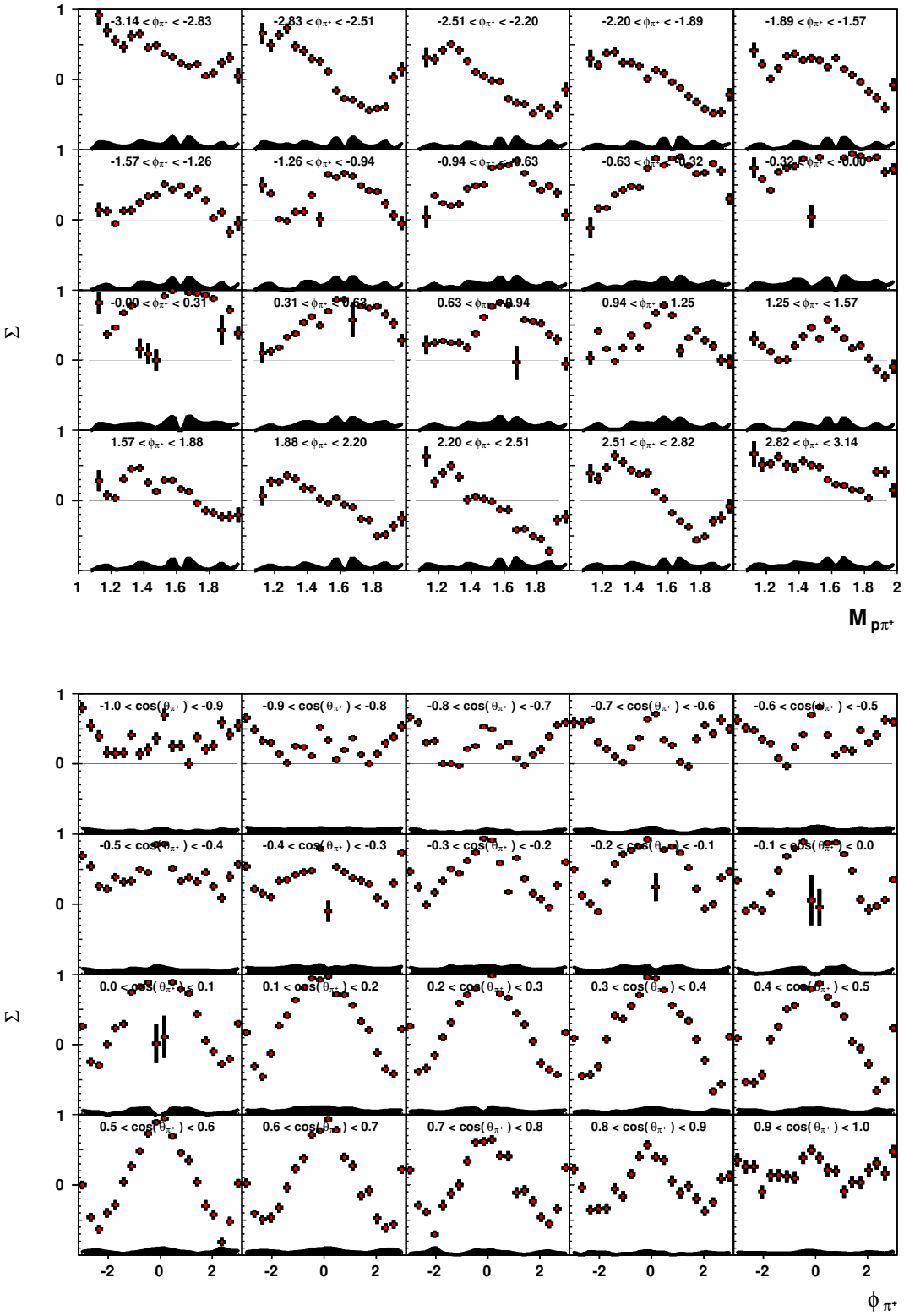

Figure 3.40: Results for the observable Σ, $E_\gamma \in [2.05, 2.10]$ GeV.

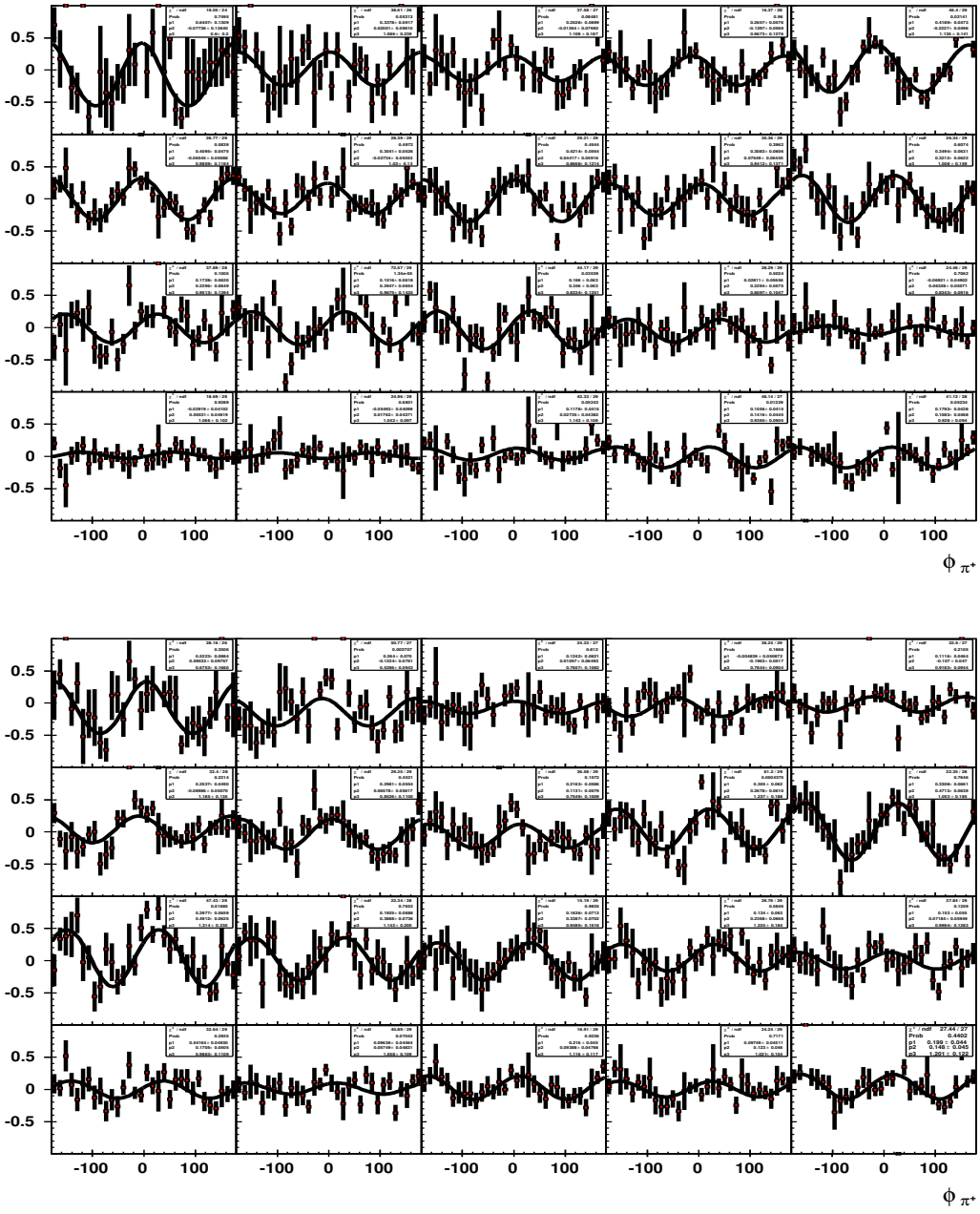

Figure 3.41: Typical β distributions (Reaction: $\gamma p \to p\pi^+\pi^-_{\text{missing}}$), $E_\gamma \in [\,1.10, 1.15\,]$ GeV: $\phi^*_{\pi^+} \in [\,-2.83, -2.51\,]$ (top), $\phi^*_{\pi^+} \in [\,-2.51, -2.20\,]$ (bottom).

BIBLIOGRAPHY

[1] U. Loring, K. Kretzschmar, B. Metsch, and H. Petry, "*Relativistic quark models of baryons with instantaneous forces*", Eur. Phys. J. **A10**, 309 (2001), hep-ph/0103287.

[2] S. Capstick and N. Isgur, "*Baryons in a Relativized Quark Model with Chromodynamics*", Phys. Rev. **D34**, 2809 (1986).

[3] S. Capstick and W. Roberts. Phys. Rev. D, 58:074011, 1998.

[4] W. Roberts and T. Oed, "*Polarization Observables for Two-Pion Production off the Nucleon*", (2004), nucl-th/0410012.

[5] E. Rutherford, Phil. Mag. **21** (1911) 669.

[6] N. Bohr, Phil. Mag. **26** (1913) 476.

[7] E. Rutherford, Phil. Mag. **37** (1919) 581.

[8] http://www.particlephysics.ac.uk/news/picture-of-the-week/picture-archive/the-pion-muon-death-cycle–a-double-anniversary.html

[9] J.E. Augustin *et al.* (1974). "*Discovery of a Narrow Resonance in e+e Annihilation*". Physical Review Letters **33**: 1406.

[10] J.J. Aubert *et al.* (1974). "*Experimental Observation of a Heavy Particle J*". Physical Review Letters **33**: 1404.

[11] Fermilab (7 August 1977). "*Discoveries at Fermilab - Discovery of the Bottom Quark*". Press release.
http://www.fnal.gov/pub/inquiring/physics/discoveries/bottom_quark_pr.html.

[12] F. Abe *et al.* (CDF Collaboration) (1995). "*Observation of Top Quark Production in pp Collisions with the Collider Detector at Fermilab*". Physical Review Letters **74**: 26262631.

[13] http://www.physics.fsu.edu/users/roberts/roberts_color_tech.html

[14] S. Bethke, Prog. Part. Nucl. Phys. **58**, 351 (2007).

[15] F. X. Lee *et al.* "*Excited baryons from Bayesian priors and overlap fermions*", hep-lat/0208070, 2002.

[16] J. Bulava *et al.* "Nucleon, Δ, and Ω excited state spectra in N_f=2+1 lattice QCD" Phys. Rev. D **82**, 014507 (2010).

[17] http://cerncourier.com/cws/article/cern/29524

[18] http://en.wikipedia.org/wiki/Cubical_atom.

[19] http://en.wikipedia.org/wiki/Plum_pudding_model.

[20] http://en.wikipedia.org/wiki/Hantaro_Nagaoka.

[21] A. de Rujula *et al.* "*Hadron masses in a gauge theory*", Phys. Rev. D 12, 147 (1975).

[22] L. Glozman and D. Riska, "*The Spectrum of the nucleons and the strange hyperons and chiral dynamics*", Phys. Rept. **268**, 263 (1996), hep-ph/9505422.

[23] K. Nakamura *et al.* (Particle Data Group), J. Phys. G 37, 075021 (2010).

[24] D.B. Lichtenberg *et al.* "*Quark-Diquark Model of Baryons and SU(6)*", Phys. Rev. 167, 1535, 1968.

[25] http://adsabs.harvard.edu/abs/1983PhDT.....98H

[26] E. Klempt "Baryon Spectroscopy and the Origin of Mass", Hadron 2009, arXiv:1001.3290v1.

[27] K. Glander *et al.*, [SAPHIR Collaboration], "*Measurement of* $\gamma p \to K^+\Lambda$ *and* $\gamma\ p \to K^+\Sigma^0$ *at photon energies up to 2.6 GeV*", Eur. Phys. J. A19, 251 (2004), nuclex/0308025.

[28] J. W. C. McNabb *et al.*, [CLAS Collaboration], "*Hyperon Photoproduction in the Nucleon Resonance Region*", Phys. Rev. C69, 042201 (2004), nucl-ex/0305028.

[29] N. Sparks, [CBELSA-TAPS Collaboration], "*Beam asymmetries in pi0 photoproduction on the proton*", AIP Conf. Proc. **1257**, 591 (2010).

[30] W. Roberts and A. Rakatovao, "*A model for two-pion photoproduction amplitudes*", (1997), hep-ph/9708236.

[31] M. Bellis *et al.*, "*Measurement of* $\pi^+\pi^-$ *Photoproduction in Double-Polarization Experiments using CLAS*". CLAS Analysis Proposal E-06-013.

[32] O. Krehl, C. Hanhart, S. Krewald, and J. Speth, "*What is the structure of the Roper resonance?*", Phys. Rev. **C62**, 025207 (2000), nucl-th/9911080.

[33] Z.-p. Li, V. Burkert, and Z.-j. Li, "*Electroproduction of the Roper resonance as a hybrid state*", Phys. Rev. **D46**, 70 (1992).

[34] Volker D. Burkert, Inna Aznauryan1, and the CLAS Collaboration, "*New Results on Nucleon Resonance Transition Form Factors*", arXiv:0908.3507v1 [nucl-ex] 24 Aug 2009.

[35] J. Gomez Tejedor and E. Oset, "*Double pion photoproduction on the nucleon: Study of the isospin channels*", Nucl. Phys. **A600**, 413 (1996), hep-ph/9506209.

[36] L. Murphy and J. Laget, 1996, "DAPHNIA/SPhN 96-10".

[37] V. Mokeev, *et al.*, "*Electroexcitation of nucleon resonances at Q^2=0.65(GeV/c^2 from a combined analysis of single- and double-pion electroproduction data*", Phys. Rev. C 72, 045201 (2005).

[38] V.A. Nikonov, *et al.*, "*Further evidence for N(1900)P_{13} from photoproduction of hyperons*", Phy. Lett. B Volume 662, Issue 3, 24 April 2008, Pages 245-251.

[39] S. Strauch, "*Beam-Helicity Asymmetries in Double-Charged-Pion Photoproduction on the Proton*", Phys. Rev. Lett. 95, 162003 (2005).

[40] Y. Assafiri *et al.* "*Double π^0 Photoproduction on the Proton at GRAAL*". Phys. Rev. Lett. 90 (2003), p. 222001.

[41] J. Ajaka *et al.* "*Double π^0 photoproduction on the neutron at GRAAL*". Phys Lett B, Volume 651, Issues 2-3, 26 July 2007, Pages 108-113.

[42] E. Gutz. *et al.* "*Photoproduction of meson pairs: First measurement of the polarization observable I^s*". Phys. Lett. B687:11-15, 2010.

[43] B. Mecking. "*The CEBAF large acceptance spectrometer (CLAS)*". Nucl. Instr. and Meth. A503/03, 513, 2003.

[44] http://www.jlab.org/visitors/science/unique.html.

[45] M. Crofford *et al.* "*The RF System for the CEBAF Polarized Photoinjector*". Technical Report, Thomas Jefferson National Accelerator Facility, 1993.

[46] D.I. Sober *et al.* "*The bremsstrahlung tagged photon beam in Hall B at JLab*". Nucl Instr. Meth. A440, 263 (2000).

[47] U. Timm. "*Coherent bremsstrahlung of electrons in crystals*". Fortschritte der Physik, 1969.

[48] L. Montanet *et al.* Phys. Rev. **D50** 1173, 1994.

[49] W.J Briscoe *et al.* NSF Major Research Instrumentation, NSF Award 9724489. Technical report.

[50] Y.G. Sharabian *et al.* "*A new highly segmented start counter for the CLAS detector*". Nucl. Phys. A 556, 246 (2006).

[51] M.D. Mestayer. "*The CLAS Drift Chamber System*". Nucl. Instr. and Meth. A449, 81, 200.

[52] E.S. Smith *et al.* "*The time-of-fight system for CLAS*". Nucl Inst Meth A 432, 265-298, 1999.

[53] E. Pasyuk. "*Energy loss corrections for charged particles in CLAS*". CLAS-Note 2007-016. https://misportal.jlab.org/ul/physics/Hall-B/clas/viewFile.cfm/2007-016.pdf?documentId=423.

[54] M. Williams. "*Measurement of Differential Cross Sections and Spin Density Matrix Elements along with a Partial Wave Analysis for $\gamma p \to p\omega$ using CLAS at Jefferson Lab*". Doctoral Thesis, Carnegie Mellon University.

[55] S. Stepanyan *et al.* "*Energy calibration of the JLab bremsstrahlung tagging system*". Nucl Inst Meth A **572**, 654 (2007).

[56] M. Dugger, C. Hanretty. "*Correction to the incident photon energy for g8b data*". CLAS-Note 2009-030. https://misportal.jlab.org/ul/physics/Hall-B/clas/viewFile.cfm/2009-030.pdf?documentId=605.

[57] M. Battaglieri, *Private communication.*

[58] K. Livingston. "*Binned fitting techniques for measuring photon beam asymmetry*". CLAS-Note 2012-010. http://nuclear.gla.ac.uk/~kl/g8b/linpol/extracting_sigma.pdf

[59] http://root.cern.ch/root/htmldoc/TH1.html#TH1:KolmogorovTest

[60] A. Natter. Analytic bremsstrahlung code. http://www.pit.physik.uni.tuebingen.de/bremsanalytic.html.

[61] C.I.O. Gordon. "*Rho photoproduction using linearly polarized photons with the CLAS detector*". PhD thesis, Glasgow University, 2004.

[62] https://clasweb.jlab.org/rungroups/g8/wiki/index.php/CLAS_notes_and_Supporting_Documents

[63] M. Dugger, B. Ritchie. "*Consistency corrections to the linear photon polarization for g8b data*". CLAS-Note 2012-002. https://misportal.jlab.org/ul/Physics/Hall-B/clas/viewFile.cfm/2012-002.pdf?documentId=668.

[64] http://www.physics.fsu.edu/users/roberts/roberts_polarization.html.

[65] W. Roberts, *Private Communication* (2010).

[66] C. Keith. "*The JLab Frozen Spin Target*". S&T Review, July 2, 2008. http://www.jlab.org/~ckeith/Frozen/SciTech.pdf

[67] http://clasweb.jlab.org/rungroups/g9/wiki/index.php/Main_Page